Mapping T-Cell Signal Integration From Synthetic, Membrane-Associated T-Cell Receptor Agonists

by

Kiera B. Wilhelm

A dissertation submitted in partial satisfaction of the

requirements for the degree of

Doctor of Philosophy

in

Chemistry

in the

Graduate Division

of the

University of California, Berkeley

Committee in charge:

Professor Jay T. Groves, Chair
Professor Ke Xu
Professor David Drubin

Summer 2022

Mapping T-Cell Signal Integration From Synthetic, Membrane-Associated T-Cell Receptor Agonists

Kiera B. Wilhelm

Abstract

Mapping T-Cell Signal Integration From Synthetic, Membrane-Associated T-Cell Receptor Agonists

by

Kiera B. Wilhelm

in Chemistry

University of California, Berkeley

Professor Jay T. Groves, Chair

T-cell receptors (TCRs) recognize sparse pathogenic peptides (p) displayed in major histocompatibility complex (MHC) proteins on the surface of antigen presenting cells (APCs). Wide natural diversity of TCR clonotypes within an individual enables a robust immune response but complicates efforts to study and therapeutically control T cell activation because the pMHC ligands for almost all natural TCRs are not known. Antibodies are widely used to universally activate T cells, but unlike monovalent pMHC, antibodies activate T cells from solution by inducing extensive TCR crosslinking and have high affinity for TCR. In contrast, the physical junction between the T cell and APC is required for productive T cell activation in response a few tens of monovalent, membrane-bound pMHC that bind TCR relatively weakly. These differences suggest that antibodies short-circuit native T cell signal integration processes that confer single molecule sensitivity. We have engineered a class of membrane-associated, synthetic TCR agonists that mimic biophysical properties of native pMHC in order to activate polyclonal T cells in a physiologically-relevant manner. The modular ligand design – an anti-TCR Fab' fragment conjugated to a DNA oligonucleotide – enables experimental control over physical parameters of ligand:TCR interactions including binding epitope, ligand geometry, and affinity. We find that, when presented on a supported lipid bilayer, high-affinity Fab'-DNA ligands activate T cells with similar potency as strong pMHC agonists, regardless of which epitope they bind. However, a short intermembrane space at binding events is necessary to maintain the native mechanical TCR triggering process. Notably, like pMHC, Fab'-DNA must be tethered to an opposing surface in order to trigger TCR; it is inactive from solution. By tuning Fab'-DNA binding kinetics to match naturally low pMHC:TCR affinities, we find roles for both on- and off-rates in coordinating the T cell activation response. The results obtained from these studies can aide in defining design principles for effective T cell therapies. Moreover, the ability of Fab'-DNA ligands to trigger TCRs in polyclonal T cells opens avenues to quantitate signal integration in human T cell populations using a membrane-associated, monovalent TCR agonist.

To Tricia Brady

Contents

List of Figures

List of Tables

Acknowledgments

I am so grateful to all of the family, friends, mentors, and collaborators who have supported me through my graduate school journey.

First foremost, thank you to my mom, Tricia Brady, for inspiring me to work toward a PhD and providing guidance and encouragement every step of the way. My sisters Katherine and Abby Wilhelm have brought humor, love, and a lot of fun, keeping my work toward my degree in perspective. And to the whole Brady family, thank you for your enduring love and support.

Huge thanks to my friends from Carleton for creating lots of opportunities to escape the Bay Area for fun adventures, and to my friends in the Bay for adventures nearby. A special shout out to Shannon Mueller who took many long bike rides with me through the hills with me, processing everything going on in our lives. And thank you to my cohort for their camaraderie through courses and quals, it couldn't have all gotten done without you.

My advisor, Jay Groves taught me to carefully define my questions, realize the story in my data, and communicate the impact of the conclusions. Jay's perspective was critical to integrating my findings into the broader literature and current discussions, and he skillfully directed my project toward directions that could have the most impact. Laurie Mason kept the lab running smoothly and made sure everything got done when it needed to be done, for which I am very grateful.

Many collaborators played critical roles in completing the work presented in this dissertation. Koli Basu, Kristin Wucherer, and Charly Craik kindly offered advice, guidance, and plasmids as I worked to bring the Fab expression platform to the Groves lab. Serena Muratcioglu offered advice for generating Fab mutants and helped develop screening assays. Lin Shen generously gifted polyclonal murine T cells for studying in our supported bilayer assays. Mike Coyle and Ariel Furst taught me the synthetic chemistry necessary for my project, and Geoff O'Donoghue taught me how to present my work in a paper and build the scaffolding around the data to tell a story. Orion Weiner and Derek Britain were amazing collaborators in developing the Fab-Zdk platform, and I had tons of fun working with them.

None of this could have happened without the support of all current and former members of the Groves lab. Thank you all for your guidance, thoughtful discussions, hours troubleshooting, collaborative spirit, and all the fun we had in and out of lab. The group taught me to make a perfect supported lipid bilayer, keep T cells alive outside a mouse for a week, analyze my data, and so much more. Shout out to pumpkin carving, murder mystery parties, bowling, hot pot, and classic conference room parties. I'd like to extend a special thanks to Joey DeGrandchamp, Anand Vissa, Nugent Lew, Mark O'Dair, Darren McAffee, Shalini Low-Nam, Sungi Kim, Shumpei Morita, Brittany Stinger, Laura Nocka, Hyuneil Kim, Scott

Hansen, and William Huang.

I'd like to thank my former mentors from secondary and undergraduate school for preparing me for the work of graduate school. A special thanks to Anthony Borgueta for teaching me to keep a lab notebook and to write everything down. My notes were invaluable in putting this document together.

Finally, to Oliver Heywood, thank you for all of your love, steadfast support, and many visits to Berkeley. I'm so excited to share alongside you whatever comes after this PhD!

Chapter 1

Introduction

T cells mediate adaptive immunity by recognizing sparse antigenic peptides (p) in major histocompatibility complex (MHC) molecules displayed on antigen presenting cells (APCs). In order for T cells to recognize any number of pathogenic peptides an individual may encounter, T cell populations are polyclonal. The T cell receptor (TCR) gene of developing thymocytes undergoes genetic recombination to produce cells expressing unique TCR clonotypes [1]. These thymocytes then undergo a selection process to ensure that they recognize host MHC molecules but do not respond so strongly to self-peptides that they cause autoimmunity [2]. This selection process, and the subsequent activation of mature T cells in circulation, requires that cells recognize sparse agonist pMHC presented on APCs in a sea of weak or null pMHC molecules.

A defining feature of physiological TCR triggering is that pMHC is bound to an apposing membrane, creating a close, 14 nm intermembrane junction between the APC and T cell at pMHC:TCR binding events. pMHC monomers are unable to trigger TCR from solution at any concentration [3], yet single ligation events between pMHC and TCR at cell junctions are sufficient to generate significant downstream signal [4–7]. Only tens of well-spaced binding events are required for cellular activation [8, 9]. While microclusters of bound TCR are seen at high antigen densities (10-250 μm^{-2}) [10, 11], a recent body of work has established that clustering is not required for TCR triggering [12] and likely does not predominate under physiological antigen densities (0.1 – 2 μm^{-2}) [13–15].

While the mechanisms that govern TCR triggering and antigen discrimination are not fully known, a few proposed models are well-supported by decades of evidence. The kinetic-segregation model of TCR triggering proposes that the close intermembrane spacing between the APC and T cell at pMHC:TCR ligation events locally excludes the abundant phosphatase CD45, which has a bulky extracellular domain [16–19]. By changing the local balance of kinase and phosphatase, CD45 exclusion enables TCR triggering. Force applied at TCR ligation events is also implicated in the TCR triggering mechanism [20–24], though how

force transmits signal through the TCR is under debate. Both kinetic-segregation and force models are consistent with the inability of TCR to be triggered by a monovalent ligand from solution and weak response to artificially heightened pMHC ligands presented on a surface [25]. All pMHC ligands, however, have approximately the same dimensions when displayed on an APC and must be differentiated as self or agonist ligand by some other means. T cells read ligand binding kinetics, and in particular the kinetic off-rate, to distinguish self- and agonist-pMHC across a narrow affinity range despite self pMHC outnumbering agonist over 10,000 fold. The kinetic proofreading model proposes that sensitivity and selectivity is achieved because the TCR complex must undergo a series of chemical changes, each of which takes time and energy, while it remains bound to pMHC before it can become signaling-competent [26]. Each step enhances the discriminatory ability of the TCR [27], though the mechanistic details of kinetic proofreading steps are still under investigation. Kinetic segregation and force TCR triggering mechanisms are suggested to play a role in how T cells discriminate ligand by kinetic proofreading [28].

The wide diversity of TCRs expressed within individuals complicates efforts to study and therapeutically control T cell activation, as cognate pMHC ligands for almost all natural TCRs are not known. To overcome this challenge, antibodies that bind constant regions of the TCR and associated CD3 chains are commonly used universally activate T cells [29, 30]. Antibodies are routinely coated on a substrate or used in solution at saturating concentrations with additional crosslinking agents. TCR crosslinking is an essential feature of solution activation by antibodies, and T cells will not activate without it [31]. Moreover, antibody-based T cell activation typically omits integrin engagement, which provides critical signals for setting T cell activation thresholds [8, 32, 33]. Because conditions of antibody activation differ dramatically from conditions under which TCR is triggered physiologically, they likely short-circuit native signal integration processes that enable T cells to maintain both high sensitivity and high selectivity.

Here, I aim to design an experimental system for activating polyclonal T cells that retains biophysical characteristics of native TCR triggering. In this system, the ligand must be monovalent and inactive from solution, yet able to trigger TCR when associated with an apposing membrane. A universal TCR agonist must, by definition, bind TCR in a constant region rather than the hypervariable pMHC recognition site, and so the influence of binding epitope on signal integration must be examined. Ligands should also be designed to span a range of binding affinities to test whether T cells discriminate between these ligands using similar proofreading mechanisms used to discriminate between pMHCs with high selectivity. Furthermore, all experiments should be conducted in the presence of integrin adhesion, with the ability to incorporate additional signaling through costimulatory molecules and coreceptors.

In effort to achieve this goal, I have developed a novel class of T cell receptor agonists consisting of the antigen binding fragment (Fab) of an anti-TCR antibody covalently linked to

a short, fluorescently labeled DNA oligonucleotide. These Fab'-DNA constructs are then presented on fluid glass-supported lipid bilayers (SLBs) by annealing to SLB-bound complementary strands. Intracellular adhesion molecule 1 (ICAM-1), which binds the integrin lymphocyte function-associated antigen 1 (LFA-1), is also incorporated onto the SLB, creating a pseudo-APC surface with which T cells can interact. The sample is readily imaged on an inverted fluorescence microscope by surface-selective and bulk imaging modalities. Binding events at the intermembrane junction are imaged at high resolution with total internal reflection fluorescence (TIRF) microscopy, and the localization of fluorescent markers of intracellular signal propagation are simultaneously monitored. We are able to precisely measure ligand binding parameters, such as off-rate, affinity, and the number, timing, and location of each binding event (input signal) and map these events directly to intracellular signaling consequences. By visualizing stochastic cell-to-cell variation in the binding event inputs and simultaneously monitoring readouts for signal propagation and activation, we can determine which features of input integration lead to cellular decisions [7, 9]. This experimental platform contrasts with other approaches for studying T cell signal integration in which binding kinetics and cellular responses are measured in bulk in separate assays and then correlated [34, 35].

The modular construction of Fab'-DNA provides great flexibility in engineering attributes of the synthetic ligand. Commercially available antibodies that bind constant regions of the TCR/CD3 complex are widely used and readily accessible for fragmentation to monovalent Fab' species. In addition, Fab' expression vectors allow mutations to be introduced into standard anti-TCR Fabs to control binding affinity and enable Fabs to be engineered against novel epitopes, making the technology broadly applicable. The DNA scaffold allows for high-affinity conjugation to the SLB while easily modulating the length of the tether, allows multiple distinct ligands to be patterned onto a surface [36], and enables complex structures such as heterodimers and designer clusters through DNA origami [37]. Though this work focuses on developing synthetic TCR ligands, Fab'-DNA constructs can be engineered to study a wide variety of interactions at cellular junctions [38].

Anti-TCR Fab'-DNA ligands fall into a growing category of T cell engagers (TcE). All TcEs contain an antibody-based TCR binding and a domain that binds a protein or moiety on another cell membrane or surface. Many TcEs are used to therapeutically control T cell activity, such a bispecific TcEs which direct cytotoxic T cells activity to cells displaying cancer markers [39–41]. Others are used to study the effect of mechanical and temporal variation in TcE binding on T cell response [42–45]. Fabs and single chain variable fragments are both popular binding moieties [39], and how the structure of TcEs affects T cell activity is under active investigation [45]. Results from supported bilayer studies with Fab'-DNA contribute to this conversation regarding the best methods for thereputically controlling T cell activation without inducing adverse effects through overstimulation.

The chapters following this introduction describe in detail my work mapping T cell signal

integration from Fab'-DNA ligands to characterize their activity and to provide insight into the mechanisms of TCR triggering and cellular signal processing. The vast majority of experiments are performed using transgenic murine T cells expressing the AND TCR, for which a well-characterized panel of cognate altered peptide ligands with varying affinities for the AND TCR exists. AND T cell signaling has been rigorously characterized on our SLB platform [7–9, 46, 47], allowing direct comparison between pMHC and Fab'-DNA signaling response in order to understand how signaling from the two classes of ligands compares.

In the second chapter, I introduce Fab'-DNA as a novel construct for studying T cell activation [9]. I show that the Fab'-DNA synthesized from the anti-TCRβ antibody H57-597 retains many key attributes of TCR triggering and cellular activation compared to pMHC: single binding events are sufficient to induce downstream TCR-proximal signaling; Fab'-DNA is active when membrane-associated, but not from solution; Fab'-DNA, which has a very long dwell time, has a potency similar to that of the strong pMHC agonist MCC-MHC; and Fab'-DNA at high densities stimulates significant production of the cytokine IL-2. Data suggest that Fab'-DNA may have a different relationship to integrin signaling compared to pMHC, as the contact area between the supported bilayer and T cell is not as stable through time at high ligand densities.

In chapter 3, I modulate geometric attributes of Fab'-DNA binding to TCR in order to explore how binding epitope and spacing between apposed membranes affects ligand potency [48]. I find that the TCR is agnostic to which epitope is bound by the Fab, with similar potencies for pMHC and three Fab'-DNA constructs. However, TCR triggering and cellular activation is sensitive to the intermembrane space allowed at binding events. Ligand that restrict this spacing to 14 nm are strong activators and potency dramatically decreases with increasing DNA tether length. Comparing these results to established models of TCR triggering suggests that Fab'-DNA triggers TCR in a similar manner as pMHC. That signaling through the TCR is indistinguishable regardless of which epitope a ligand binds allows for flexibility when designing Fab ligands against murine or human TCR, or perhaps even chimeric antigen receptors. This is useful to achieve the goal of designing a universal TCR agonist that, by definition, must bind an epitope distinct from the hypervariable pMHC binding site. This study expands upon the characterization done in the first chapter and provides greater foundation for how Fab'-DNA behaves as a TCR ligand.

In chapter 4, I address a critical difference between Fab'-DNA constructs used thus far and pMHC: binding kinetics. pMHC binds TCR quite weakly [49, 50], with affinities in the low- to mid-micromolar range whereas antibodies bind their epitopes very strongly, in the low-nanomolar range. Binding affinity, particularly ligand dwell time, is read by T cells to determine whether or not to respond to a binding event or collection of binding events. I modify a Fab expression vector to express anti-TCR Fabs with an additional hinge-region cysteine for conjugation to the DNA oligonucleotide. Mutations can then be introduced to modulate Fab affinity. The first mutant generated from this expression vector, H57 R97L,

has a high on-rate like other Fab'-DNA constructs, but a much higher off-rate than parental Fabs. It has a mean dwell time of 9 s, which is similar to that of native pMHC:TCR binding interactions. From this work, we learn that the dwell time of individual binding events must be several seconds to accumulate sufficient TCR-proximal phosphorylation to instigate a nearby LAT condensation, but the high on-rate allows multiple shorter binding events to cooperate. I also show, as a proof of principle, that Fab'-DNA constructs can be used to activate polyclonal T cells, and that ligand potency is correlated to dwell time.

In chapter 5, I highlight efforts to control ligand dwell time with optogenetics. We replace the DNA linker on the anti-TCR Fab with an 8 kDa protein, Z dark (Zdk), which binds its partner LOV2 in the dark. Upon incident blue light, LOV2 undergoes a conformational change and rapidly releases Zdk. We demonstrate that both in the dark and under blue light conditions, single LOV2:Zdk interactions follow zero-order unbinding kinetics, with the mean dwell time decreasing with increased blue light. Moving forward, this optogenetic system can be used to directly modulate ligand:TCR binding interactions and monitor downstream responses without changing the binding interface.

In the final chapter, I discuss the impact of this work on our current understanding of signaling through the T cell receptor and then summarize future directions opened by the development of Fab'-DNA as a tool to probe T cell signaling. One of the most exciting areas of future research is to develop a Fab'-DNA affinity panel for human T cells in order to quantitatively assay T cell activity from patient samples in diagnostic settings.

Chapter 2

Fab'-DNA Potently Activates T Cells

2.1 Abstract

The natural peptide-major histocompatibility complex (pMHC) ligand for T cell receptors (TCR) is inactive from solution yet capable of activating T cells at single molecule levels when membrane associated. This distinctive feature stems from the mechanism of TCR activation, which is thought to involve steric phosphatase exclusion as well as direct mechanical forces. It is possible to defeat this mechanism and activate T cells with solution ligands by crosslinking pMHC or using multivalent antibodies to TCR. However, these widely-used strategies activate TCRs through a non-physiological mechanism and can produce different activation profiles than natural, monovalent, membrane-associated pMHC. Here, we introduce a strictly monovalent anti-TCRβ H57 Fab' ligand that, when coupled to a supported lipid bilayer via DNA complementation, triggers TCRs and activates nuclear translocation of the transcription factor Nuclear Factor of Activated T cells (NFAT) with a similar potency to pMHC in primary murine T cells. Importantly, like monovalent pMHC and unlike bivalent antibodies, monovalent Fab'-DNA triggers TCRs only when physically coupled to the membrane, and only around 100 individual Fab':TCR interactions are necessary to stimulate early T cell activation.

2.2 Statement of Significance

We report the synthesis of a monomeric Fab'-DNA conjugate and demonstrate its utility as a high potency, universal T cell ligand when tethered to a supported lipid membrane via DNA complementation. Quantitative analysis confirms the Fab'-DNA conjugate has potency similar to strong agonist pMHC, and around 100 Fab':TCR interactions are required to initiate downstream signaling. The Fab'-DNA ligand is engineered to mimic the biophysical properties of a native pMHC ligand, except MHC-restriction, and provides a universal agonist suitable for quantitative analysis of T cell signaling activity.

2.3 Introduction

T cells form the front line of the adaptive immune system, and their activation by foreign antigen is governed by T cell antigen receptors (TCRs). A distinctive feature of TCRs is that the genes encoding the TCR undergo genetic recombination in developing thymocytes [1]. The resulting TCR clonotypes are screened by a selection process based on their ability to weakly bind self peptide antigen presented in major histocompatibility complex (pMHC) molecules on antigen presenting cells (APCs). TCR recombination and selection results in millions of T cells with distinct TCR clonotypes within an individual that are able to interrogate a practically infinite repertoire of pMHC ligands, forming the basis of adaptive immunity. A few, specific TCRs have been cloned, and for these, agonist pMHC molecules have been identified [51, 52]. More recently, high throughput pMHC tetramer and yeast display technologies have enabled identification of peptide agonists for specific TCRs [24, 53]. But without the pMHC molecule that triggers a particular TCR, it is essentially impossible to activate the natural agonist pMHC-triggered TCR response *in vitro* or therapeutically.

To overcome this challenge, bivalent antibodies that bind variable and constant regions [29, 30, 54–56] of the TCRα/β chains and associated CD3 chains have been developed. Antibodies successfully stimulate proliferation [30, 54, 55], cytokine production [29, 56], and CD69 expression [57]. However, T cells can exhibit different activation profiles and mechanisms when they are stimulated with monovalent membrane-bound agonist pMHC compared to bivalent antibody [6, 32, 33, 58]. For example, T cells interacting with an APC displaying agonist pMHC require adhesion through integrins in order to produce the cytokine IL-2, whereas T cells activated by antibodies from solution can stimulate IL-2 production in the absence of adhesion [33]. Anti-TCR/CD3 antibodies require high concentrations and additional crosslinking to activate from solution [31]. Tethering anti-CD3 to a surface seems to circumvent the need for crosslinking, but the activation profile differs from solution [59]. Although antibodies targeting TCRα/β and associated CD3 chains have revealed fundamental properties of T cell activation, they can short-circuit some features of the T cells' native signal discrimination mechanisms. There is thus a substantial need for alternative antibody-based ligands that trigger the TCR via a mechanism more closely mimicking the

physiological mechanism of TCR activation by agonist pMHC on APCs, while retaining the broad TCR specificity of stimulatory antibodies. Such a ligand would trigger the TCR without external cross-linking, would be monomeric and monovalent, and would trigger the TCR when tethered to a membrane but not from solution.

It has long been established that pMHC monomers activate T cells only when surface-tethered, but that pMHC tetramers can activate T cells from solution [3, 60]. Based on these observations, it was natural to assume that TCR crosslinking was the mechanism of TCR activation. This TCR-crosslinking mechanism was further supported by the visible formation of microclusters of pMHC:TCR in the immunological synapse [10, 61–66]. However, TCR microclusters are generally observed at densities of agonist pMHC 10-100s of times greater than physiological pMHC densities [10, 11, 15, 62, 67, 68] (Table 2.1). Detailed analysis of agonist pMHC near threshold activation densities ($< 1\ \mu m^{-2}$) [8, 9, 46, 69] revealed that pMHC triggers TCR and activates T cells as a monomer [4–6, 47, 70] and large-scale crosslinking of TCRs does not occur [12, 71].

Within the past decade, studies that directly probe mechanical activation of the TCR have identified a mechanism by which force can trigger the TCR [20–22, 72, 73]. These investigations conclude that the TCR requires a mechanical force applied to its extracellular domain to actuate a structural transition that enables immunoreceptor tyrosine-based activation motif (ITAM) phosphorylation by Lck and activation of the TCR [21, 24, 74]. This force-mediated activation mechanism provides an explanation for why agonist pMHC is inactive from solution and only active when surface associated, where it can mediate force transmission to the TCR. It is plausible that TCR crosslinking could induce force coupling between receptors, and thus achieve some activation. However, the cis geometry of crosslinked receptors on the cell surface is clearly very different from the force vectors that would be achieved in the physiological trans configuration of pMHC:TCR binding between an APC and a T cell. Alternatively, steric exclusion of the CD45 phosphatase from the vicinity of engaged pMHC:TCR complexes has long been considered a mechanism by which TCR is activated [17, 18]. Under this mechanism, pMHC:TCR complexes create a relatively close apposition of the T cell and APC membranes, which provides insufficient space to accommodate the bulky CD45 extracellular domain.

Here, we introduce a monomeric anti-TCRβ Fab' ligand, henceforth referred to as Fab'-DNA, that triggers TCR and stimulates early T cell activation as individual monomers when tethered to a supported lipid bilayer (SLB) via DNA complementation but cannot trigger TCR from solution (Fig. 2.1). The Fab'-DNA synthetic strategy is general and can be applied to any number of different Fab' fragments [30, 37, 75, 76], or juxtacrine signaling molecules [38]. This study focuses on Fab' derived from the H57-597 antibody, which binds the FG loop on the constant region of TCRβ (Fig. 2.1C-D) [29, 77], a motif implicated in TCR mechanosensing [20, 70, 78]. The H57 Fab' is widely used as a TCR label for imaging studies, where it is known not to activate at any concentration and also does not

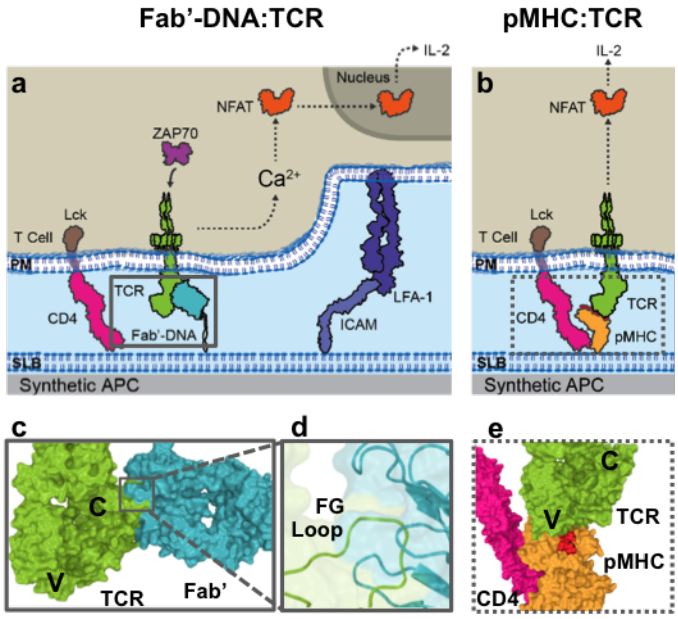

Figure 2.1: A membrane-tethered, universal T-cell receptor agonist. a. Schematic of membrane-tethered Fab'-DNA binding to the T cell receptor (TCR) and initiating signaling cascade to result in the production of cytokine IL-2. **b.** Schematic of the natural, cognate agonist pMHC:TCR binding and signaling. The extracellular domains of the CD3 chains have been omitted for clarity. **c.** Structural model of the H57-597 Fab'-DNA:TCR complex (gray box in a). The constant (C) and variable (V) regions of the TCR are indicated. Adapted from PDB structure 1NFD. **d.** Zoomed in structural model from c, focusing on the interaction between the FG loop of the TCR and heavy chain of the anti-TCR Fab'. **e.** Structural model of the tertiary CD4:pMHC:TCR complex (gray, dotted box in b). The constant (C) and variable (V) regions of the TCR are indicated. Adapted from PDB structure 3T0E.

interfere with pMHC-mediated TCR activation [8, 12, 65, 79, 80]. Once on the membrane, H57 Fab'-DNA remains strictly monomeric and does not crosslink TCR, as characterized by single molecule imaging at the SLB – live cell interface. Similar to pMHC, single molecule binding events between Fab'-DNA and TCR recruit Zap70 to the TCR and activate the calcium signaling pathway. Measurements of *in situ* Fab'-DNA:TCR binding using single molecule imaging [8, 47] reveal that Fab'-DNA is a stronger binder than a strong agonist pMHC. The threshold density at which half of assayed T cells translocate nuclear factor for the activation of T cells (NFAT), an indicator of Ca^{2+} pathway activation (Fig. 2.1A-B) [81, 82], is very similar for the strong agonist pMHC and Fab'-DNA, at about 0.2 μm^{-2}. The hybrid protein-DNA synthetic strategy employed here is intrinsically modular and will enable facile exploration and development of numerous universal TCR ligands with differing TCR engagement geometry (epitope) as well as molecular binding dwell time (affinity). Such tools may be of utility to better resolve the mechanisms of TCR activation and may inform

the design of bispecific T cell engagers (BiTEs), a class of cancer immunotherapeutic agents that are structurally similar to Fab'-DNA.

2.4 Materials and Methods

Reagents

The phospholipids 1,2-dioleoyl-sn-glycero-3-phosphocholine (DOPC), 1,2-dioleoyl-sn-glycero-3-[(N-(5-amino-1-carboxypentyl)iminodiacetic acid)succinyl] nickel salt (Ni-DOGS), and 1,2-dioleoyl-sn-glycero-3-phosphoethanolamine-N-[4-(p-maleimidomethyl)cyclohexane-carboxamide] sodium salt (MCC-DOPE) for preparation of supported membranes were purchased from Avanti polar lipids (Alabaster, AL) as chloroform solutions. Pepsin from porcine gastric mucosa (3200-4500 U/mg, lyophilized powder) was purchased from Sigma-Aldrich (St. Louis, MO). ATTO647N maleimide was purchased from Atto-tec, AlexaFluor555 maleimide was purchased from Thermo Fisher and custom DNA oligonucleotides were purchased from Integrated DNA Technologies (Coralville, IA). Succinimidyl-[(N-maleimidopropionamido)-hexaethyleneglycol] ester (SM-PEG¬6-maleimide), Protein A, Protein A/G, and Protein G resins were purchased from Thermo Fisher).

DNA oligonucleotide sequences:
Sequence 1: 5- /5AmMC6/GGT GTG ATG TAT GTG GA/3ThioMC3-D/ -3
Sequence 2: 5- /5ThioMC6-D/CCA CAT ACA TCA CAC C -3

The hybridoma cell line that was used for monoclonal antibody production was obtained from ATCC (HB-218). Cell culture reagents were obtained from Gibco unless otherwise noted. The H57-597 antibody was also obtained commercially from Bio X Cell (West Lebanon, NH) and Biolegend (San Diego, CA).

Hybridoma culture and preparation of anti-TCR H57-597 monoclonal antibody

The hybridoma cell line for production of anti-TCR monoclonal antibodies was maintained in DMEM with added glutamine, pyruvate, and 10% fetal bovine serum (non-essential amino acid mixture was sometimes used in place of pyruvate). To facilitate antibody purification, Cells were adapted to BD Cell MAb Media, Quantum Yield (BD Biosciences) containing 2.5% ultra-low IgG FBS (Gibco). Alternatively, cells were adapted to Hybridoma SFM (Gibco) media supplemented with cholesterol (Gibco) and containing no serum supplement.

The antibody was purified using standard antibody affinity chromatography techniques (Protein A or Protein G, with both being effective in this case). Briefly, the hybridoma culture supernatant was diluted in neutral phosphate buffer to ensure binding to the resin and sterile filtered. The antibody was eluted with 0.1 M glycine pH 2.5. These fractions were neutral-

ized with one-tenth volume of 1 M Tris pH 8. These fractions were then pooled and buffer exchanged into phosphate buffered saline for storage at -80 °C until use.

Preparation of 3' fluorophore labeled 5'- maleimide functionalized DNA

For preparation of fluorophore labeled precursors, DNA oligonucleotides with a 3' thiol group in addition to a 5' amino group were used. In this case, the thiol group was functionalized first with a maleimide dye using the following procedure: ten equivalents of TCEP were added to the oligonucleotide and incubated for 1 hour in 100 mM HEPES. The reducing agent and residual thiol groups were removed using a NAP-5 column. After desalting, five equivalents of maleimide dye were added and incubated for one hour. After incubation, the free dye was removed again by a desalting column (such as those mentioned above). Labeling efficiency was verified using MALDI-TOF. The final product was ethanol precipitated and dried.

Maleimide DNA was prepared from this material by mixing resuspending DNA-dye in water, SM-PEG_6-maleimide, and 10x PBS to final concentrations of 0.5 mM DNA-dye, 12.5-25 mM SM- PEG_6-maleimide (25-50 equivalents), and 1x PBS. Half of the SM-PEG_6-maleimide reagent was added immediately to initiate the reaction and the remainder half was added after the reaction had proceeded for 30 min. The product was desalted over a NAP-5 column equilibrated in 1x PBS and ethanol precipitated and dried.

Preparation of Fab'-DNA from anti-TCR mAb

Purified anti-TCR antibody (either purchased or purified as above) was digested with pepsin at a ratio of pepsin to antibody (by mass) of 1:25-30 for 8 hr at 37C, with agitation, in 0.1 M acetate buffer pH 4.5 or 40 min in 0.1 M citrate buffer pH 3.5 to produce $F(ab')_2$ fragments. Optimal conditions were found to be a 1:25 mass ratio for 8 hr using the acetate buffer. The digestion was stopped by treatment with one-tenth volume of 1 M Tris pH 8 and buffer exchanged or dialyzed into 50 mM phosphate buffer, 150 mM NaCl, pH 7.4 or 1x PBS. Residual IgG was removed by treatment with protein A. Purified $F(ab')_2$ is stable at 4 °C for at least one week. This $F(ab')_2$ preparation was then treated with 2 mM freshly prepared 2-MEA in 1x PBS with 1 or 2 mM EDTA for 90 min to produce Fab' fragments. The reducing agent was removed by a combination of gel filtration and centrifugal ultrafiltration. Maleimide DNA was immediately added in 2-20 fold molar excess and incubated at room temperature for 1-3 hours or overnight at 4 °C. More details are shown in Supplementary Table 4.

For preparation of a pure sample of Fab'-DNA conjugated to exclusively one molecule of DNA (all experiments other than Supplementary Fig. 15), it was necessary to perform a two-step purification of the molecule. The Fab'-DNA reaction mixture was purified by

size exclusion chromatography (Superdex 75 or Superdex 200, GE Healthcare). Fractions containing Fab'-DNA were pooled and injected on a Mono Q 5/50 GL. Similar results were obtained using anion exchange before size exclusion chromatography, and this approach was used for the reagent in Supplementary Figure 12.

Thiol-DNA preparation

Thiol DNA at a concentration of 1 mg/mL (197 μM) was reduced by treatment with 2 mM tris(2-carboxyethyl)phosphine) (TCEP) in 10 mM HEPES pH 8 at 37 °C for 90 min. After incubation, the sample was desalted sequentially in two Biospin 6 columns that had been equilibrated in PBS according to the manufacturer's direction. The concentration after desalting was measured using absorbance at 260 nm on a Nanodrop 2000 spectrophotometer.

Supported membrane preparation

Supported membranes were produced according to a previous procedure that was adapted for use with flow cell systems (FCS2 Closed Chamber Systems Bioptechs, Butler, PA) or Attofluor cell chambers (Invitrogen). For the FCS2 system, No.2 40 mm diameter round coverslips were ultrasonicated for 30 minutes in 50:50 isopropyl alcohol:water, rinsed thoroughly in Milli-Q water (EMD Millipore, Billerica, MA), etched for 5 minutes in piranha solution (3:1 sulfuric acid:hydrogen peroxide), and again rinsed thoroughly in Milli-Q water. The coverslips were used in the assembly of the flow cells, which were prefilled with phosphate buffered saline (Mediatech Inc., Herndon, VA). For Attofluor cell chambers, 1.5 Warner brand 25 mm round coverslips were cleaned, etched, assembled, and prefilled as above.

Vesicles for bilayer formation were prepared by sonication of a 0.5 mg/mL suspension of lipids in water containing 95% DOPC, 2% Ni-DOGS, and 3% MCC-DOPE. Sonicated solutions were then centrifuged at 21,000 × g for 20 min at 4 °C. Vesicle solutions in water were mixed 1:1 with PBS, injected into assembled flow cells, and incubated for 30 minutes. After rinsing, thiol DNA (seq. 2, reduced and desalted as described in Thiol-DNA preparation) was injected at a final concentration of 1 μM and incubated for 80-120 minutes. The density of thiol DNA on the bilayer (100's thiol DNA/μm^{-2}) is primarily a result of this initial incubation concentration (51) and always far exceeded the desired density of Fab'-DNA. The membrane was then incubated with 100 mM $NiCl_2$ in Tris-buffered saline (TBS, Cellgro) for 5 min, rinsed with TBS, and then rinsed with imaging buffer (1 mM $CaCl_2$, 2 mM $MgCl_2$, 20 mM HEPES, 137 mM NaCl, 5 mM KCl, 0.7 mM Na_2HPO_4, 6 mM D-glucose, and 1% w/v bovine serum albumin). A solution containing all proteins to be coupled to the membrane was then prepared in imaging buffer, added to the sample and incubated for 30-35 min. Calibrations of solution concentration to final surface density were established experimentally for Fab'-DNA, pMHC, and ICAM-1 stock solutions. Suitable surface densities for single molecule experiments were achieved by using very low solution incubation concentrations

of Fab'-DNA (50-200 pM). Alternatively, Fab'-DNA surface density could be controlled by mixing the Fab'-DNA reagent with a "blocking" DNA strand comprising the same nucleotide sequence but with no fluorophore and not conjugated to Fab', thus occupying some of the available binding locations on the surface. The total DNA concentration was targeted to 100 nM, and ratios of Fab-DNA to blocking DNA (determined empirically to achieve a specific surface density) of between 1:20 and 1:200 were generally used. To maximize the bilayer concentration of Fab'-DNA in the calcium flux experiment, no blocking strand was used and the incubation concentration of Fab'-DNA was 100 nM. The solution incubation concentrations of pMHC and ICAM-1 used in experiments were approximately 0.2 – 1 nM and 100 nM respectively. Incubation concentrations could be adjusted as needed based on the surface density observed in TIRF images. After 30-35 min, the flow cell was washed with imaging buffer and equilibrated for 30 minutes to 37 °C before adding cells. All imaging was done at 37 °C.

T-cell harvesting and culturing

$CD4^+$ T cells expressing the AND TCR (59) were harvested, cultured, and transduced as previously described [8, 9, 47, 83]. Briefly, T cells were harvested (day 1) from AND × B10.BR transgenic mice (Jackson Laboratory) and activated by moth cytochrome c (amino acids 88103) (MCC) peptide immediately after harvest. IL-2 was added 24 hours after harvest (day 2) to promote proliferation. On day 3, activated T cells were retrovirally transduced with ZAP70-eGFP or NFAT-mCherry-containing supernatants collected from Platinum-Eco cells (Cell Biolabs, San Diego, CA). ZAP70-eGFP-transduced T cells were sorted using fluorescence-activated cell sorting (FACS) based on eGFP expression level. Gates were selected to isolate cells expressing low levels of ZAP70-GFP, in order to ensure a constant ratio of exogenous:endogenous ZAP70 [47]. Cells expressing the NFAT-mCherry translocation reporter were not sorted. T cells were imaged on days 5 to 7. All animal work was approved by Lawrence Berkeley National Laboratory Animal Welfare and Research Committee under the approved protocol 177002.

Calcium flux analysis

Intracellular calcium was observed using the ratiometric fluorescent calcium indicator fura-2-acetoxymethyl (FURA-2 AM). Cells were incubated with 1 μM FURA for 15 minutes at room temperature in serum-free culture media. Cells were then pelleted and resuspended in cell culture media with serum for 20 minutes at 37 °C. For image collection, FURA was excited at 340 and 380 nm with emission collected at 510 nm via a 40xS Fluor objective (Nikon) on a CoolSnap K4 camera (Photometrics Tuscon, AZ). Fields of view were monitored every 15 s for 20 min. Cell motion and ratiometric fluorescence intensity were tracked and analyzed semi automatically in Imaris, Matlab, and Excel.

TIRF microscopy

TIRF experiments were performed on a motorized inverted microscope (Nikon Eclipse Ti-E; Technical Instruments, Burlingame, CA) equipped with a motorized Epi/TIRF illuminator, motorized Intensilight mercury lamp (Nikon C-HGFIE), Perfect Focus system, and a motorized stage (Applied Scientific Instrumentation MS-2000, Eugene, OR). A laser launch with 488, 561, and 640 nm (Coherent OBIS, Santa Clara, CA) diode lasers was controlled by an OBIS Scientific Remote (Coherent Inc., Santa Clara, CA) and aligned into a fiber launch custom built by Solamere Technology Group, Inc. (Salt Lake City, UT). A dichroic beamsplitter (z488/647rpc; Chroma Technology Corp., Bellows Falls, VT) reflected the laser light through the objective lens and fluorescence images were recorded using an EM-CCD (iXon 897DU; Andor Inc., South Windsor, CT) after passing through a laser-blocking filter (Z488/647M; Chroma Technology Corp., Bellows Falls, VT). Exposure times, multidimensional acquisitions, and time-lapse periods for all experiments were set using Micro-Manager [84]. A TTL signal from the appropriate laser triggered the camera exposure. Colors were registered before each two-color Zap70 and Fab'-DNA tracking experiments by imaging 100 nm Tetraspec beads (Invitrogen Inc.) deposited on a coverslip patterned with a Cr grid with 80 nm width and 3–4 μm pitch Cr lines. The Tetraspec beads preferentially bind the Cr pattern and create images with high-density, regularly spaced patterns covering the entire field of view.

The laser intensities were measured at the sample for each experiment day, so that a constant laser intensity is used for each type of imaging across different days. Imaging of Fab'-DNA diffusion on the supported membrane was performed with a streaming acquisition of 14 ms and 21 ms exposure time at 11 mW and 9 mW power at the sample for Fab'-DNA-Atto647N and –AlexaFluor555, respectively. Additionally, to accurately localize particles of Fab'-DNA-AlexaFluor555, pixels were binned in 2x2 arrays. The longer exposure time and binning were needed to resolve the dim, quickly diffusing AlexaFluor555-labeled particles. Images for the Fab'-DNA intensity distribution were taken with the same acquisitions settings as for the diffusion data. For Fab'-DNA dwell time measurements, TIRF images of long exposure time (500 ms) using a laser power of 0.8 mW (640 nm) or 1.0 mW (561 nm) at the sample were collected every 10 (MCC pMHC) or 15 (Fab'-DNA) s. Photobleaching data were taken for each species using the same laser power and exposure time as was used to collect dwell time data, but without a time lapse in order to minimize recovery after photobleaching. The fraction bound measurements were taken with power at the sample of 4.4 mW (640 nm), exposure times of 20 ms and 500 ms, and EM gains of 500 and 50 to resolve all and bound Fab'-DNA molecules, respectively. Images for all and bound ligands were taken sequentially, with a 1 s time lapse for the kinetic data. The two-color Zap70 and Fab'-DNA tracking experiments was acquired using a streaming acquisition with a 500 ms exposure time and at laser powers of 0.8 mW (640 nm) and 0.5 mW (488 nm) at the sample.

NFAT nuclear translocation assay

Early activation state was measured based on detection of an NFAT sensor. In dynamic acquisitions, NFAT localization was measured using epifluorescence detection at 3 and 6 μm above the supported bilayer, at a frequency of 60 seconds. These images were interleaved with RICM and Fab'-DNA images, at a typical temporal resolution of 15 seconds each. Binding event accumulation and NFAT localization were observed in single cells for 20-60 minutes. For the NFAT titration, T cells were allowed to interact with the bilayer for 15 minutes, prior to imaging. Single sets of RICM, Fab'-DNA and NFAT images were acquired for at least 15 fields of view.

T cell activation state was determined by ratio of the mean intensity of the NFAT sensor in the nucleus to the cytoplasm, as previously described [8, 9]. A ratio greater than 1 indicates activation. In the dynamic measurements, the point of initial activation is defined as the first frame where the ratio increases above the initial, basal level. In the titration measurements, only cells with substantial interfacial contact areas (based on RICM signal) were included in the quantification of endpoint NFAT activation state.

IL-2 ELISA

IL-2 was assayed from the supernatant of T cells interacting with supported lipid bilayers or antibody-coated glass for 6 hours at 37 °C. Chambers were prepared as described above, and cells were imaged as they landed and spread, after 1 hour, and after 3 hours. At 6 hours, 400 μL of supernatant was removed from each chamber and centrifuged at 800 x g for 10 min to remove cell debris. The ELISA was completed according to manufacturer's instructions (Mouse IL-2 ELISA MAXTM Deluxe Set, Biolegend, San Diego, CA, Cat. No: 431004).

Image analysis

Intensity distribution. Fluorescent particles were localized in shade-corrected and background-subtracted images using the TrackMate plugin of FIJI [85]. Particle diameters and intensity thresholds were determined by eye and then applied uniformly. Intensity distributions were constructed and fit to a log-normal distribution using the distribution fitting tool in MATLAB.

Step size distribution. Fluorescent particles were tracked using the TrackMate plugin of FIJI. Particle diameters, intensity thresholds, and maximum linking distances were set by eye and then all data were uniformly analyzed. The particle density in movies was very low ($< 0.01\ \mu m^{-2}$) to accurately track single particles for 10's to 100's of frames. In the rare occasion that two particles overlapped, only one particle was localized and this localization was used to populate the step size distribution along one track. The other particle was split into a second track. Because overlapping events are very rare at these low densities,

this is expected to have negligible impact on the final step size distribution. The particle localization and linking data were exported to MATLAB using a custom python script.

A custom MATLAB script was then used to build step size distributions as a function of time lapse. Step sizes were too small between adjacent frames relative to camera pixel size and TrackMate sub-pixel localization error, resulting in regular spikes in the step size distribution built from particle localizations in adjacent frames and the appearance that the distribution represented two diffusing components when only one was present (Supplementary Fig. 8B) (unpublished work by Dr. Young Kwang Lee). Consequently, this shortest time delay (14 ms or 21 ms, depending on construct) was removed from analysis. For subsequent time delays, distances were calculated between every other frame, every third frame, etc. drawing from the same tracking data. Skips were used rather than a scanning window to prevent over-counting. The entire data set was then fit to a single component diffusion model to extract the diffusion coefficient, D. This global fitting protocol was used to mitigate systemic irregularities that may result from biases within TrackMate's localization algorithm [86]. Error was calculated using a 95% confidence interval. The global fit through this protocol was nearly identical to the average of the individual step size distributions at each lag time (Supplementary Fig. 8C).

Single particle photobleaching. Tracks from step size distribution movies were confirmed by eye to end with a photobleaching event, as opposed to leaving the field of view or crossing paths with another particle. The entire intensity traces of particles that photobleached were constructed and analyzed using a Bayesian change point detection algorithm [87] within a MATLAB script.

Dwell time distribution. Data were first filtered to include only fluorescent particles under cell footprints, as determined by RICM. RICM edges were detected using the following algorithm, executed in Matlab: First the image was thresholded using isodata thresholding. Next, small objects and objects touching the image edge were removed. Any holes in the thresholded areas were filled in, and the object with the largest area was identified. Lastly, the selected area was slightly dilated to more accurately capture membrane ruffles and filopodia at the SLB – T cell interface. Fluorescent particles were then tracked using TrackMate. Particle diameters, intensity thresholds, and maximum linking distances were set by eye, guided by the diffraction limit and the speed at which Fab'-DNA:TCR binding events move under cells, and then all data were uniformly analyzed. The Fab'-DNA:TCR binding interaction is significantly longer than the MCC pMHC:TCR interaction and required increasing the time interval between acquisitions from 10 s to 15 s in order to minimize the effects of photobleaching. The long dwell time complicates linking single molecule Fab':TCR features into trajectories, primarily due to overlapping trajectories below the diffraction limit, either in the periphery of the cell or as trajectories reach the immunological synapse, which occurs within 2 min of peripheral ligand binding. This leads to a systematic undercounting of long Fab'-DNA:TCR dwell times and an excess of short, artificially cut-off trajectories. Fluo-

rophores resolved for only one frame were discarded from analysis due to occasional spurious localization errors. The dwell time distribution was built using a custom MATLAB script and was fit in either MATLAB or Igor to a single exponential decay.

The data for photobleaching were cropped to a region of even illumination and the mean intensity of each frame was plotted as a function of time. These data were background subtracted and fit to a double exponential decay due to a dim, quickly bleaching background contaminant. The longer time constant was then multiplied by the time lapse used in acquiring the dwell time data to accurately capture the photobleaching rate. A photobleaching curve was taken and analyzed for each species measured, MCC pMHC-Atto647N, Fab'-DNA-Atto647N, and Fab'-DNA-Alexa555. The bleaching rate is subtracted from the observed off-rate to determine the mean single molecule lifetime.

Fraction bound. The RICM channel was used to crop images to single cells and mask images of all and bound Fab'-DNA molecules. Particles were localized using TrackMate and number of bound Fab'-DNA was divided by the total number of Fab'-DNA for each cell to measure the fraction bound. This fraction may exceed 1 if a Fab'-DNA molecule bound TCR during the long-exposure image, after the corresponding short-exposure image.

Zap70. In two-color experiments, a 3 pixel by 3 pixel area centering on the localized positions of single Fab' molecules were used as a mask to integrate the intensity from the spatially registered ZAP70-EGFP channel. These intensity traces were then used to correlate Fab' and ZAP70 binding events.

Adhesion signatures. A custom MATLAB script was used to crop images to single cells, mask the RICM footprint, and calculate the contact area between the cell and bilayer.

2.5 Results

Synthesis and biochemical characterization of a monovalent Fab'-DNA reagent

Fab'-DNA was synthesized by conjugating H57 Fab' fragments and maleimide derivatized fluorophores to DNA oligonucleotides modified with 5' amino and 3' thiol groups (Fig. 2.2A). The 17 bp DNA oligonucleotide component of the Fab'-DNA reagent approximates the same intermembrane spacing as pMHC when bound to TCR (Supplementary Fig. 1) and can sustain forces up to about 28 pN [88]. The maleimide fluorophore (Atto647N or AlexaFluor555) was first conjugated to the 3' thiol group for the purpose of monitoring single molecule Fab' fragments on the supported membrane. The 5'-amino group was then derivatized by an NHS-maleimide bifunctional crosslinker for subsequent conjugation to the hinge-region thiols of Fab' fragments. Matrix assisted laser desorption/ionization-time of flight (MALDI-TOF) spectra confirm that all detectable oligonucleotides with the bifunctional crosslinker – and

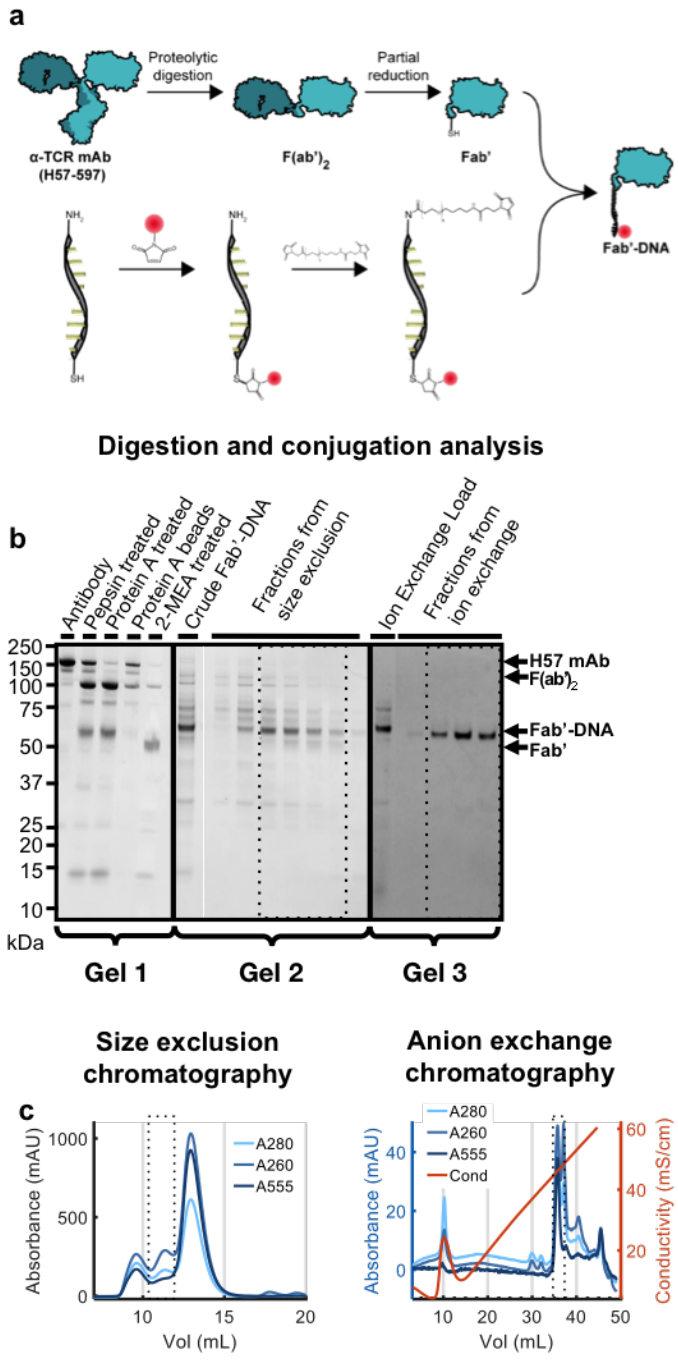

Figure 2.2: Preparation of Fab'-DNA conjugates. a. The anti-TCR antibody H57-597 was proteolytically digested with pepsin to produce $F(ab')_2$ fragments. These fragments were partially reduced using 2-mercaptoethylamine to produce Fab' fragments with reactive cysteine residues in the hinge region. After removal of reducing agent, the product was exposed to fluorophore-labeled maleimide DNA to produce the Fab'-DNA conjugates. **b, c.** Synthesis and purification of Fab'-DNA-AlexaFluor555. **b.** The products of each of these transformations were analyzed by SDS-PAGE. **c.** Additional purification steps (size exclusion and ion exchange chromatography) were required to produce Fab' fragment labeled with a single copy of fluorophore labeled DNA. Dotted boxes indicate fractions selected for further purification or final product after size exclusion or ion exchange chromatography, respectively.

thus capable of binding Fab' – are labeled with fluorophore (i.e. there is no peak in the final product with an m/z ratio corresponding to oligo+linker) (Supplementary Fig. 2). In addition, UV-vis quantitation based on the calculated extinction coefficient of the oligonucleotide and the dye showed $> 93\%$ conversion, indicating that nearly all Fab'-DNA conjugates are visualized.

In order to produce Fab' fragments that retain cysteine residues from the hinge region of the parent IgG molecule, we employed a two-step approach using pepsin digestion followed by partial reduction of the hinge disulfide bond with 2-mercaptoethylamine. SDS-PAGE analysis verifies formation of the desired Fab'-DNA conjugate, showing a gel shift upon treating Fab' fragments with the prepared dye-labeled maleimide DNA (Fig. 2.2B). This product necessitated further purification using size exclusion and ion exchange chromatography to ensure the final product contained Fab' fragments with strictly one conjugated oligonucleotide (Fig. 2.2C, Supplementary Figs. 3-5). Analysis of the eluted fractions after all purification steps by SDS-PAGE revealed the presence of a single band at the expected molecular weight for the Fab'-DNA conjugate. Analogous data for the preparation of Fab'-DNA-Atto647N are shown in Supplementary Figs. 3 and 5.

The Fab'-DNA reagent is monovalent when conjugated to supported membranes

The purified Fab'-DNA conjugate was coupled to supported membranes via covalent maleimide:thiol chemistry and DNA hybridization following a two-step incubation procedure (Fig. 2.3A). For detailed single molecule characterization, extremely low defect density supported membranes are essential. Small unilamellar vesicles (SUV) were first prepared from a mixture of 95% choline, 3% maleimide, and 2% nitrilotriacetic acid (NTA) headgroup phospholipids by probe sonication in MilliQ water followed by centrifugation to remove titanium particles and lipid aggregates. SUVs were then mixed 1:1 with 1x PBS resulting in a spreading solution with a final concentration of 0.25 mg/ml total lipid content. Supported membranes were formed on freshly piranha-etched glass coverslips by vesicle fusion of SUV from the spreading solution in an imaging chamber. The supported membrane was then treated for 80 minutes with a 5' thiol-modified oligonucleotide with a sequence complementary to the Fab'-DNA (thiol-DNA). The concentration of thiol-DNA was selected to target a density of 100 maleimide-DNA conjugates/μm^2 on the supported membrane (51). The membrane was then charged with Ni^{2+} after rinsing excess thiol-DNA from solution to ensure chelation of polyhistidine-tagged proteins to the membrane. Finally, polyhistidine-tagged intercellular adhesion molecular-1 (ICAM-1) [89], which binds to integrin receptors LFA-1 on the T cell and is essential to form a continuous T cell–antigen presenting cell contact [90], and Fab'-DNA, were mixed and incubated in the imaging chamber for 35 minutes. In the final assembled supported membrane, Fab'-DNA hybridizes with complementary DNA that is covalently coupled to maleimide phospholipids (Fig. 2.3A), whereas ICAM-1 couples to NTA phospholipids through multivalent Ni^{2+}:Histidine interactions [37, 89]. Fluorescent Fab'-DNA-Atto647N complexes were not observed on the supported membrane when the complementary thiol-DNA strand was absent, indicating minimal nonspecific binding of Fab'-DNA-Atto647N to the membrane (Supplementary Fig. 6).

Single molecule TIRF imaging confirmed that both Atto647N- and AlexaFluor555-labeled Fab'-DNA molecules on the supported membrane were single-species and uniformly labeled

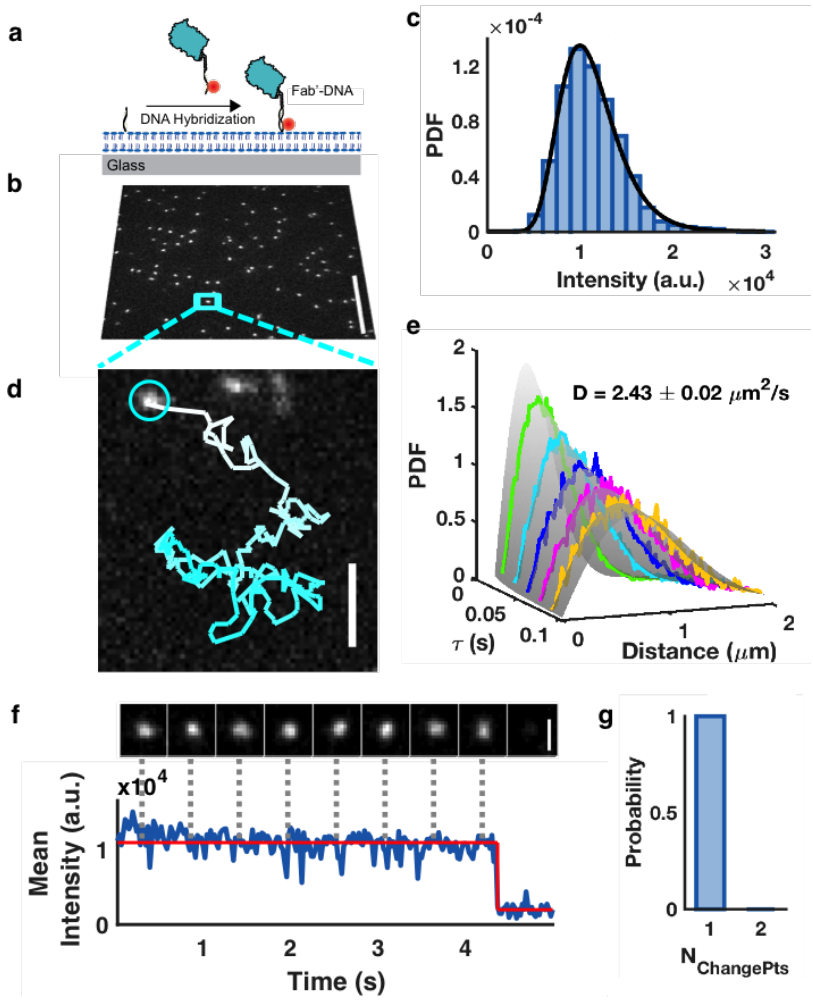

Figure 2.3: Single molecules of Fab'-DNA diffuse freely as monomers on supported lipid bilayers. a. Fab'-DNA was conjugated to SLBs composed of 95% DOPC, 2% Ni-NTA-DOGS, and 3% MCC-DOPE phospholipids via DNA complementation with a membrane-tethered oligonucleotide. **b.** Single particles of Fab'-DNA were clearly resolved with a 20 ms exposure time and 11 mW power at the sample. Scale bar 10 μm. **c.** The intensity distribution of single particles fit a lognormal distribution, consistent with uniform, singly labeled species (n = 16,215 unique particles). **d.** A representative trajectory of a particle freely diffusing in two dimensions on the bilayer. Scale bar 2 μm. **e.** Step size distributions of Fab'-DNA at multiple delay times (τ = 29, 43, 58, 72, and 87 ms), fit simultaneously by a single component 2D diffusion model with a diffusion constant of $2.43 \pm 0.02\ \mu m^2/s$ (n > 50,000 steps). Error denotes the 95% confidence interval. **f.** Montage and intensity trace of the particle tracked in (d), representative of 99 analyzed trajectories. This particle underwent a single step photobleaching event. Scale bar 1 μm. **g.** Number of change points in intensity traces of particles that bleached within the field of view (n = 99). All particles bleached in a single step. Fab'-DNA-Atto647N was used for all data in this figure. Data are collected at 37 °C and are representative of at least three independent experiments.

with a single fluorophore. Single molecule images were detected and linked into trajectories using the FIJI plugin, TrackMate (Figs. 3B-3D, Supplementary Fig 7) [85]. The intensity distribution, calculated from the background-subtracted mean intensities of typically 10,000 – 20,000 unique particles per experiment, were well fit by a lognormal distribution, which results from convolution of Poisson distributed photon emission events with the multiplicative error inherent to EMCCD cameras (Fig. 2.3C) (67). Particles undergo 2-dimensional Brownian motion (Fig. 2.3D), and their step size distribution is well fit by a single component diffusion model,

$$\rho(r, \tau, D) = \frac{r}{2D\tau} exp(\frac{-r^2}{4D\tau}) \tag{2.1}$$

with molecular displacement, r, and the corresponding time interval, τ. The resulting diffusion coefficients, D, were obtained through a multi-delay time fit protocol (see Methods), and found to be $2.43 \pm 0.02\,\mu m^2/s$ for Atto647N-labeled Fab'-DNA (Fig 3E; Supplementary Fig 8) and $5.41 \pm 0.04\,\mu m^2/s$ (Supplementary Fig. 9) for the AlexaFluor555-labeled species. The mobility of the AlexaFluor555-labeled construct is somewhat higher than the mobility of K-Ras4B at room temperature covalently attached to an SLB by the same maleimide-cysteine linkage of 4.5 $\mu m^2/s$ [91], but this difference could be accounted for by the higher temperature (37 °C) used in this study and differences in bilayer composition [92]. The much slower diffusion of Fab'-DNA-Atto647N may be because Atto647N interacts significantly with the SLB. Atto647N has a high membrane interaction factor of 13, and dye intercalation into the SLB may slow the Atto647N construct relative to the construct labeled with AlexaFluor555, which has a membrane interaction factor of 0.3 [93]. It is unlikely that AlexaFluor555 weakens annealing between complementary oligonucleotides and leads to hopping of Fab'-DNA between SLB-tethered oligos, thereby increasing observed diffusion rates, because Fab'-DNA-AlexaFluor555 density is stable on SLBs at 37 °C through time (data not shown) and it remains bound to TCR under tension with the same mean dwell time as Fab'-DNA-Atto647N (Supplementary Fig. 11). Because both Atto647N and AlexaFluor555 Fab'-DNA constructs interact with TCR with the same binding kinetics, choice of fluorophore does not appear to influence the functionality or characterization of Fab'-DNA ligands. The hypothesis that Atto647N interacts with the SLB and slow diffusion could be tested using long SLB-tethered complementary oligos that allow separation between the SLB and the dye [48]. Preliminary analysis of SLB-bound Fab'-DNA with a 76-mer poly(dT) spacer between the SLB and the complementary DNA sequence suggested a diffusion coefficient of 3.25 ± 0.05 $\mu m^2/s$, though more careful data acquisition and analysis are needed for this construct.

When linked into trajectories, all particles analyzed were observed to photobleach in a single step (Fig. 2.3F-G), indicating that all of the Fab'-DNA molecules on the membrane are uniformly monomeric and labeled 1:1 with fluorophore (Atto647N or AlexaFluor555). This

was expected based on the biochemical analysis, described above, which also ruled out Fab' [94]- or DNA-mediated oligomerization.

Fab'-DNA binds TCR with high affinity

Primary AND $CD4^+$ T cell blasts were isolated from the lymph nodes and spleens of first generation AND × B10.BR mice. The cells were stimulated with moth cytochrome c (amino acids 88-103) (MCC) peptide immediately after harvest in order to induce the differentiation of T cells expressing the AND TCR, and IL-2 was added 24 h after harvest to promote proliferation. T cells used to image localization of intracellular signaling proteins were retrovirally transduced on day 3, and all cells were imaged on days 5 to 7 (further detailed in Methods) [83]. Cell viability, proliferation, morphology, and activation in response to high densities of agonist pMHC were used as indicators of cell health.

After equilibration of the imaging chamber to physiological temperature (37 °C), T cells were added to a supported membrane bearing fluorescently labeled Fab'-DNA and ICAM-1, prepared as described above (Fig. 2.4A). The T cell-APC interface was imaged by reflection interference contrast microscopy (RICM). RICM imaging revealed the expected T cell landing and spreading on the supported membrane, forming a T cell-supported membrane junction within which Fab'-DNA:TCR binding interactions occur (Fig 4B). As demonstrated in previous work, pMHC mobility slows significantly upon TCR binding, allowing bound pMHC to be clearly resolved from free pMHC based on mobility differences. Use of long (500 ms) exposure times and low excitation power (0.8-1.0 mW at the sample) in total internal reflection fluorescence (TIRF) microscopy selectively resolves bound pMHC:TCR complexes in each image frame [8, 9, 47, 95]. This imaging strategy was employed to image single Fab'-DNA:TCR binding and unbinding events (Fig. 2.4A-C). Like pMHC, Fab'-DNA:TCR complexes are actively transported to the geometric center of the cell (Fig. 2.4E). The error rate for misidentifying Fab'-DNA:TCR complexes, determined by analyzing apparent binding events outside the boundaries of the T cell—where no genuine binding can occur—was measured to be 0.2% (Fig. 2.4C).

Single molecule in situ measurements of Fab'-DNA:TCR two dimensional kinetic off-rate, k_{off}, and binding efficiency indicate that Fab'-DNA is a stronger binder to TCR than a potent agonist peptide ligand, MCC pMHC binding to AND TCR. The mean pMHC:TCR binding dwell time, $\langle \tau_{off} \rangle$, is equal to $1/k_{off}$, for first order binding kinetics. Single molecule binding dwell time distributions for each ligand were compiled by tracking individual binding events through time using the FIJI plugin TrackMate (Fig. 2.4B,D, Supplementary Fig. 10). $\langle \tau_{off} \rangle$ for these distributions was determined by fitting observed dwell time histograms $p((\tau_{obs}))$ and measured fluorophore bleaching rates $(\langle \tau_{bl} \rangle^{-1})$ based on first order kinetics (Fig 4F):

$$p(\tau_{obs}) = (\langle \tau_{bl} \rangle^{-1} + \langle \tau_{off} \rangle^{-1}) * exp(-\tau_{obs}(\langle \tau_{bl} \rangle^{-1} + \langle \tau_{off} \rangle^{-1})) \tag{2.2}$$

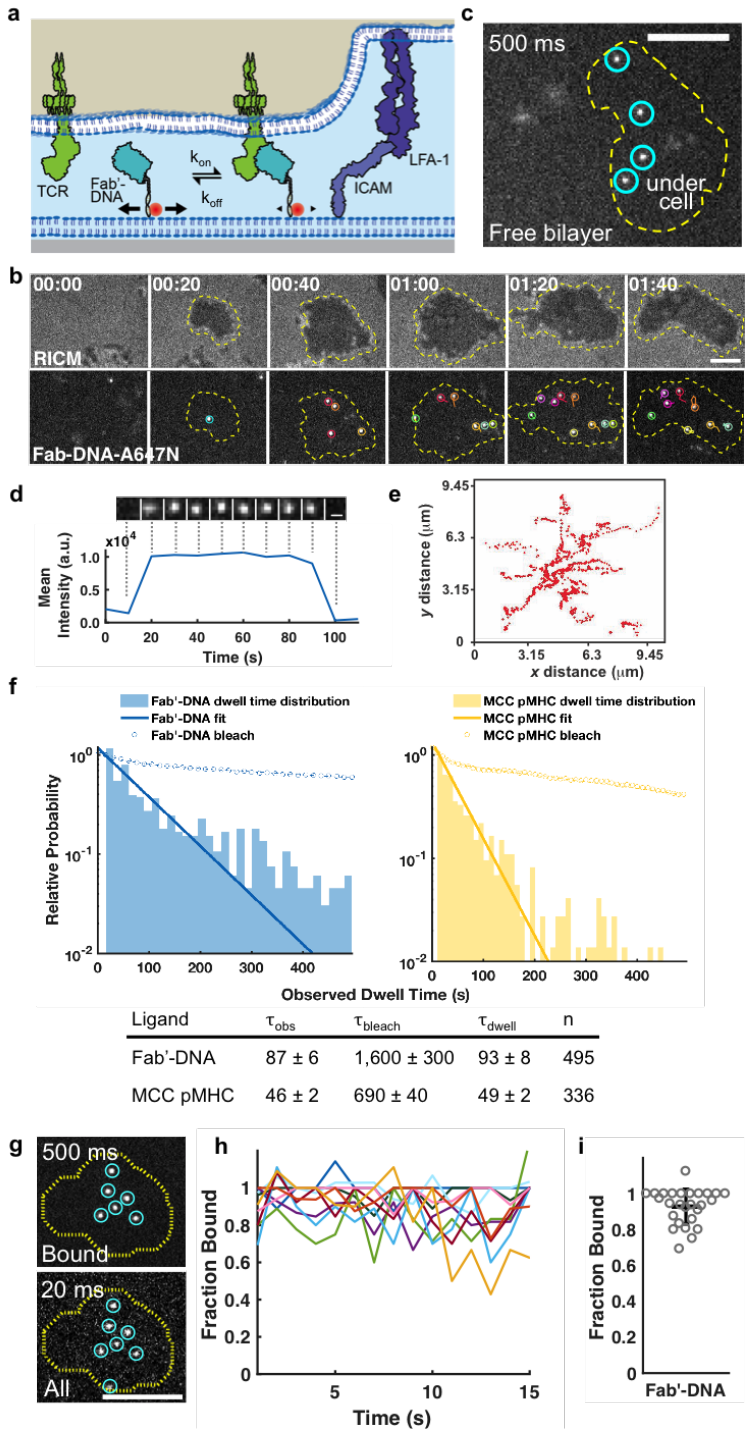

Ligand	τ_{obs}	τ_{bleach}	τ_{dwell}	n
Fab'-DNA	87 ± 6	1,600 ± 300	93 ± 8	495
MCC pMHC	46 ± 2	690 ± 40	49 ± 2	336

Figure 2.4: Single molecule Fab'-DNA:TCR complexes can be visualized under living T cells. a. Binding of Fab'-DNA to TCR occurs at the interface between a living T cell and an SLB. Upon binding, Fab'-DNA motility dramatically decreases. **b.** Montage of a T cell landing and binding Fab'-DNA-Atto647N on the bilayer. Scale bar 5 μm. **c.** Long, 500 ms exposure time resolved Fab'-DNA:TCR complexes under the T cell and unbound ligands were blurred. 99.8% of slow-moving Fab'-DNA that are resolved using this method appear within the T cell boundary. Scale bar 5 μm. **d.** Representative montage and corresponding intensity trace for a single Fab':TCR binding event shows single step binding and unbinding. Scale bar 0.5 μm. **e.** A spatiotemporal map of Fab':TCR binding events at the interface between a live T cell and a supported membrane. Each dot represents a single Fab':TCR binding event in a single image frame and all time points are plotted simultaneously. **f.** Dwell time distributions for Fab'-DNA and MCC pMHC. Data were collected from at least 5 cells in at least 3 independent experiments. Error: SD. **g.** Representative images of bound (upper) and all (lower) Fab'-DNA-Atto647N under a T cell at a given time point. **h.** Fab'-DNA-Atto647N fraction bound through time, n=10 cells. **i.** Fab'-DNA-Atto647N fraction bound was 0.93 ± 0.09, n = 27 cells, error: SD.

Fit parameters are used rather than the average of measured dwell times because the measured data convolve uneven sampling of the dwell time distribution (32). The Fab'-DNA:TCR binding interaction is significantly longer than the MCC pMHC:TCR, and a variety of technical factors lead to systematic undercounting of long Fab'-DNA:TCR dwell times (see Methods). Thus the measured apparent Fab'-DNA:TCR mean dwell time of 93 $\pm$ 8 s is an underestimate. The measured mean dwell time for MCC and T102S pMHC binding AND TCR are 49 $\pm$ 2 s and 8.3 $\pm$ 0.5 s, respectively (31). Extremely low densities of Fab'-DNA ($0.01 - 0.03\ \mu m^{-2}$) are used in dwell time experiments to track single particles for tens of seconds to minutes as reliably as possible. The mean Fab'-DNA dwell time measurements do not depend on the fluorophore label (Supplementary Fig. 11). At higher densities of Fab'-DNA ($0.2\ \mu m^{-2}$) the long Fab'-DNA:TCR dwell time enables observation of transient merging of Fab'-DNA:TCR in diffraction-limited areas, consistent with observations of TCR clustering in response to pMHC ligand (Supplementary Fig. 12A). Co-localized single molecule Fab'-DNA and ZAP70-EGFP pairs are observed to merge and split from other Fab'-DNA/ZAP70 pairs while traveling along linear trajectories (Supplementary Fig. 12B-D), confirming that the TCRs also merge and split within these diffraction-limited areas.

In situ binding measurements indicate that Fab'-DNA also binds the TCR with a higher efficiency than the potent agonist MCC pMHC. Comparison of bound ligand to all available ligands at long (500 ms) vs. short (20 ms) exposure times, respectively, enables direct measurement of the fraction of ligands bound to TCR underneath a T cell (Fig. 2.4G) [8]. This observable represents the efficiency of ligand:receptor binding and, when coupled with quantification of TCR density, can be used to determine the in situ affinity and kinetic on-rate, k_{off} [8]. Using this technique, nearly all (0.93 $\pm$ 0.09) of the Fab'-DNA was observed to be bound to TCR (Fig. 2.4H-I). By comparison, at most 80% and as few as 50% of the strong agonist MCC pMHC, depending on the pMHC density, and at most 30% of the weak agonist T102S pMHC is typically observed bound to AND TCR [8].

Immunological synapse formation

After extended periods of time (10-30 minutes), T cells interacting with Fab'-DNA- and ICAM-1-functionalized membranes form characteristic immunological synapse patterns (Supplementary Fig. 13). However, while cells exposed to high density MCC pMHC retain large, uniform footprints on bilayers for up to 6 hours, a large fraction of cells on high density Fab'-DNA bilayers are detected to have minimal contact with the bilayer after 1 hour, as visualized by RICM, despite robust landing and spreading and accumulating tens to hundreds of Fab'-DNA:TCR binding events (Supplementary Fig. 14).

Fab'-DNA triggers ZAP70 recruitment and calcium signaling

AND T cells transduced with a ZAP70-EGFP transgene were used to measure real-time triggering of the TCR at sites of Fab'-DNA:TCR binding (Supplementary Fig. 12B). As in a previous report [47], Fab'-DNA and ZAP70-EGFP were simultaneously imaged with sub-pixel location accuracy using a dichroic mirror to project the two channels onto distinct regions of an EMCCD camera. Step increases in ZAP70-EGFP intensity were observed in spatial correspondence with individual Fab'-DNA:TCR trajectories (Supplementary Fig. 12E), confirming TCR triggering by single molecule Fab'-DNA:TCR binding events.

Monovalent Fab'-DNA only activates T cells and acts as a TCR agonist when tethered to an opposing surface (Supplementary Fig. 15). T cell activation was monitored by intracellular Ca^{2+} flux using fluorescence ratio imaging of fura-2 dye. The timing and duration of Ca^{2+} flux can be heterogeneous at the single cell level [46], so T cells were imaged for 20 minutes at intervals of 15 s in order to achieve optimal signal fidelity. More T cells fluxed Ca^{2+} when exposed to Fab'-DNA-conjugated supported membranes compared to T cells exposed to comparable densities of MCC pMHC. When the same Fab'-DNA was allowed to bind T cells from solution, the number of T cells fluxing calcium was negligible and similar to the response to a null peptide, T102E pMHC. This result is consistent with previous extensive use of the H57 Fab' fragment as a solution-phase TCR label, which neither activates the receptor nor interferes with activation by pMHC [8, 12, 65, 70, 79, 80]. The ability for membrane-tethered Fab' to stimulate Ca^{2+} flux is also consistent with force spectroscopy experiments that report Ca^{2+} flux upon applying either shear or normal force to a single half antibody at a T cell–bead interface [70].

Membrane-tethered Fab'-DNA is a potent agonist

Nuclear localization of NFAT-EGFP is a reliable indicator of early T cell activation and has been used as a quantitative readout for activation of the Ca^{2+} signaling pathway in precision ligand density titrations [8, 9, 82]. T cells transduced with NFAT-EGFP were allowed to interact with supported membranes presenting ICAM-1 and either Fab'-DNA, MCC pMHC, or T102S pMHC. Inclusion of the T102S ligand in these experiments serves as a benchmarking control because the affinity and kinetic off-rate of this ligand with AND TCR is more similar to the native MCC pMHC:5C.C7 TCR interaction [8, 9, 96]. Within minutes of productive ligand:TCR binding, NFAT translocates to the nucleus, providing a binary readout of single T cell activation (Fig. 2.5A). At each density, cells were fixed 15 minutes after being introduced to the bilayer, and the fraction of cells that had translocated NFAT, defined as the fluorescence within the nucleus equal to or greater than the fluorescence in the cytosol, was counted (Fig. 2.5C). Using this assay, the NFAT activation threshold of the Fab'-DNA reagent was measured to be nearly identical to that of MCC pMHC at $0.2\ \mu m^{-2}$ (Fig. 2.5C), and both were significantly stronger than T102S pMHC. Because Fab'-DNA has a higher affinity for AND TCR than MCC pMHC and ligands are laterally mobile, cells on

Fab'-DNA-conjugated membranes serve as concentration sinks, and they have more ligand bound at any given moment than cells on MCC pMHC-conjugated membranes at matched surface density (Supplementary Fig. 16A) [8]. Through time, T cells on Fab'-DNA bilayers also experience more binding events than cells on MCC pMHC bilayers when bilayers are density-matched. At the threshold density of 0.2 μm^{-2}, cells on Fab'-DNA bilayers are estimated to experience 260 ± 100 Fab'-DNA:TCR binding events from initial landing to NFAT translocation (Supplementary Fig. 16B-C), compared to 30 ± 10 events for MCC pMHC [9]. NFAT nuclear translocation is observed in response to Fab'-DNA densities as low as 0.08 μm^{-2} (Fig. 2.5C-D), corresponding to an estimated 110 ± 50 Fab':TCR binding events (Supplementary Fig. 16B-C), setting this as the observed lower limit of Fab'-DNA input necessary to stimulate T cell activation.

The membrane-tethered Fab'-DNA reagent binds the TCR in the constant β region and, unlike pMHC ligands, can therefore bind TCR clonotypes that differ in their variable pMHC binding region (Fig. 2.1C-E). To confirm this universality, we generated a mixed population of T cells with varying peptide specificity and measured their NFAT response to Fab'-DNA- and pMHC-conjugated membranes. A subset of primary T cells isolated from AND transgenic mice were expanded on anti-CD3/anti-CD28 coated tissue culture plates, while the remainder were differentiated via MCC incubation, as in all other experiments in this report (Fig. 2.5B). Because the AND transgenic mice used are not homozygous Rag2 knockouts, expansion via non-peptide specific anti-CD3 stimulation produces a population of T cells with varying peptide specificity. When exposed to Fab' supported membranes, T cells expanded via anti-CD3 stimulation had an almost identical fractional activation as T cells expanded via MCC incubation (Fig. 2.5C-D). In comparison, T cells expanded via anti-CD3 stimulation exhibited a lower fraction of activated cells when exposed to MCC pMHC supported membranes (Fig. 2.5C-5D). Regardless of the expansion technique, T cells exposed to MCC pMHC or Fab'-DNA supported membranes had similar activation threshold ligand densities and expressed similar densities of TCR (Supplementary Fig. 17).

IL-2 production was characterized using an enzyme-linked immunosorbent assay (ELISA). T cells were exposed to supported membranes displaying ICAM-1 only, ICAM-1/Fab'-DNA, or ICAM-1/MCC pMHC for 6 hours and the supernatants were analyzed for IL-2 concentration. Cells exposed to either agonist pMHC or Fab'-DNA produced appreciably more IL-2 than observed on the ICAM-1 only control (Table 2.2).

2.6 Discussion

The H57 Fab'-DNA ligand recapitulates several emergent properties of pMHC ligands. First, it is strictly monovalent (Fig. 2.2 and Fig. 2.3) and only active when tethered to an opposing surface (Supplementary Fig. 15). Second, Fab'-DNA:TCR binding stimulates recruitment of Zap70 (Supplementary Fig. 12), calcium flux (Supplementary Fig. 15), NFAT translocation

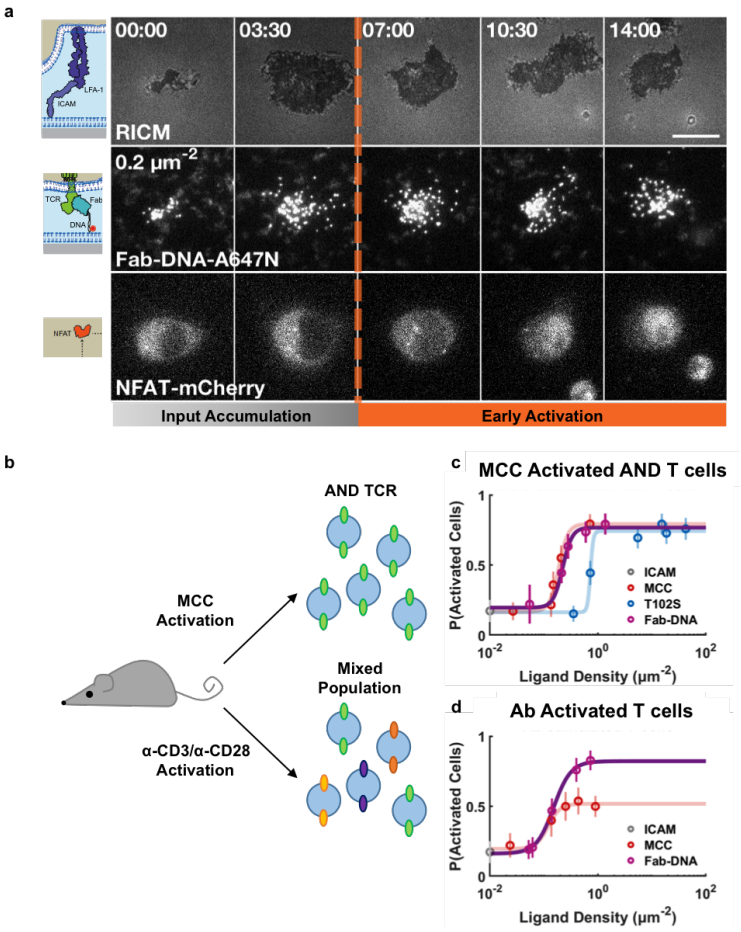

Figure 2.5: Fab'-DNA universally activates NFAT in mixed T cell population. a. Representative time trace shows an NFAT-EGFP expressing T cell landing and spreading onto a supported lipid bilayer (top row), accumulating Fab'-DNA:TCR binding events (middle row, Fab'-DNA-Atto647N at 0.2 μm^{-2}), and initiating NFAT activation and nuclear translocation (bottom row). Phases of input (TCR binding event) accumulation (gray gradient bar) and early cellular activation (NFAT translocation; orange bar) are indicated. The initial cellular decision to activate was defined as the time point when NFAT translocation is first observed (orange dashed line). Scale bar 10 μm. **b.** Diagram of the approach to generate different T cell populations. Transgenic, primary T cells are harvested from mouse lymph nodes and spleens. The harvested T cells were activated either with the agonist pMHC to generate a pure population of mature, AND TCR T cells, or with anti-CD3 and anti-CD28 antibodies to generate a population of T cells expressing a mixture of different TCRs. **c-d.** The fraction of NFAT activated cells in a population as a function of bilayer ligand identities and densities for the pure population of AND TCR T cells in c or for the mixed population of T cells in d. Due to the high affinity of Fab'-DNA, cells on Fab'-DNA-conjugated membranes experience more binding events at matched ligand density compared to those on pMHC-conjugated membranes (Supplementary Figure 16A). Error bars indicate standard error of the mean (n > 35 cells per condition).

(Fig. 2.5), and IL-2 production (Table 2.2). Third, quantitative density titrations reveal that Fab'-DNA and the strong agonist MCC pMHC have nearly identical NFAT translocation thresholds (Fig. 2.5).

However, H57 Fab'-DNA differs from pMHC in a handful of potentially important ways. First, the Fab' ligand cannot bind CD4 (Fig. 2.1). The peptide-independent CD4-MHC interaction has been identified as a modulator of Lck access to TCR, thus providing a tuning mechanism for antigen discrimination based on pMHC:TCR binding dwell time [97]. The Fab'-DNA ligand defeats this mechanism, presumably due to its extremely long dwell time (Fig. 2.4F). This is consistent with previous reports indicating that CD4 is most functionally relevant for lower affinity pMHC:TCR interactions [97]. The activity of the Fab'-DNA ligand conclusively demonstrates that CD4 engagement is not a strict requirement for NFAT activation. However, although the Fab' ligand defeats the CD4 dwell time tuning mechanism, it is also less efficient than MCC pMHC, which does engage CD4. The Fab' ligand is estimated to require 260 ± 100 Fab':TCR binding interactions to trigger half maximal NFAT translocation in a population of T cells (Supplementary Fig. 16B-C) compared to 30 ± 10 for pMHC [9], raising the possibility that CD4 coreceptor binding may trigger more potent or qualitatively distinct downstream signaling and not just enhance pMHC:TCR kinetics.

A crucial difference between H57 Fab'-DNA and MCC pMHC lies, by design, in their TCR binding epitope. A TCR ligand able to activate T cells universally must bind a constant region of the TCR complex, whereas pMHC binds the variable region. The qualitative similarities in all signaling readouts presented herein suggest that for a surface-tethered ligand, the dominant requisite feature of a TCR agonist may be, simply, that it binds the TCR complex. Notably, H57 Fab' binds the FG loop of TCRβ (Fig. 2.1), which has been shown to be a transducer of force in studies that carefully control the incident force acting of the TCR using optical trapping [20, 70, 78]. This raises the possibility that the Fab'-DNA triggers the TCR via non-chemically specific force, which is supported by the observation that Fab'-DNA triggers calcium flux only when tethered to a solid support (Supplementary Fig. 15). We note that our Fab'-DNA molecules are laterally fluid in the bilayer (Fig. 2.3), and therefore can only sustain force in the surface-normal direction [70]. Our results are also consistent with phosphatase exclusion [17, 18] and kinetic proofreading [26] models of T cell receptor triggering, and further work is required to test the contribution of each mechanism.

Another observable difference between Fab'-DNA and pMHC is noted in the context of cell adhesion. While cells remain strongly adhered to ICAM-1/MCC pMHC bilayers for many hours, cell engagement with ICAM-1/Fab'-DNA bilayers wanes after less than an hour. Thus, although the H57 Fab'-DNA activation of T cells looks very similar to agonist pMHC at early times, differences develop over time. Differences in adhesion between antibody- and agonist pMHC-stimulated cells have been reported [6, 32, 33]. Together with our observations, this suggests that some feedback between TCR activation and ICAM-1:LFA-1 adhesion is not effectively activated by antibody or the H57 Fab' binding to TCR.

The modular nature of the Fab'-DNA construct offers a variety of routes for modification. Fab' fragments derived from antibodies that bind alternative TCR epitopes may produce differential TCR triggering profiles, possibly as a result of the different force vectors involved. For example, pMHC:TCR interactions with relatively high affinity can fail to activate TCR based on structural nuances of their interaction, even when pMHC are displayed from membrane surfaces [24]. Similar ligand-mediated differential signaling effects have also been reported in NGF:EGFR versus EGF:EGFR signaling [98]. The length of the DNA oligonucleotide and the Fab' affinity can be modulated to test kinetic proofreading and kinetic segregation models in the context of these ligands [99]. Additionally, the Fab'-DNA construct is amenable to controlled heterodimerization [37] and more elaborate DNA origami techniques [100, 101], offering means to engage TCR and other co-receptors (e.g. CD4, CD28, etc.) in precisely defined stoichiometry and geometry.

A primary motivation for the development of a non-MHC restricted TCR agonist is the ability to trigger polyclonal T cell populations in a manner that closely resembles natural pMHC activation. Such a ligand would be useful for characterization of cell-to-cell variation in triggering thresholds and other aspects of tuning within the TCR signaling pathway. A similar approach could also be adapted to human anti-TCR antibodies to inform the design of T cell-based and BiTE-based immunotherapies.

2.7 Supplementary Materials

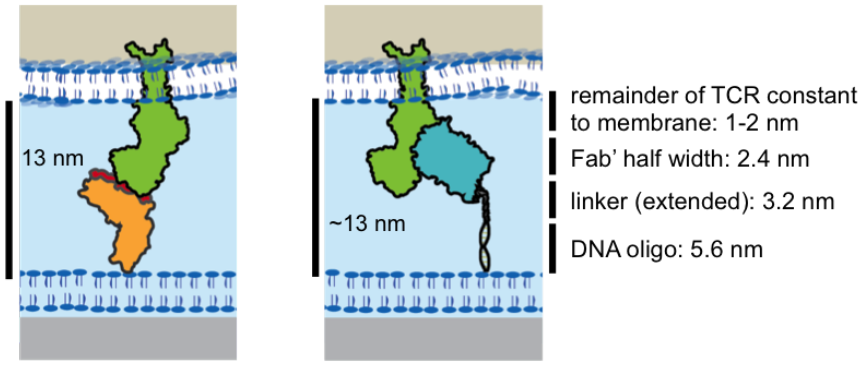

Figure 2.6: Supplementary Figure 1. Estimated Fab'-DNA:TCR complex dimensions. The intermembrane spacing from Fab'-DNA:TCR binding was estimated using PDB: 1NFD (H57Fab:TCR), and assuming the double stranded DNA oligonucleotide was rigid (dsDNA persistence length 50 nm) and that the linker was fully extended. The Fab'-DNA ligand was designed to approximate an intermembrane spacing comparable to pMHC (PDB: 3QIU).

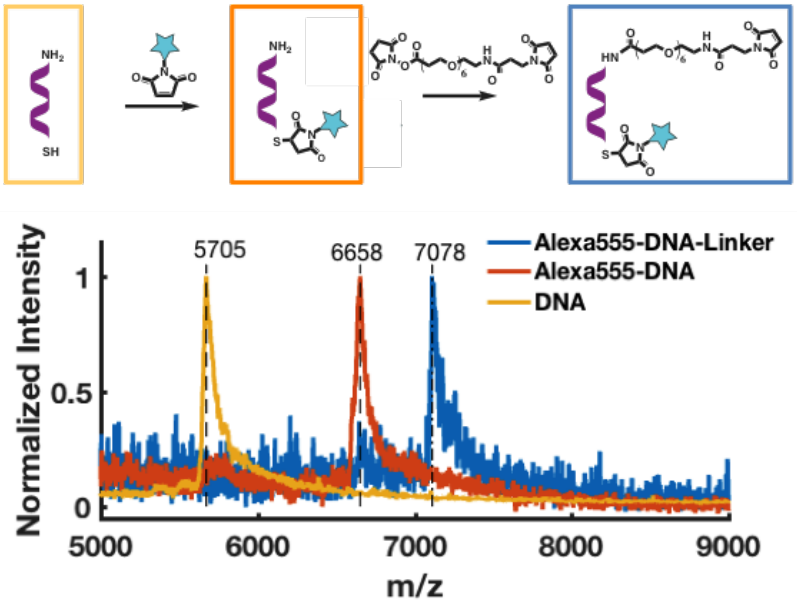

Figure 2.7: Supplementary Figure 2. MALDI spectra of DNA oligonucleotides with modifications. The DNA oligonucleotide with a 3' thiol group and 5' amino group (yellow) was first conjugated to AlexaFluor555 (red) or Atto647N (not shown) and then to an NHS-maleimide linker (blue). Any oligonucleotide lacking the NHS-maleimide linker is not able to conjugate to Fab'.

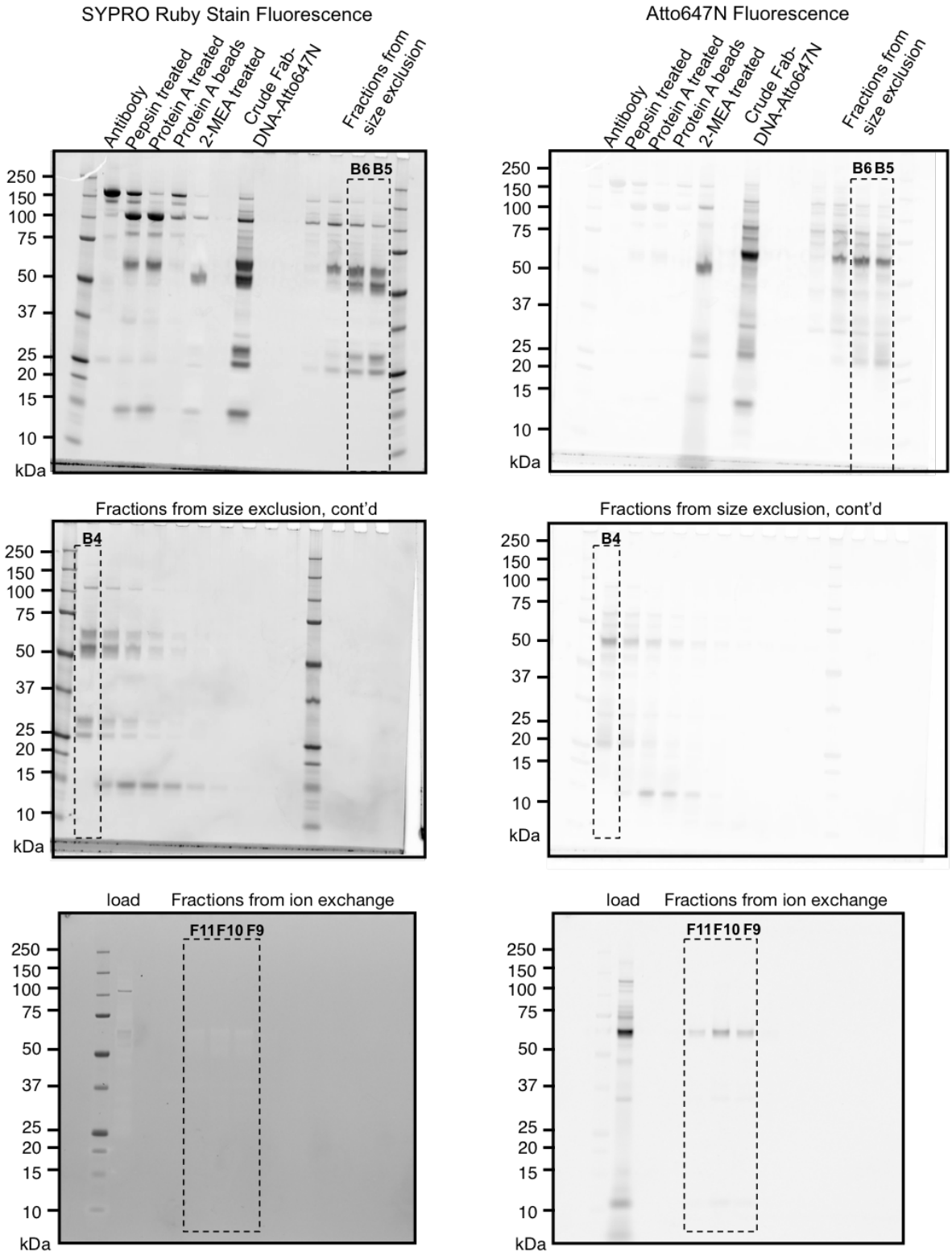
SYPRO Ruby Stain Fluorescence
Antibody
Pepsin treated
Protein A treated
Protein A beads
2-MEA treated
Crude Fab-DNA-Atto647N
Fractions from size exclusion
B6 B5
250
150
100
75
50
37
25
20
15
10
kDa
Atto647N Fluorescence
Antibody
Pepsin treated
Protein A treated
Protein A beads
2-MEA treated
Crude Fab-DNA-Atto647N
Fractions from size exclusion
B6 B5
250
150
100
75
50
37
25
20
15
10
kDa
Fractions from size exclusion, cont'd
B4
250
150
100
75
50
37
25
20
15
10
kDa
Fractions from size exclusion, cont'd
B4
250
150
100
75
50
37
25
20
15
10
kDa
load
Fractions from ion exchange
F11 F10 F9
250
150
100
75
50
37
25
20
15
10
kDa
load
Fractions from ion exchange
F11 F10 F9
250
150
100
75
50
37
25
20
15
10
kDa

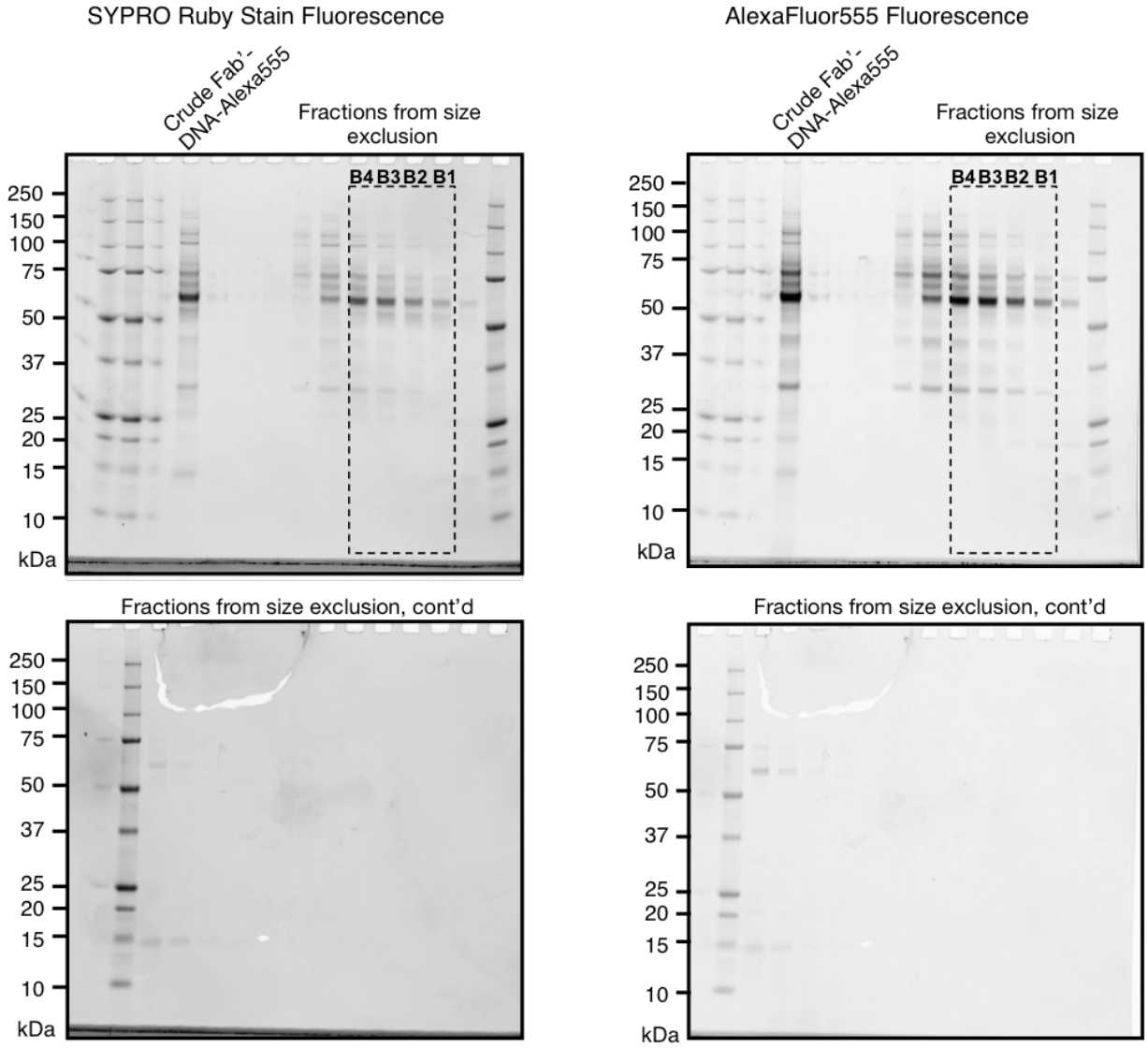
SYPRO Ruby Stain Fluorescence
AlexaFluor555 Fluorescence
Crude Fab'-DNA-Alexa555
Fractions from size exclusion
B4 B3 B2 B1
Fractions from size exclusion, cont'd
250
150
100
75
50
37
25
20
15
10
kDa

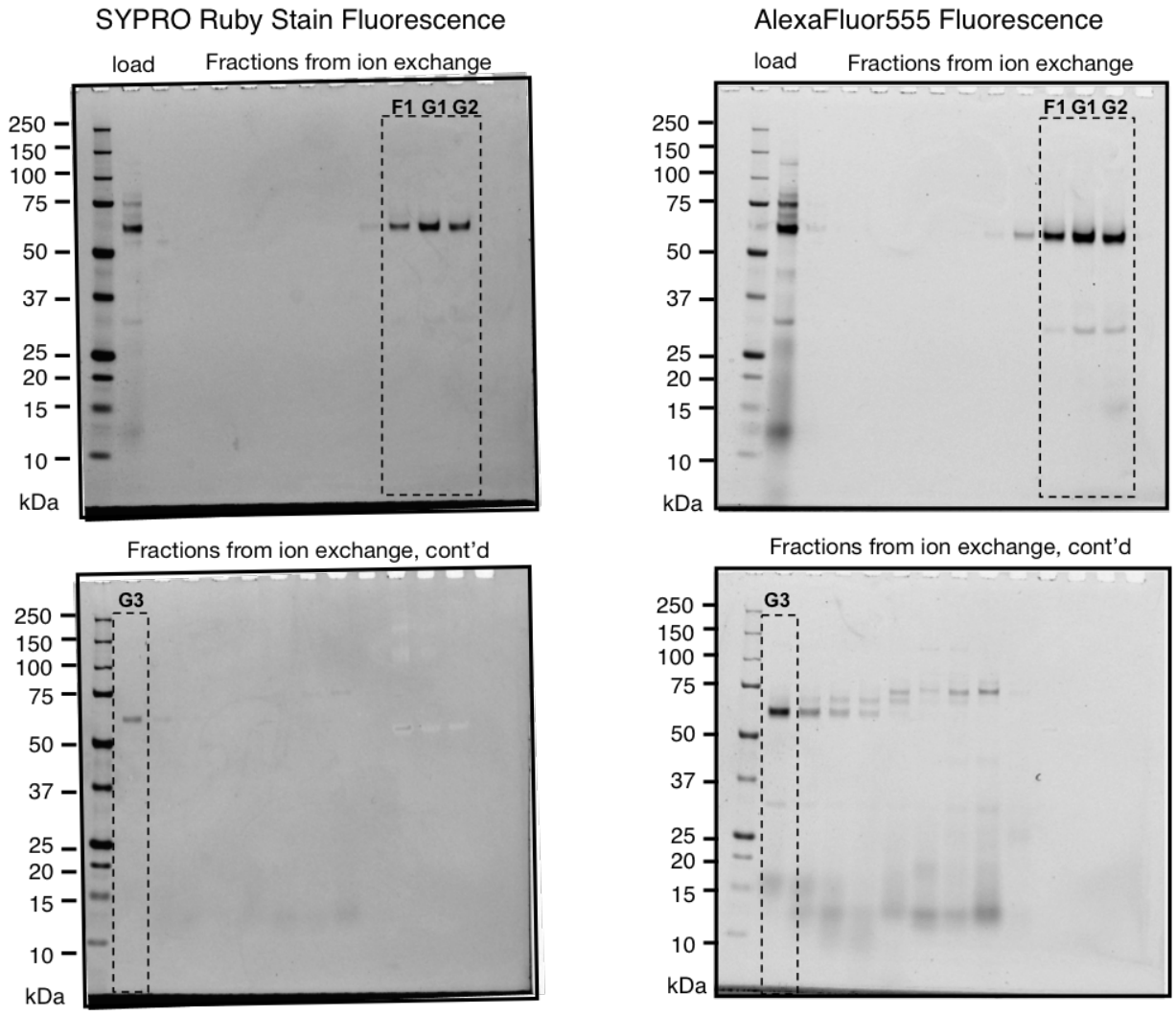

Figure 2.8: Supplementary Figure 3. Complete gels from H57 Fab' fragmentation, conjugation to DNA-Atto647N and DNA-AlexaFluor555, and purification over size exclusion and ion exchange columns. Size exclusion and ion exchange chromatography were necessary to purify Fab' labeled with a single fluorophore. Dashed boxes indicate fractions that were selected for further purification and for experiments after size exclusion and ion exchange, respectively.

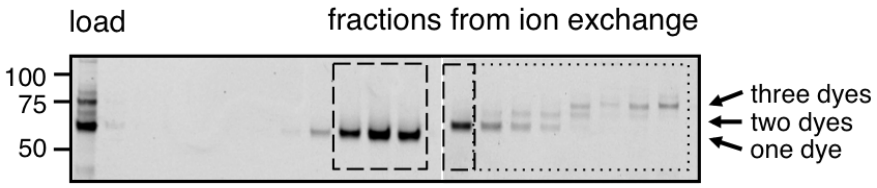

Figure 2.9: Supplementary Figure 4. Fab' molecules bound to one, two, or three DNA-AlexaFluor555 molecules. Clean separation after ion exchange chromatography is due to the high negative charge on the DNA oligonucleotides. Long dashes indicate singly labeled Fab'-DNA fractions used for further studies. Dots indicate fractions containing Fab's with multiple DNA oligonucleotides. This image is from the AlexaFluor555 fluorescence channel.

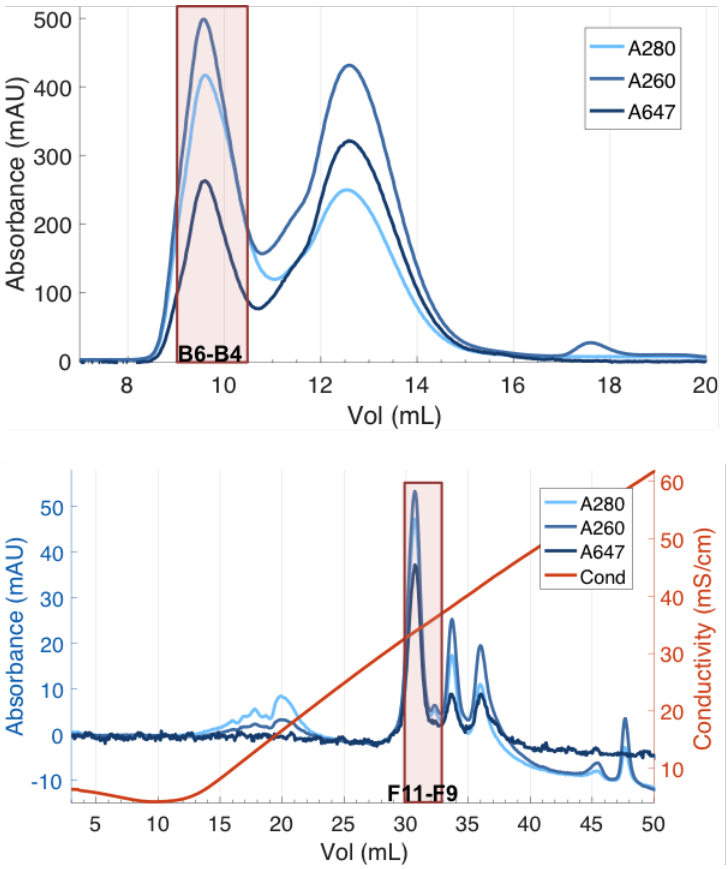

Figure 2.10: Supplementary Figure 5. Chromatograms from purification of H57 Fab'-DNA-Atto674N over Superdex 75 (top) and MonoQ (bottom) columns. Selected fractions are highlighted and correspond to boxed lanes in the full gels above.

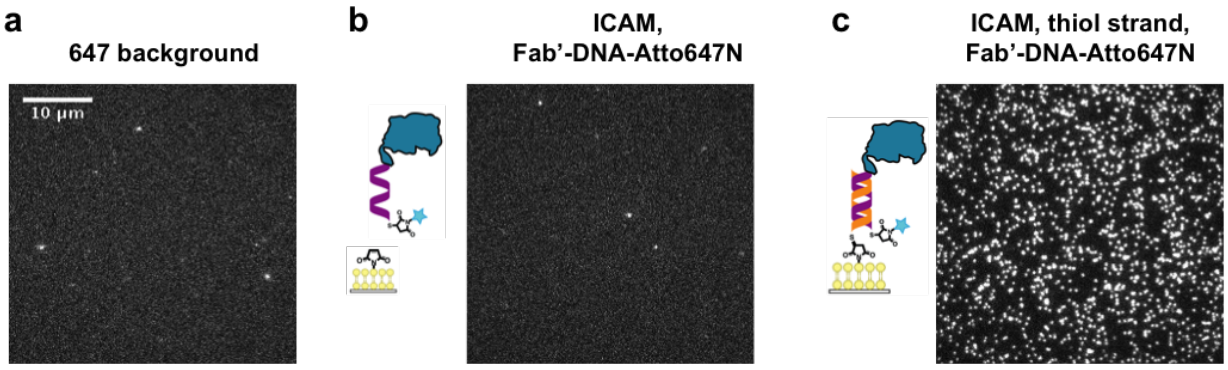

Figure 2.11: Supplementary Figure 6. Fab'-DNA needs the complementary strand in order to adhere to the bilayer. a. Fluorescence background on a sample without fluorescent species added. **b-c.** Fluorescence signal from a sample. **b.** without and c. with the 3'-thiol modified DNA oligonucleotide on the bilayer. Both chambers imaged were incubated with 140 pM Fab'-DNA-Atto647N. All images were taken with 5 mW power at the sample and 20 ms exposure time. Scale bar 10 μm.

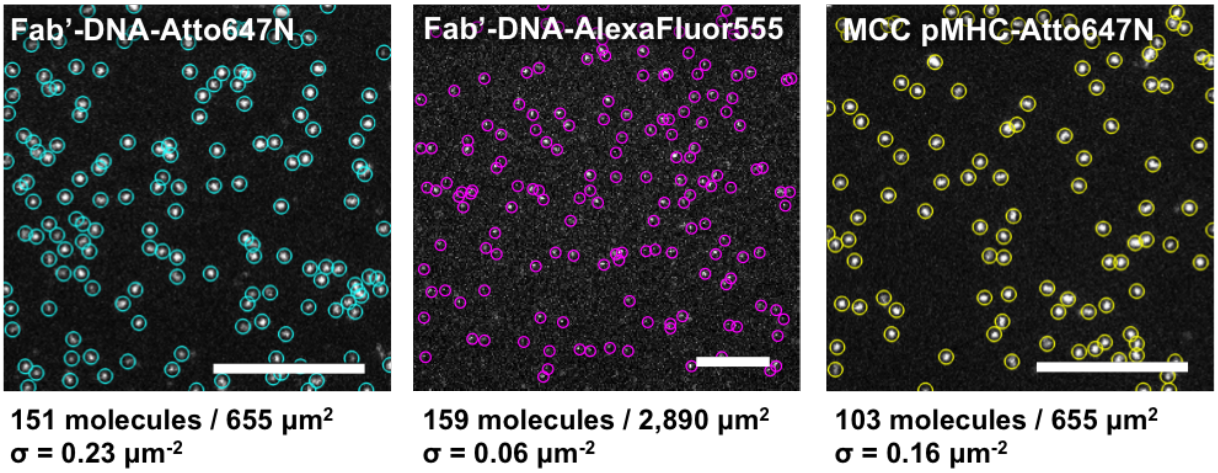

Figure 2.12: Supplementary Figure 7. Density calculations for Fab'-DNA and MCC pMHC. Images in the 640 and 555 channels were acquired with 11 and 9 mW power at the sample, respectively, and 20 ms exposure time. TrackMate was used for particle localization. Densities were calculated by dividing the number of particle localizations by the total area. Scale bars, 10 μm.

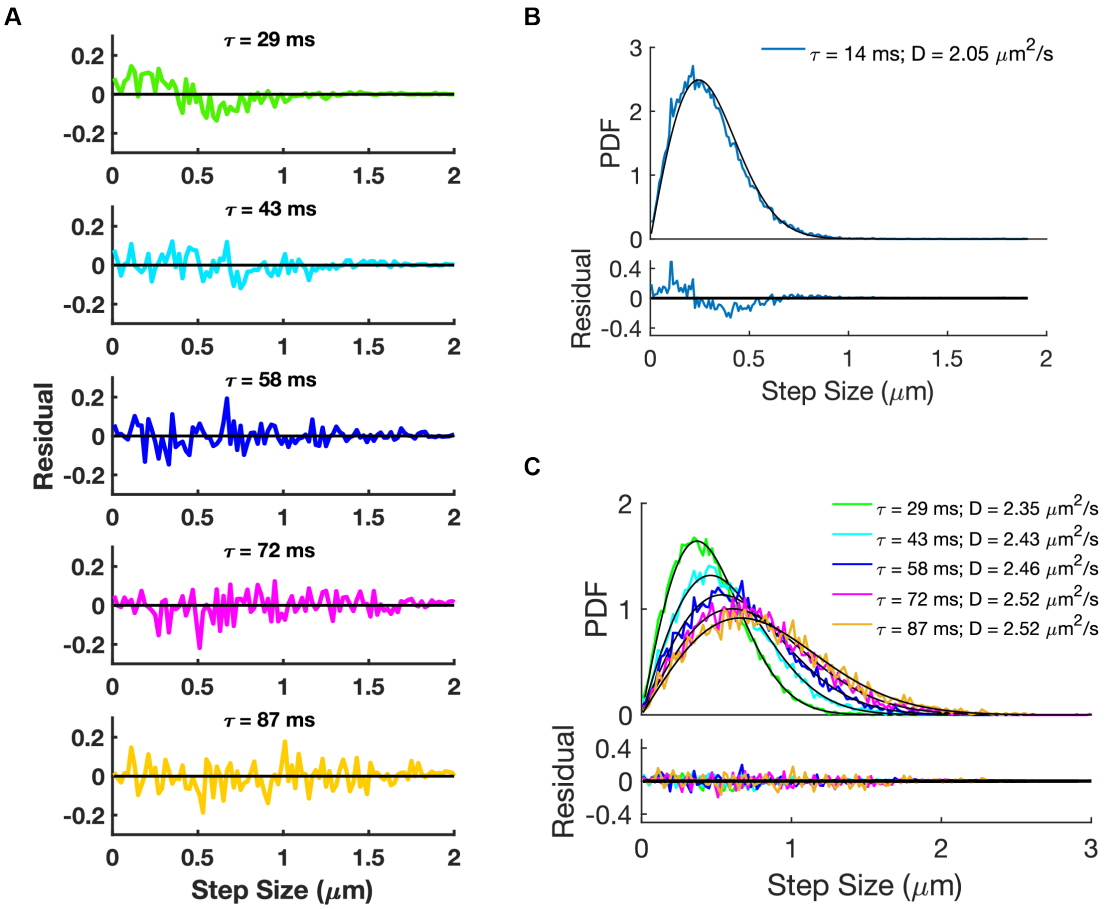

Figure 2.13: Supplementary Figure 8: Fab'-DNA-Atto647N diffusion analysis. a. Residuals from Fab'-DNA-Atto647N step size histograms at multiple time delays fit by a 2D single component diffusion model. Data from all time delays were fit simultaneously to obtain a single diffusion coefficient, as shown in Fig. 2.3E. **b.** The shortest measured time delay of 14 ms, between adjacent frames in the acquisition, was omitted from analysis due to irregularities in the distribution that likely result from systemic bias in the sub-pixel localization algorithm in TrackMate. The distribution exhibits regular spikes and poorly fits a single component diffusion model. These features become apparent when small step sizes are of a similar scale as the pixel size of 0.106 μm. **c.** Fitting step size distributions at each time delay separately and then averaging gives a mean diffusion coefficient of 2.46 $\pm$ 0.07 $\mu m^2/s$, which is similar to the result from the global fit of 2.43 $\pm$ 0.02 $\mu m^2/s$. This mean is affected by which distributions are considered, as measured diffusion coefficient correlates with the time delay used in analysis. Longer delay times were not included due to increasingly poor sampling of the distribution with fewer data points being used.

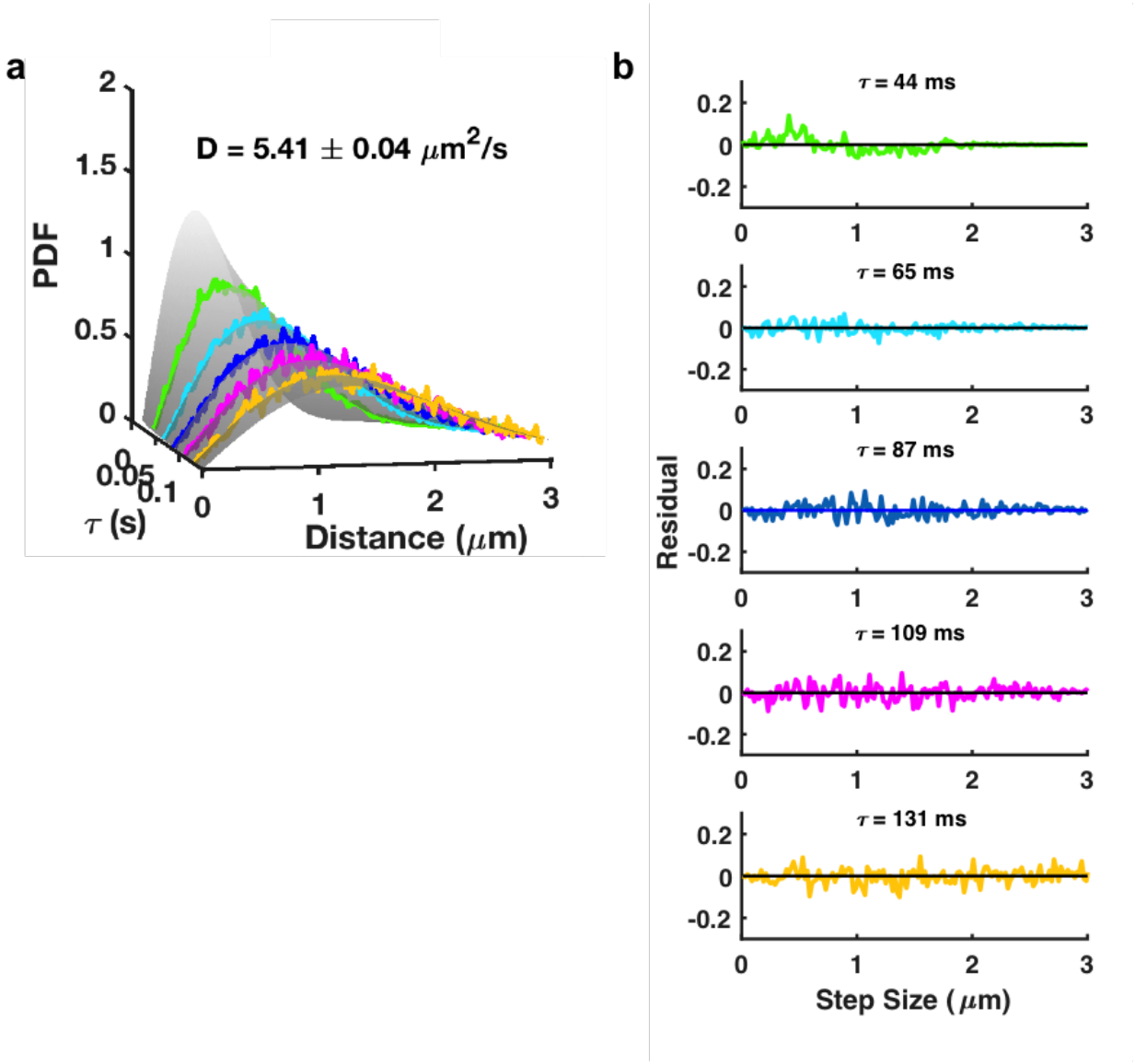

Figure 2.14: Supplementary Figure 9. Fab'-DNA-AlexaFluor555 step size distribution. The step size distribution of Fab'-DNA-AlexaFluor555 diffusing in two dimensions in a supported membrane fits a single species diffusion model with a diffusion coefficient D = 5.41 ± 0.04 $\mu m^2/s$. a. Step size distributions at multiple time delays (τ = 44, 65, 87, 109, and 131 ms) are simultaneously fit to extract a single diffusion coefficient. b. Residuals at each time delay.

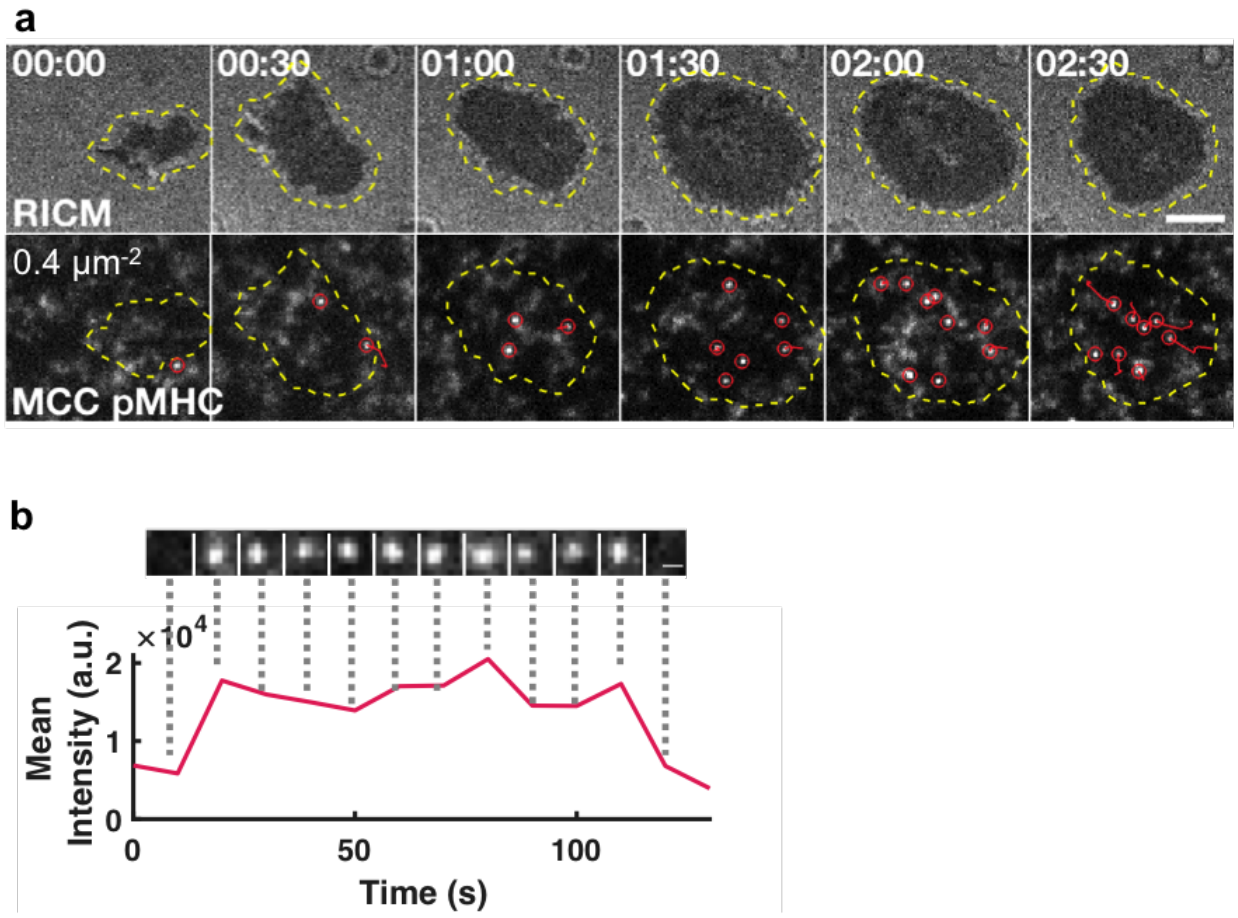

Figure 2.15: Supplementary Figure 10. Visualizing individual MCC pMHC:TCR binding events at the supported membrane – T cell interface. a. $CD4^+$ AND T cell lands and spreads on a supported membrane decorated with 0.4 μm^{-2} MCC pMHC and >100 μm^{-2} ICAM-1. Single pMHC:TCR binding events are visualized using 500 ms exposure time and a tracked through time using the FIJI plugin TrackMate. Binding events undergo directed motion to the geometric center of the cell. Scale bar 5 μ m. **b.** Representative kymograph and corresponding intensity trace for a single molecule MCC pMHC:TCR binding event. Scale bar 0.5 μm.

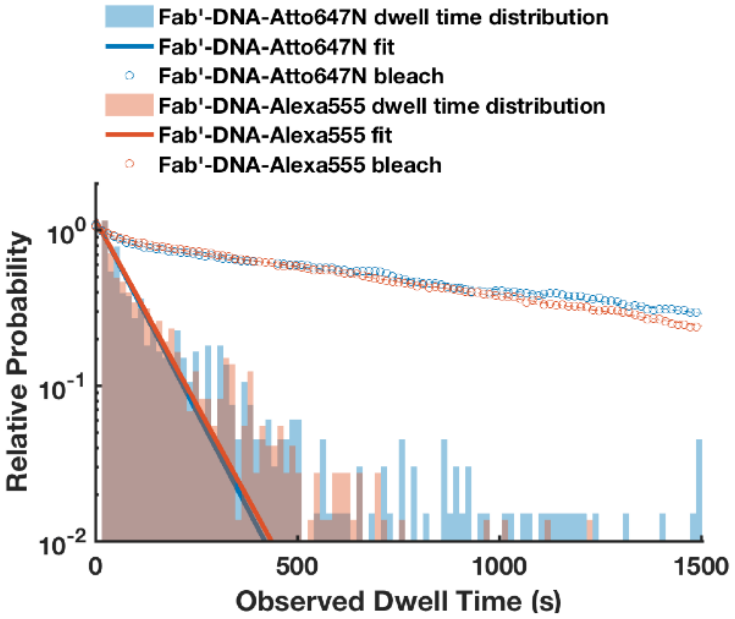

Ligand	τ_{obs}	τ_{bleach}	τ_{dwell}
Fab'-DNA-Atto647N	88 ± 6	1600 ± 300	93 ± 8
Fab'-DNA-AlexaFluor555	92 ± 5	1300 ± 300	98 ± 7

Figure 2.16: Supplementary Figure 11. Dwell time distributions For Fab'-DNA-Atto647N and Fab'-DNA-AlexaFluor555 interacting with the AND TCR. Photobleaching rates of the two dyes were the same within error. When corrected for photobleaching, the dwell time distributions were identical within error, confirming that the dye did not influence measured H57Fab':TCR binding kinetics.

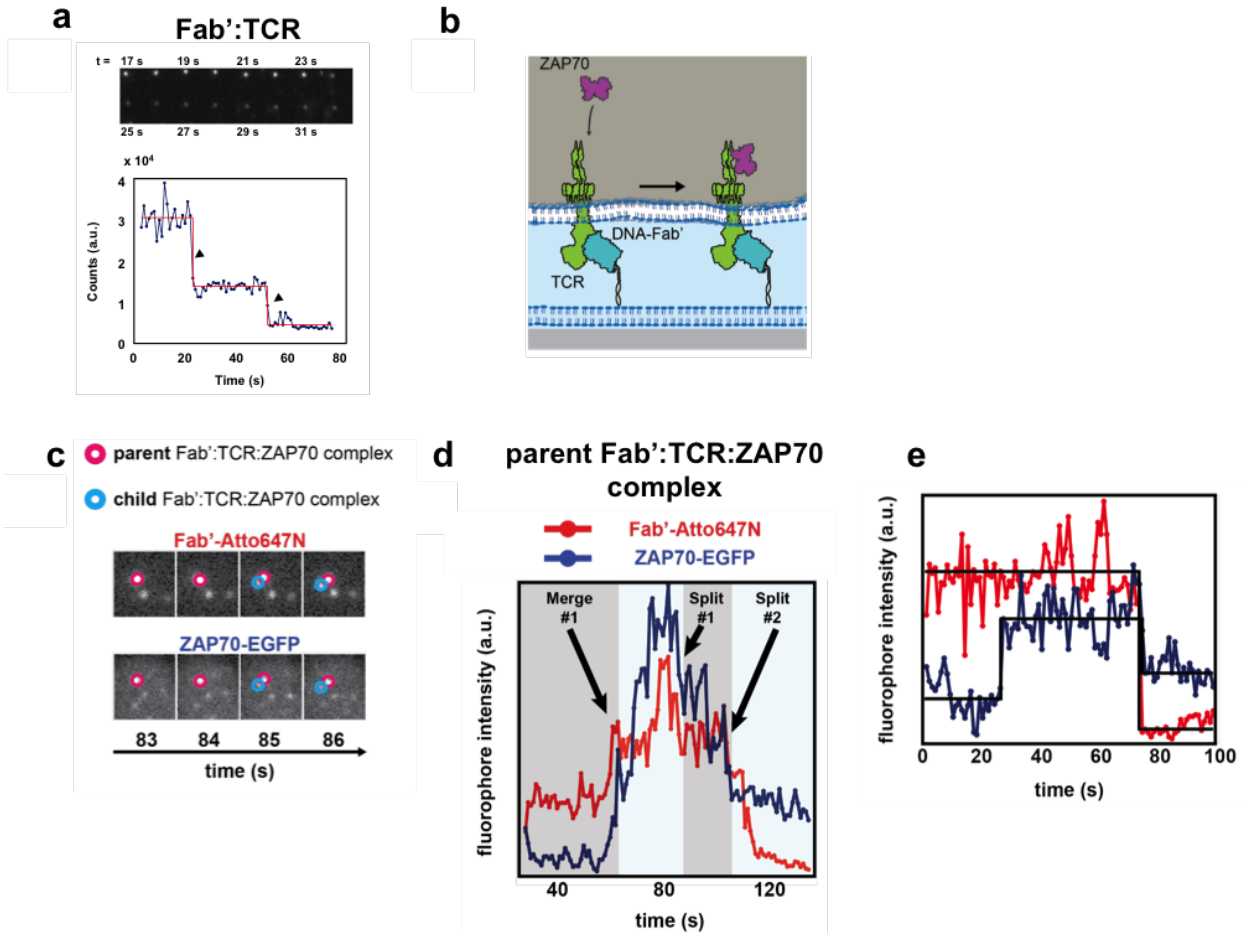

Figure 2.17: Supplementary Figure 12. Single molecule Fab' and ZAP70 imaging reports on TCR triggering. a. An intensity trajectory for a Fab':TCR interaction exhibiting multistep photobleaching. In the kymograph and in the intensity trace, multiple Fab':TCR co-transport over several seconds. The step down in intensity is due to either unbinding of a Fab':TCR interaction or photobleaching of the Atto647N fluorophore. Such trajectories with multi-step photobleaching patterns are observed at relatively high densities of Fab' (0.2 μm^{-2}). **b.** ZAP70 was recruited to ITAMs and acted as a readout of TCR triggering. **c.** Kymographs of Fab'-Atto647N and ZAP70-EGFP; a parent intensity feature split into a parent and child feature between 84 and 85 s. Splitting in the Fab'-DNA-Atto647N channel was mirrored by splitting in the ZAP70-EGFP channel. **d.** Fab' -DNA-Atto647N (red) and ZAP70-EGFP (blue) intensity traces for data in (c). Merging and splitting events, determined by Fab' intensity, are indicated by arrows. **e.** A representative single molecule Fab'-DNA intensity trace (red) exhibited single step photobleaching. ZAP70-EGFP intensity at the same spatial position had a step increase between 20 and 30 s.

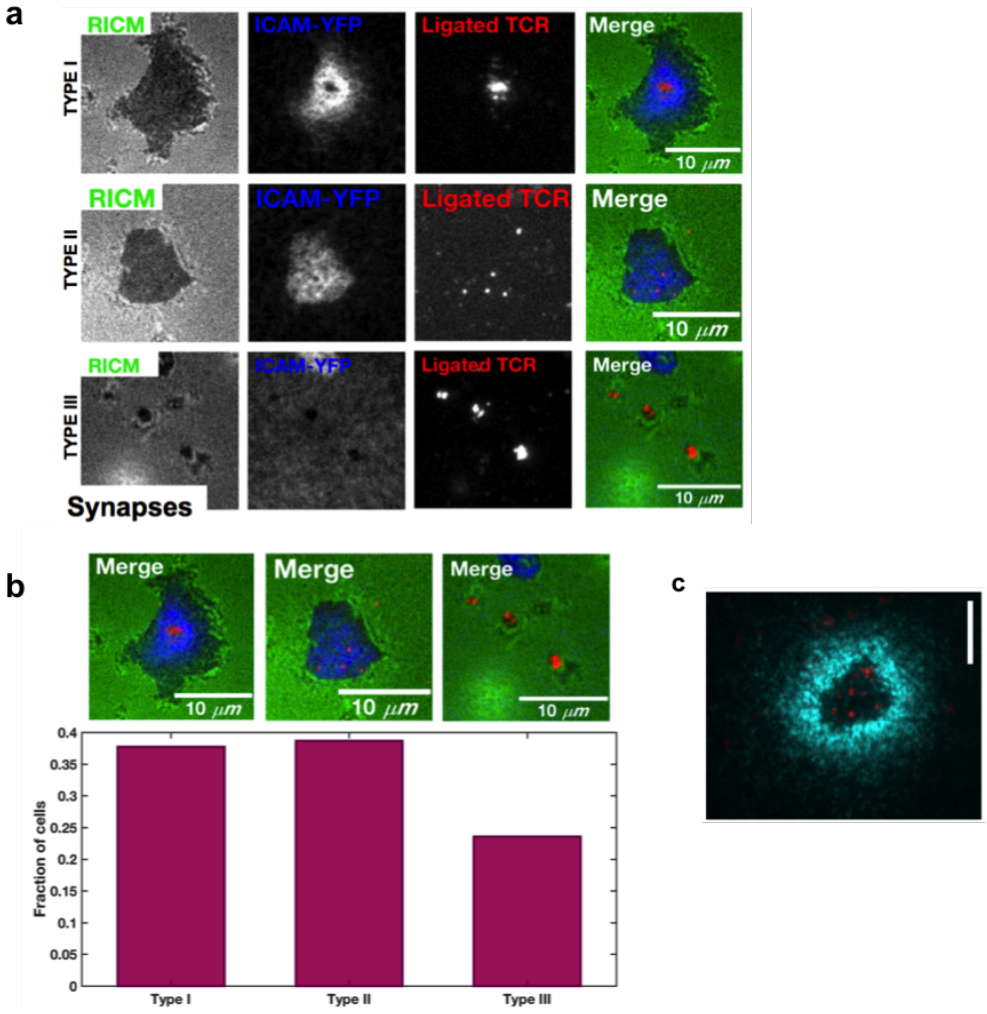

Figure 2.18: Supplementary Figure 13. Synapse structure of T cells exposed to a supported membrane. a-b. Fab'-DNA synapse structures. About 40% of cells had a typical psmac/csmac synapse structure, with Fab'-DNA (red) at the center of the bulls eye and ICAM-1 (yellow) in the periphery (Type I). Another 40% had single molecule binding events and ICAM-1 dispersed throughout the synapse (Type II). These cells likely will form a psmac/csmac at a later time point. Both Type I and Type II synapses are typical of pMHC ligand (shown in c). About 20% of cells were pinned to the bilayer with Fab'-DNA, with ICAM-1 excluded where the cell contacted the bilayer (Type III). The Type III signature is unique to Fab'-DNA and is likely a result of its strong binding affinity. Densities of Fab'-DNA and ICAM-1 were 0.09 μm^{-2} and 100's μm^{-2}, respectively. **c.** Example of synapse with pMHC ligand. MCC-MHC-Atto647N (red) and ICAM-1-YFP (cyan) segregated to form the typical psmac/csmac structure. Densities of MCC pMHC and ICAM-1 were 30 μm^{-2} and 100's of μm^{-2}, respectively, with fluorescently labeled pMHC doped in 1:100 labeled:dark. Scale bar 5 μm. Images were acquired 5-15 min after cells were added to bilayers.

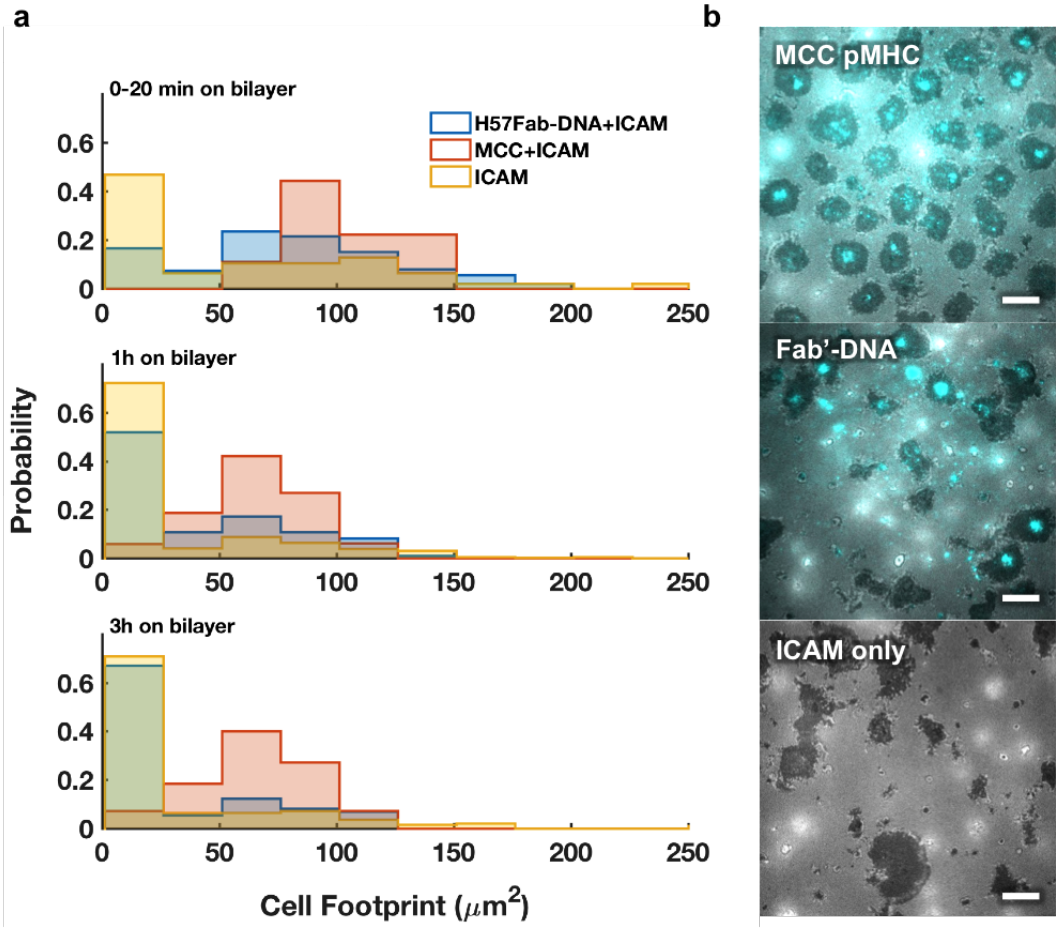

Figure 2.19: Supplementary Figure 14. Adhesion signatures of T cells on bilayers through time. a. T cell footprint areas of cells on bilayers with Fab'-DNA and ICAM-1, MCC pMHC and ICAM-1, and ICAM-1 only bilayers soon after cells had landed (top), after 1 hour (middle) and after 3 hours (bottom), as determined by RICM. Cells on Fab'-DNA bilayers initially landed and spread similarly to cells on MCC pMHC bilayers, but at later time points many cells had significantly decreased contact area, similar to cells on ICAM-1 only bilayers. **b.** Example snapshots of cells 1 hr after being added to bilayers, RICM (gray) and ligand (cyan). (Top) Cells on MCC pMHC spread isotropically and remained strongly adhered. Synapse structure was visible in most cells. (Middle) Cells on Fab'-DNA bilayers formed stable synapses. Some cells were well spread while others had minimal contact. Some cells with minimal contact were bound to many Fab'-DNA molecules (bright cyan spots outside of visible RICM footprints). (Bottom) Some cells on ICAM only bilayers were well spread while others had minimal contact area. Scale bar 10 μm.

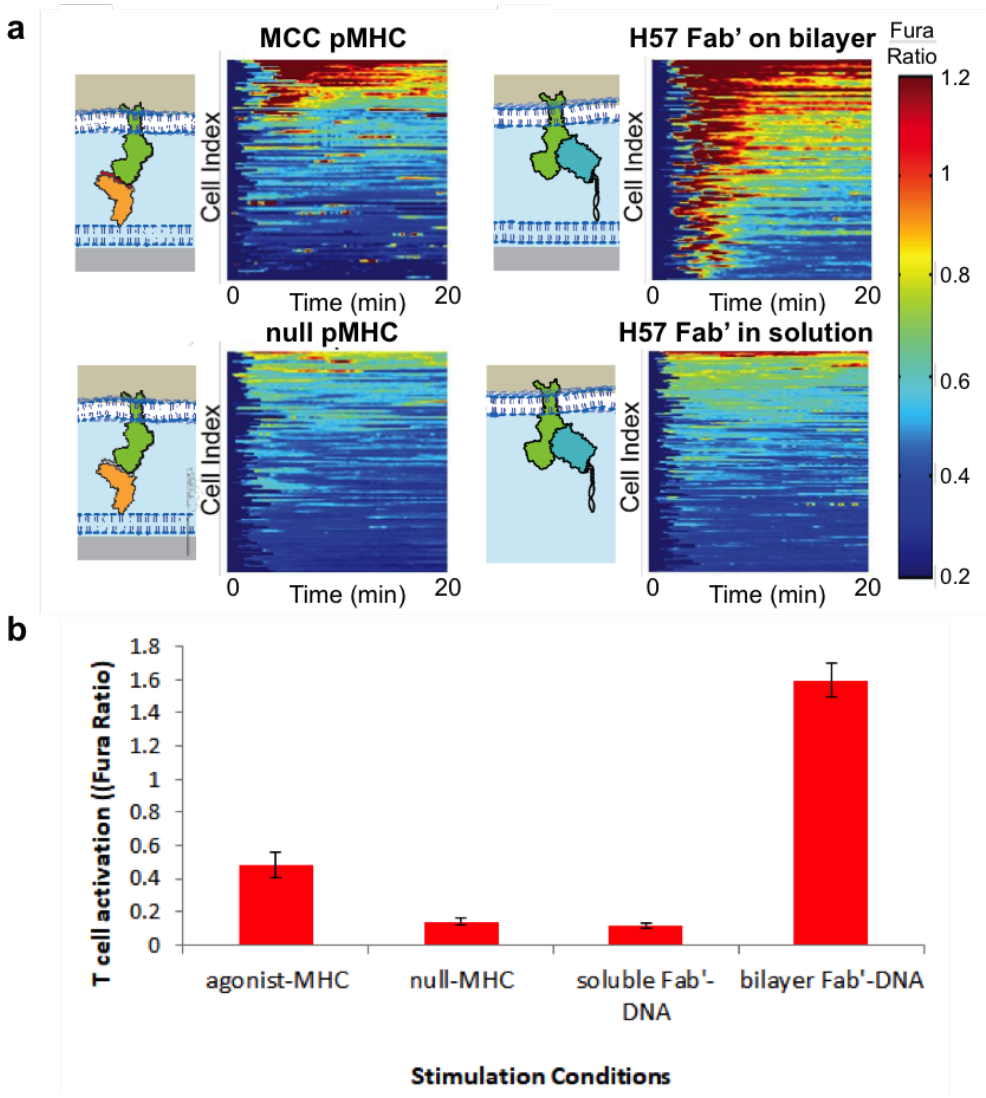

Figure 2.20: Supplementary Figure 15. Tethering H57 Fab' to a supported membrane leads to T cell activation. Populations of AND TCR transgenic primary murine $CD4^+$ T cells were stimulated with MCC pMHC, T102E pMHC, membrane-tethered H57 Fab', and soluble H57 Fab'. T cell triggering was observed using ratiometric fluorescent dyes that are sensitive to cytosolic Ca^{2+} concentrations. **a.** Heat maps indicate that membrane-tethered, but not soluble, H57 Fab' triggered Ca^{2+} in primary T cells. All experiments used ligands at densities of 100's μm^{-2}. **b.** Average peak Fura-2 ratio across stimulation conditions. Error bars denote standard deviation.

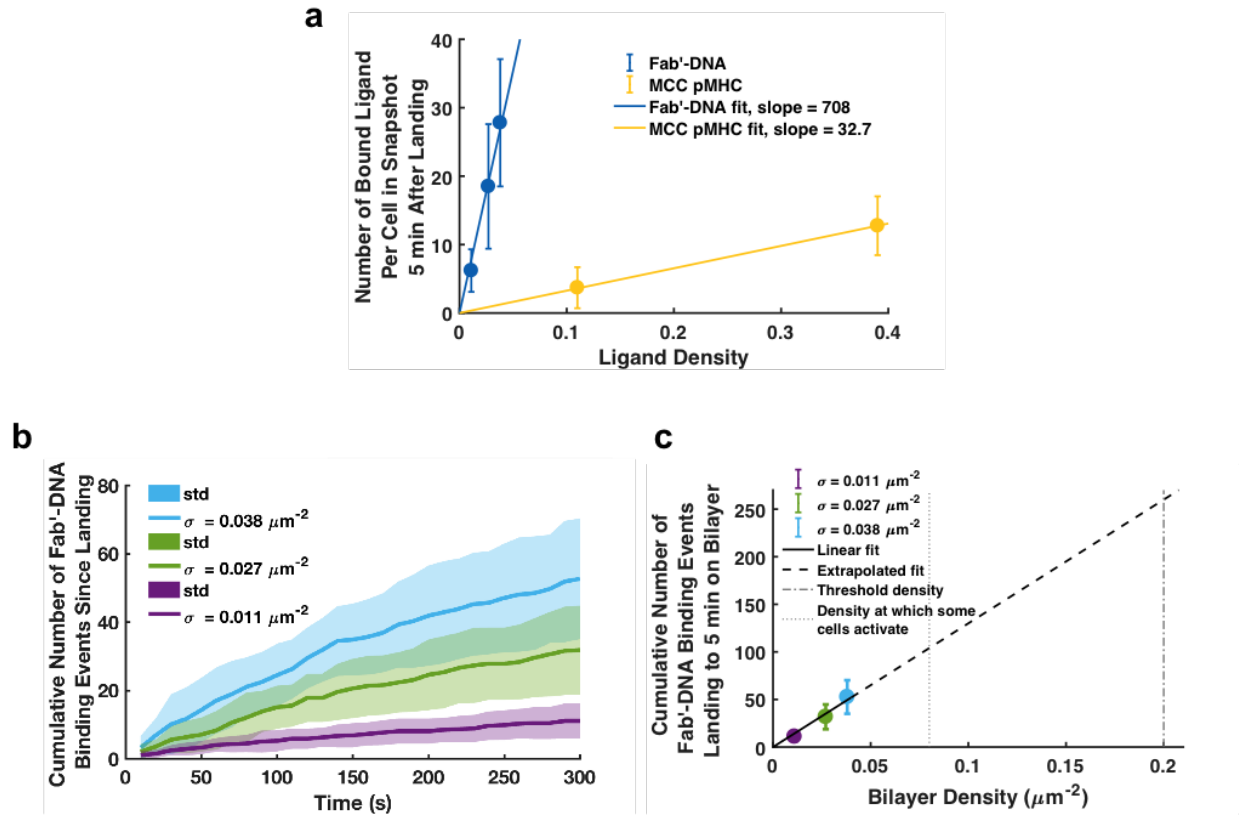

Figure 2.21: Supplementary Figure 16: Quantifying the number of binding events under cells with Fab'-DNA and MCC pMHC ligands. a. In a snapshot 5 minutes after catching a cell land on the supported membrane, cells on Fab'-DNA bilayers have far more binding events under their footprint compared to cells on MCC pMHC bilayers. Error bars denote the standard deviation of 5 cells for Fab'-DNA and 4 cells for MCC pMHC. **b.** Cumulative number of Fab'-DNA:TCR binding events accumulated by T cells since landing on the bilayer at low Fab'-DNA densities. At Fab'-DNA densities greater than 0.04 μm^{-2}, binding events are often too dense to be quantified reliably. Also, as binding events are shuttled to the immunological synapse, they become indistinguishable from each other. This limits the length of time for which cumulative binding events can be counted to under 5 min. Cell landing defines time = 0. Solid line denotes the mean of 5 cells. Shaded region denote the standard deviation. **c.** Cumulative number of Fab'-DNA:TCR binding events measured after 5 minutes as measured in (b) as a function of bilayer density. The relationship is extrapolated, assuming a linear relationship between cumulative binding and bilayer density, to densities at which cells activate, as measured by NFAT translocation. Cells are estimated to accumulate 260 $\pm$ 100 binding events after 5 minutes at the NFAT threshold density of 0.2 μm^{-2} and 110 $\pm$ 50 binding events at a density at which some cells activate, 0.8 μm^{-2}. Activating cells translocate NFAT 3 – 7 minutes after landing on the supported membrane, justifying the use of 5 minutes as a benchmark. Error bars denote the standard deviation of 5 cells.

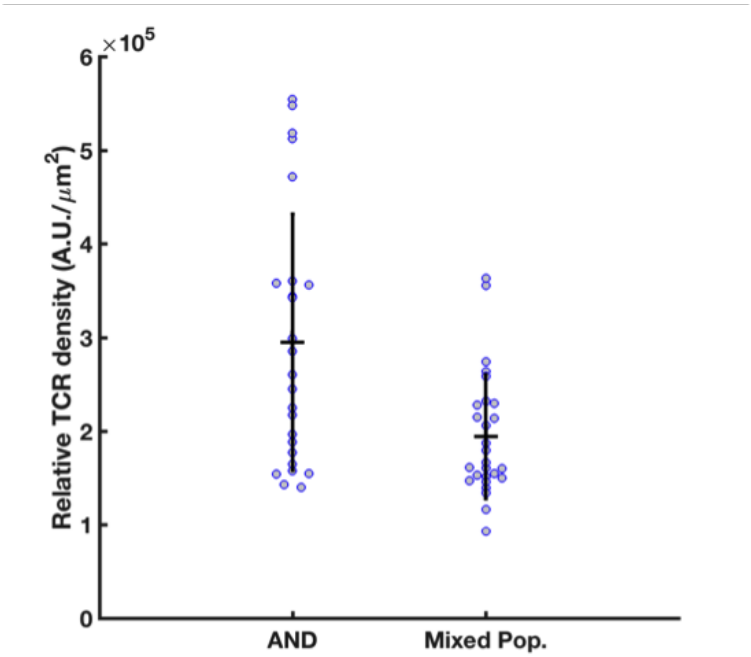

Figure 2.22: Supplementary Figure 17. TCR surface density on cells differentiated with MCC-MHC and expanded with anti-CD3/anti-CD28 antibodies. TCRs were labeled with H57 Fab'-Atto488, incubated with 100,000 T cells at 1 μg/mL in 100 μL imaging buffer for 20 min on ice. TCR surface density was similar for the two populations of cells. n = 24 (AND), 27 (Mixed Pop.) cells, error bars represent standard deviation.

Table 2.1: Peptide densities in antigen presenting cells and supported membranes

Reference	Peptide	Cell Type	peptide copies/cell	pMHC density (μm^{-2})
Bozzacco*	H2, alpha chain	Dendritic Cell	118,000	
	H2, alpha chain	B Cell	118,000	
	ApoE	Dendritic Cell	42	
	ApoE	B Cell	299	
	Cap1	Dendritic Cell	26	
	Cap1	B Cell	133	
	Latm4B	Dendritic Cell	36	
	Latm4B	B Cell	273	
	Slamf7	Dendritic Cell	36	
	Slamf7	B Cell	13	
	Tln1	Dendritic Cell	614	
	Tln1	B Cell	680	
Purcell*	H2kb-SIINFELKL		700	
	rVACV infected cells		3000	
	CMV pp65		1000-1600	
	HLA-A2/allopeptide		85-125	
	HLA-A2/LMP1		500	
	HLA-A2/LMP2A		700	
	HLA-A2/EBNA1		2000	
	H-2K^d-IGRP		25	
	H-2K^d-Insulin		1-2	
	H-2K^d-B8		5000	
	H-2K^d-A47		3000	
	H-2K^d-L2		50	
	H-2K^d-C4		4	
Grakoui**			188-25120	0.6-80
Mossman**			78500	250
Campi**			12560	40
Varma**			62.8-3140	0.2-10

*Number of peptides per cell were recorded using mass spectrometry or flow cytometry.
** Peptide densities in supported membrane experiments were converted to number peptides per cell assuming a spherical cell with a 10 μm diameter.

Table 2.2: IL-2 secretion per million cells

Sample	Experiment 1		Experiment 2		Experiment 3	
	IL-2 (pg/mL)	$\sigma(\mu m^{-2})$	IL-2 (pg/mL)	$\sigma(\mu m^{-2})$	IL-2 (pg/mL)	$\sigma(\mu m^{-2})$
ICAM only	0.57 ±0.2	–	2.2 ±0.4	–	1.0 ±0.1	–
ICAM, MCC	348 ±6	high (dark)	8 ±1	0.35	4.2 ±0.1	2.4
ICAM, H57 Fab'-DNA	42.3 ±0.6		48 ±2	0.4	6.7 ±0.1	4.0
ICAM, H57 Fab'-DNA	–	–	–	–	97 ±1	20
H57 Ab on glass	5200 ±200	saturated	2.2 ±0.4	saturated	700 ±10	saturated

Chapter 3

Height, Not Epitope, Affects Fab'-DNA Potency

3.1 Abstract

Under physiological conditions, peptide-MHC (pMHC) molecules can trigger T-cell receptors (TCRs) as monovalent ligands that are sparsely distributed on the plasma membrane of an antigen-presenting cell. TCRs can also be triggered by artificial clustering, such as with pMHC tetramers or antibodies; however, these strategies circumvent many of the natural ligand discrimination mechanisms of the T cell and can elicit non-physiological signaling activity. We have recently introduced a synthetic TCR agonist composed of an anti-TCRβ Fab' antibody fragment covalently bound to a DNA oligonucleotide, which serves as a membrane anchor. This Fab'-DNA ligand efficiently triggers TCR as a monomer when membrane-associated and exhibits a potency and activation profile resembling agonist pMHC. In this report, we explore the geometric requirements for efficient TCR triggering and cellular activation by Fab'-DNA ligands. We find that T cells are insensitive to the ligand binding epitope on the TCR complex, but that length of the DNA tether is important. Increasing the intermembrane distance spanned by Fab'-DNA:TCR complexes decreases TCR triggering efficiency and T cell activation potency, consistent with the kinetic-segregation model of TCR triggering. These results establish design parameters for constructing synthetic TCR agonists that are able to activate polyclonal T cell populations, such as T cells from a human patient, in a similar manner as the native pMHC ligand.

3.2 Statement of Significance

We report geometric requirements for potent T cell activation by synthetic TCR ligands that mimic biophysical properties of the native pMHC ligand, but have the additional ability to activate polyclonal T cell populations. We find that increasing the space between apposed membranes at TCR binding events decreases ligand potency, but that changing the ligand's binding epitope on the TCR has essentially no effect. The observed decrease in potency with increased ligand height is attributed to the longer ligands' attenuated ability to trigger TCR at binding events.

3.3 Introduction

T cells play a central role in adaptive immunity by recognizing foreign peptide fragments presented in major histocompatibility complex molecules (pMHC) with their T-cell receptors (TCR). In order to identify a wide range of potentially pathogenic peptides, each individual develops a polyclonal repertoire of T cells with distinct TCR genes. In developing thymocytes, the region of the TCR gene that encodes the pMHC recognition site undergoes somatic recombination, which creates a large sample space of potential receptors, and cells with TCR clonotypes that successfully pass a screening process survive [1]. The resulting diversity of TCRs within an individual is critical for successfully conferring adaptive immunity, but presents challenges to the study of T cell activation because the cognate pMHC that activates a given T cell is generally not known.

Antibodies that bind the TCR and associated CD3 complex (TCR/CD3) readily activate T cells, as measured by cytokine secretion, proliferation, and changes in surface receptor expression [29, 30, 54, 56, 57], but this method of stimulation differs from physiological antigen activation. Anti-TCR/CD3 antibodies, as well as widely used pMHC tetramers [3], induce crosslinking of TCR on the T cell surface. This crosslinking is an essential aspect of their activation mechanism; neither pMHC monomer nor monovalent Fab' antibody fragments are active from solution [3, 55, 60, 79], and anti-TCR/CD3 antibodies in solution must typically be further crosslinked by secondary antibodies for full activity [31]. By contrast, a growing body of evidence indicates that membrane-associated pMHC molecules are highly active as monomers [4–6, 47]. At physiological densities of agonist pMHC (0.1-2 μm^{-2}) [13–15], only tens of individual pMHC:TCR ligation events, which are widely spaced within the cell-cell interface, are sufficient to activate T cells [8, 9]. At higher agonist pMHC densities (10-250 μm^{-2}), pMHC:TCR complexes form microclusters [10, 11] that further reorganize into the large scale pattern of the immunological synapse [61, 62], but these larger scale organizations at high antigen density are not required for T cell activation [4–6, 9, 47].

We have recently developed a class of synthetic TCR agonists composed of an anti-TCR/CD3 Fab' fragment covalently bound to a DNA oligonucleotide that can uniformly activate polyclonal T cell populations as membrane-associated monomers [102]. Like natively monomeric

pMHC, Fab'-DNA molecules are inactive from solution at any concentration, but are highly potent when conjugated to a supported lipid bilayer (SLB) via DNA hybridization. Previous work focused on the anti-TCRβ H57-597 Fab'-DNA (H57 Fab'-DNA) and found it to exhibit a similar potency as a strong pMHC agonist [9]. Mechanistic studies of TCR triggering suggest that the Fab' binding epitope on the TCR/CD3 complex [20, 103] and/or the intermembrane spacing established at TCR binding events may impact ligand potency [16–18, 104, 105].

Here we examine a panel of Fab'-DNA constructs that bind three distinct epitopes on the TCR/CD3 complex and have DNA tethers of various lengths (Fig. 3.1). We synthesized Fab'-DNA ligands derived from the anti-CD3ϵ 145-2C11 antibody (2C11 Fab'-DNA) and the anti-CD3ϵ/γ 17A2 antibody (17A2 Fab'-DNA), in addition to the previously reported anti-TCRβ H57 Fab'-DNA [20, 29, 30, 56, 77] (Fig. 3.1B). Both 2C11 and H57 bivalent antibodies are commonly used to activate T cells and bind at or near the reportedly mechanosensitive FG loop of TCRβ [20, 77, 78, 103, 106]. The 17A2 antibody is less frequently used to activate T cells and has been reported to be less potent due to its binding geometry to the TCR/CD3 complex [20, 103]. DNA tethers ranging from 16 to 76 nucleotides were designed for all Fabs, creating 14 to 50 nm space between apposed membranes at binding events (Fig. 3.1C). This range of sizes spans from the native pMHC:TCR intermembrane spacing of about 14 nm [25, 107, 108] to beyond the spacing of about 30 nm established by intracellular adhesion molecule 1 (ICAM-1) bound to lymphocyte function-associated antigen 1 (LFA-1) [109] and the large 21-40 nm extracellular domain of CD45 [105, 110, 111], which has long been thought to be sterically excluded by the short pMHC:TCR complex size at T cell – antigen presenting cell junctions [11, 16, 17, 104].

We find that the intermembrane space established by DNA tether length dramatically affects Fab'-DNA potency, with larger spacing leading to less potent cellular activation, but that varying the Fab' binding epitope has essentially no effect. T cell activation was monitored by imaging translocation of a fluorescent reporter for the nuclear factor for the activation of T cells (NFAT) from the cytosol to the nucleus, which provides a binary readout of successful activation of the calcium signaling pathway in T cells [8, 9, 82, 102]. TCR-proximal signaling, measured by localized formation of protein condensates of linker for the activation of T cells (LAT), was also attenuated for longer ligands but unaffected by binding epitope. LAT is an intrinsically disordered protein that serves a signaling scaffold immediately downstream of TCR triggering [112, 113], and its condensate formation proximal to individual Fab'-DNA:TCR complexes is an indicator of local signaling activity [27, 114]. The observed dependence of T cell signaling on Fab'-DNA height is consistent with the kinetic-segregation model of TCR triggering, which implicates steric exclusion of bulky phosphatases from closely apposed membrane regions at pMHC:TCR binding events as a driving force for signal propagation from the TCR [16–18, 104, 105]. These results are also consistent with studies of similarly-structured bispecific T cell engagers (BiTEs) that show BiTEs are more effective if they bind epitopes that create smaller intermembrane spaces where they bridge TCRs on

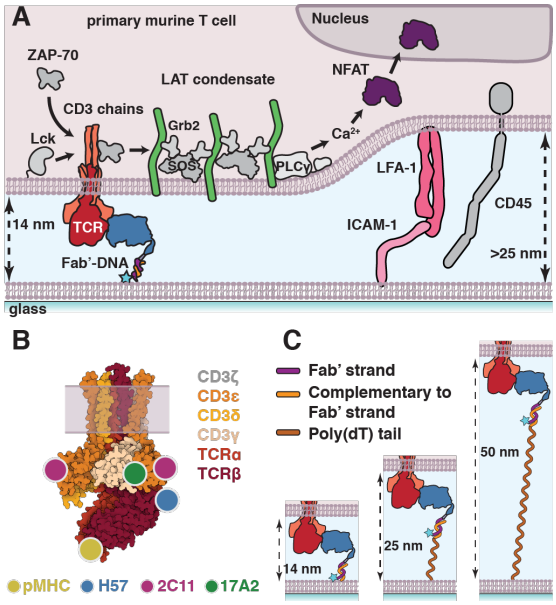

Figure 3.1: Fab'-DNA is a modular TCR ligand. (A) Fab'-DNA and ICAM-1 are presented on supported lipid bilayers. Upon adding T cells to the bilayer, LFA-1 adheres to ICAM-1 to create a stable intermembrane junction between the SLB and T cell. Within this junction, Fab'-DNA binds TCR, creating a narrow 14 nm space between membranes that excludes ICAM-1:LFA-1 conjugates and the phosphatase CD45 from close proximity. Productive TCR triggering is monitored by the formation of TCR-proximal LAT condensates and cellular activation is monitored by translocation of the transcription factor NFAT from the cytosol to the nucleus. **(B)** Fab'-DNA constructs are synthesized from antibodies that bind three distinct epitopes on the TCR/CD3 complex (adapted from PDB entry 6JXR). Binding epitopes for pMHC and all Fabs have previously been determined by crystal and NMR structures and are approximately mapped onto the TCR/CD3 cryoEM structure. **(C)** The spacing between the SLB and T cell at Fab'-DNA:TCR binding events is modulated by varying the length of the DNA tether. A poly(dT) tail is added to the membrane-proximal 5' end of the thiol-DNA, increasing the allowed distance between the membrane and the region of the thiol-DNA to which Fab'-DNA anneals.

a T cell to melanoma markers on an opposing cell [42, 43]. The T cells' indifferent response to ligand binding epitope suggests that any intramolecular aspects of the TCR triggering mechanism [103, 106, 115] do not strongly depend on TCR engagement geometry in the context of adhesion molecules and a cell-cell interface.

3.4 Materials and Methods

Fab'-DNA synthesis

All antibodies were digested with pepsin or Glu-C endoproteinase to retain the cysteines in the hinge region and then partially reduced with 2-mercaptoethylamine to form Fab' fragments. Maleimide-functionalized, dye-labeled DNA oligonucleotides were then conjugated to the reduced cysteine residue on the Fab' to form crude Fab'-DNA. This product was purified by size exclusion and anion exchange chromatography to obtain monomeric Fab' conjugated to a single DNA oligonucleotide that was labeled with a single fluorophore (25).

Supported Lipid Bilayer Preparation

Low-defect, fluid supported lipid bilayers (SLB) were prepared from a solution of small unilamellar vesicles (SUVs). SUVs were first prepared by mixing 95% DOPC (1,2-dioleoyl-sn-glycero-3-phosphocholine), 3% MCC-DOPE (1,2-dioleoyl-sn-glycero-3-phosphoethanolamine-N-[4-(p-maleimidomethyl)cyclohexane-carboxamide] sodium salt), and 2% Ni-NTA-DOGS (1,2-dioleoyl-sn-glycero-3-[(N-(5-amino-1-carboxypentyl) iminodiacetic acid) succinyl] nickel salt) phospholipids in chloroform in a piranha-etched round bottom flask. Lipids were dried and resuspended in Milli-Q water to 0.5 mg/mL total lipid concentration and sonicated to form SUVs with a probe sonicator. The SUVs were then centrifuged to remove titanium particles and lipid aggregates and mixed 1:1 with 1x PBS, resulting in a spreading solution with a final concentration of 0.25 mg/mL total lipid content. Supported membranes were formed by vesicle fusion of SUVs by adding this spreading solution to imaging chambers assembled with freshly piranha-etched glass coverslips. Thiol-DNA, complementary to the Fab'-DNA strand, was deprotected with 10 mM TCEP for 90 min to expose free thiol and then incubated on the bilayer at about 1 μM in PBS to obtain a density of approximately hundreds of molecules/μm^2 on the SLB [37]. These bilayers were stable overnight at 4 °C. Before experiments, the SLB was charged with 30 mM $NiCl_2$ to ensure stable chelation of polyhistidine-tagged ICAM-1 to the NTA-DOGS lipids. Proteins to be coupled to the bilayer were prepared in imaging buffer, added to the imaging chamber, and incubated for 35 min. Fab'-DNA incubation concentrations ranged from 50 pM for single molecule studies to 10 nM for high density samples. ICAM-1 was incubated at a concentration of 100 nM.

T cell harvesting and culture

$CD4^+$ T cells expressing the AND TCR [116] were harvested, cultured, and transduced as previously described [47, 83]. Briefly, T cells were harvested from hemizygous transgenic mice from the cross of (B10.Cg-Tg(TcrAND)53Hed/J) x (B10.BR-H2k2 H2- T18a/SgSnJ) strains (The Jackson Laboratory, Bar Harbor, ME) and activated by moth cytochrome c peptide (MCC88-103) immediately after harvest. IL-2 was added the following day within 24 h of the harvest. Cells prepared for live cell assays were retrovirally transduced with NFAT-mCherry, LAT-eGFP, or a LAT-eGFP-P2A-NFAT-mCherry plasmid-containing supernatant collected from Platinum-Eco cells (Cell Biolabs, San Diego, CA). T cells were imaged on days 5-8. Cell health was verified each day that data were collected by assessing cell morphology and signaling in response to bilayers with no agonist ligand and high density of pMHC. All animal work was approved by Lawrence Berkeley National Laboratory Animal Welfare and Research Committee under the approved protocols 177002 and 177003.

Microscopy

Imaging experiments were performed on an inverted Nikon Eclipse Ti-E motorized inverted microscope (Nikon, Tokyo, Japan) with total internal reflection fluorescence (TIRF) microscopy, reflection interference contrast microscopy (RICM), epifluorescence capabilities, and laser lines at 405, 488, 532, and 640 nm. Freely diffusing, single Fab'-DNA-Atto647 molecules were imaged in TIRF using 20 ms exposure time, 8.6 mW power at sample, and 1000 gain. Single binding events between Fab'-DNA and TCR were imaged using 500 ms exposure time, 0.4 mW power at sample, and 1000 gain. RICM and epifluorescence images were acquired with moderate exposure time (100 ms) with gain depending on the intensity of the signal. LAT was imaged using low power (0.4-0.8 mW at sample), moderate exposure time (50-200 ms) and 500 gain, with exact parameters depending on the expression of LAT-eGFP. Micro-Manager was used to automate acquisitions and collect data [84].

Image analysis

Single particle images of freely diffusing Fab'-DNA (Fig. 3.2) and Fab'-DNA bound to TCR (Fig. 3.3) were localized and tracked in the ImageJ plugin TrackMate [85](54). Particles were identified using the difference of Gaussians detector, particle diameter and threshold were determined by eye, and all data from a given experiment were analyzed uniformly. The diameter was usually set to about 0.4 μm. The simple linear assignment problem (LAP) tracking algorithm was used to link localized spots. Maximum particle linking distances were set depending on the time lapse between images and particle speed. Data from single particle tracking were then exported to MATLAB. Step size distributions, step photobleaching, dwell time distributions, and fraction bound were analyzed using custom MATLAB scripts, described in detail in the Supporting Materials and Methods.

NFAT and LAT images were processed in ilastik [117], a machine learning program for bio-image analysis. NFAT-mCherry images were segmented into cytosol and nucleus by training ilastik's pixel classification algorithm using color/intensity, edge, and texture features. Activated cells were defined as cells with a background-subtracted nucleus to cytosol intensity ratio greater than 1. Only cells that were well-spread on the bilayer and with clear nuclei were included in analysis. LAT-eGFP images were processed in ilastik to identify LAT condensates. Pixel probability maps corresponding to LAT condensates were generated in ilastik and then imported to ImageJ to be tracked in TrackMate. The number of LAT condensates experienced by a cell was determined by counting the number of LAT condensate tracks that persisted for at least 4 frames, with a 2 s time lapse between frames.

3.5 Results

Fab'-DNA constructs are monovalent when conjugated to supported membranes

Fab'-DNA constructs were synthesized by digesting three commercially available anti-murine TCR antibodies: H57-597; 145-2C11; and 17A2, purifying the monovalent Fab' fragments, and conjugating those fragments to DNA oligonucleotides labeled with a single Atto647N dye, as described previously (see Materials and Methods for details) (Figs. S1 and S2 in the Supporting Material) [102].

Supported lipid bilayers (95% DOPC, 3% MCC-DOPE, and 2% Ni-NTA-DOGS phospholipids) were formed in imaging chambers and functionalized with a thiol-modified DNA oligonucleotide (thiol-DNA) to which the Fab'-DNA molecules could hybridize. SLBs were first formed directly from unmodified SUVs followed by addition of the thiol-DNA, which became covalently linked to the MCC-DOPE lipids. The height of the Fab'-DNA above the bilayer was controlled by the length of this thiol-DNA strand. The shortest thiol-DNA strand was 16 nucleotides and precisely complemented the Fab' strand. Longer thiol-DNA strands, able to increase the intermembrane space at binding events [95, 118], were created by adding a 19 nt and 59 nt poly(dT) tail to the SLB-proximal 5' end (Fig 1C). Membrane-anchored poly(dT) tails are an established method for generating spacers able to extend past the 20+ nm thick glycocalyx on cell surfaces [118]. The length of the thiol-DNA strands used in this study were designed to allow for up to 14 nm, 25 nm, or 50 nm of vertical space between the SLB and the T cell plasma membrane at binding events between Fab'-DNA and TCR (Fig. S3).

The SLB was then functionalized with Fab'-DNA and the adhesion molecule ICAM-1, which binds the integrin receptor LFA-1 and is critical to forming a continuous contact between T cells and antigen presenting cells. Fab'-DNA rapidly anneals to the complementary thiol-DNA (Fig. 3.2A) and ICAM-1 couples to Ni-NTA lipids through multivalent interactions

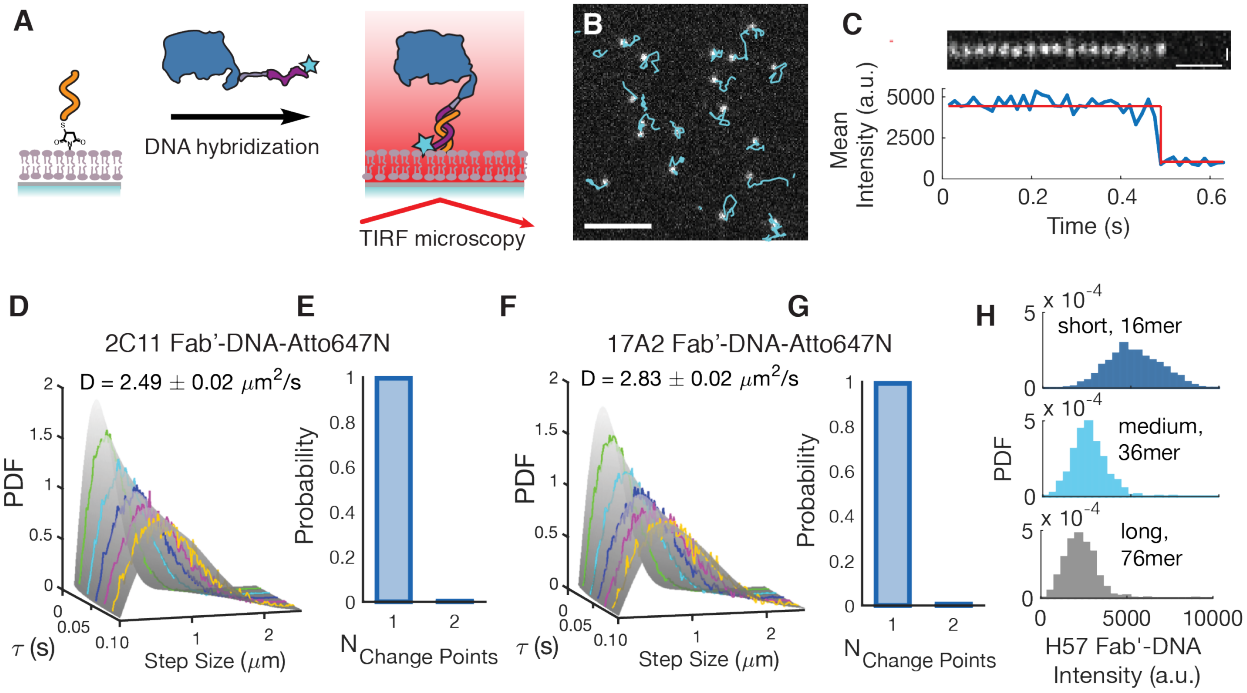

Figure 3.2: All Fab'-DNA constructs diffuse as monomers on supported lipid bilayers. **(A)** The thiol-DNA strand is covalently bound to SLBs composed of 95% DOPC, 3% MCC-DOPE, and 2% Ni-NTA-DOGS phospholipids via thiol/maleimide chemistry. Fab'-DNA that is labeled with a single Atto647N fluorophore is then incubated in the imaging chambers and anneals to the thiol-DNA strand. Fab'-DNA molecules are visualized using TIRF microscopy at 37 °C. **(B)** 2C11 Fab'-DNA molecules of uniform brightness undergo Brownian diffusion on the SLB. Scale bar 5 μm. **(C)** A diffusing 2C11 Fab'-DNA particle bleaches in a single step, confirming that it is a single Fab'-DNA molecule. Vertical scale bar 500 nm. Horizontal scale bar 0.1 s. **(D and F)** The step size distribution of 2C11 (D) and 17A2 (F) Fab'-DNA fits a single component diffusion model well. A multi-delay time protocol (τ = 29, 43, 58, 72, and 87 ms) was used to build step size distributions and all distributions were simultaneously fit to obtain the diffusion coefficient for each ligand. Error indicates the 95% CI. (n > 50,000 steps) Data are representative of three experiments. **(E and G)** >99% of 2C11 (n = 122) (E) and 17A2 (n = 175) (G) Fab'-DNA particles bleach in a single step, with intensity traces exhibiting a single change point as shown in (C). These data were obtained on gel-phase SLBs to enable tracking of particles for their full trajectories until photobleaching. The <1% of particles that undergo 2-step photobleaching match the probability that two Fab'-DNA are randomly spaced below the diffraction limit. No particles bleach in three or more steps. Panels B-G display data collected with the shortest thiol-DNA. **(H)** Single particle fluorescence intensity distributions for Fab'-DNA conjugated to the SLB by annealing to short, medium, and long thiol-DNA strands show decreased fluorescence intensity with increased tether length. Short thiol-DNA: n < 1000 particles; medium thiol-DNA: n < 500 particles; long thiol-DNA: n < 1000 particles.

between Ni^{2+} and its histidine tag [83]. Though the Atto647N dye used to label Fab'-DNA has a high membrane interaction factor [93], it has previously been confirmed that Fab'-DNA does not interact with the SLB in the absence of the complementary thiol-DNA [102].

H57, 2C11, and 17A2 Fab'-DNA constructs were confirmed to be monovalently conjugated to the SLB using single molecule total internal reflection fluorescence (TIRF) microscopy. For measurement of freely diffusing Fab'-DNA, images were taken with short exposure time (20 ms) and high power (8.6 mW). In streaming image acquisitions, particles of uniform brightness diffuse across the SLB with uniform two-dimensional Brownian motion (Fig. 3.2B) and bleach in a single step (Fig. 3.2C). The ImageJ plugin TrackMate was used to link images of single fluorophores into trajectories of diffusing particles, and the step size distribution of the resulting tracks were analyzed to obtain the diffusion coefficient of each Fab'-DNA construct. The step size distributions for both 2C11 Fab'-DNA and 17A2 Fab'-DNA, constructed using a multiple delay time protocol (see Supporting Materials and Methods), were each well-fit by a single species Brownian diffusion model (Figs. 3.2D, 3.2F, Fig. S4):

$$\rho(r, \tau, D) = \frac{r}{2D\tau} exp(\frac{-r^2}{4D\tau}) \tag{3.1}$$

with molecular displacement, r, corresponding delay time, τ, and diffusion coefficient, D. D values for 2C11 Fab'-DNA and 17A2 Fab'-DNA were measured to be $2.49 \pm 0.02\ \mu m^2/s$ and $2.83 \pm 0.02\ \mu m^2/s$, respectively, in close agreement with the previously reported value of D = $2.43 \pm 0.02\ \mu m^2/s$ for H57 Fab'-DNA on comparable supported bilayers [102]. Step photobleaching analysis further confirmed that all Fab'-DNA ligands conjugated to the SLB as monomers. For both 2C11 and 17A2 Fab'-DNA constructs >99% of fluorescent signals bleached in a single step (Figs. 2E, 2G). The diffusion and step photobleaching data together provide strong evidence that Fab'-DNA exists on the supported membrane as a monovalent, monomeric ligand.

Single particle fluorescence intensity distributions of Fab'-DNA-Atto647N annealed to short (16 nt), medium (36 nt), and long (76 nt) thiol-DNA tethers confirm that the longer tethers create more space between Fab'-DNA and the SLB. In TIRF, illumination intensity decays exponentially from the interface (in this case, between glass and the water layer below the bilayer), and so particle intensity can be a ruler for height for fluorophores if they are in a uniform chemical environment. In this system, the Atto647N dye on Fab'-DNA annealed to the shortest thiol-DNA tether likely intercalates into the membrane, which increases the brightness of the fluorophore and slows diffusion [102]. The intensity distributions of Fab'-DNA-Atto647N annealed to the longer tethers are substantially dimmer, indicating that the Atto647N fluorophore is not able to intercalate into the SLB and that it is at an increased height above the SLB where it experiences a lower illumination intensity (Fig. 3.2H). As expected, particle intensity decreases as tether length increases. These data agree with the model of the poly(dT) linker as a worm-like chain with a persistence length of 1.5 – 3 nm in

150 mM salt and a fluorophore that can occupy a range of heights above the SLB [119], with the average particle height increasing with linker length. The medium and long thiol-DNA tethers are almost certainly not fully extended when diffusing freely on the bilayer, but they have the capability to extend up to 25 nm and 50 nm, respectively, in response to forces from the apposing T cell membrane.

All Fab' ligands bind TCR with high affinity

We then evaluated the interaction between T cells and SLB-tethered agonists by live-cell imaging of primary murine $CD4^+$ effector T cells expressing the AND TCR (details in Materials and Methods). T cells were added to imaging chambers containing a continuous SLB decorated with Fab'-DNA and ICAM-1 as described above that was equilibrated on the microscope to 37 °C. T cells made initial contact with the bilayer through interactions of adhesion receptor LFA-1 with ICAM-1, and then spread on the bilayer, creating a junction within which Fab'-DNA molecules could bind TCR (Fig. 3.3A). This junction was visualized using reflection interference contrast microscopy (RICM). When Fab'-DNA binds TCR, its mobility dramatically decreases (Fig. 3.3B), as has been reported previously with other TCR ligands [8, 47, 95]. Bound ligands are specifically resolved using a long, 500 ms exposure time, which allows slow-moving bound Fab'-DNA to be clearly resolved while the fluorescent signal from quickly diffusing unbound Fab'-DNA is blurred (Fig. 3.3B) [47]. Bound Fab'-DNA was tracked through time, with 10 s time lapse between images to minimize photobleaching, enabling direct visualization of individual Fab'-DNA:TCR dwell times (Figs. 3.3A, 3.3C), and dwell time distributions for each ligand were assembled from those tracks (Fig. 3.3D). These distributions were fit with a single exponential decay, based on the first order dissociation kinetics of unbinding. After correcting for photobleaching, all Fab' ligands exhibited a dwell time, τ_{off}, of at least two minutes. In our experiments, Fab' ligands become difficult to track accurately after about two minutes due to the shuttling of bound TCR to the geometric center of the cell (Fig. 3.3A), and so these measured dwell times reflect a lower bound. Fab fragments are known to bind strongly to their binding partner, with the H57 Fab fragment reported to bind TCR stably for > 50 min [80]. In contrast, the strong agonist MCC-MHC binds AND TCR with a reliably measured dwell time of about 50 s using this method [8, 9, 47, 102].

The Fab'-DNA ligands in this study also bind TCR with a fast on-rate, corresponding to an overall very high efficiency of binding. The total number of Fab'-DNA ligands underneath a cell and the number of TCR-bound Fab'-DNA ligands can be independently measured to determine the fraction of bound Fab'-ligands at any point in time. All Fab' ligands can be resolved by rapidly acquiring short (50 ms) exposure images while bound Fab'-DNA:TCR complexes can be distinguished using long (500 ms) exposure images, in which the free ligands are diffusing too rapidly to produced well-defined images (Fig. 3.3E) [8, 102]. The cell footprint on the bilayer is determined by RICM, and the fraction of ligands under the cell that are bound, a measure of the efficiency of ligand:receptor binding, can then be

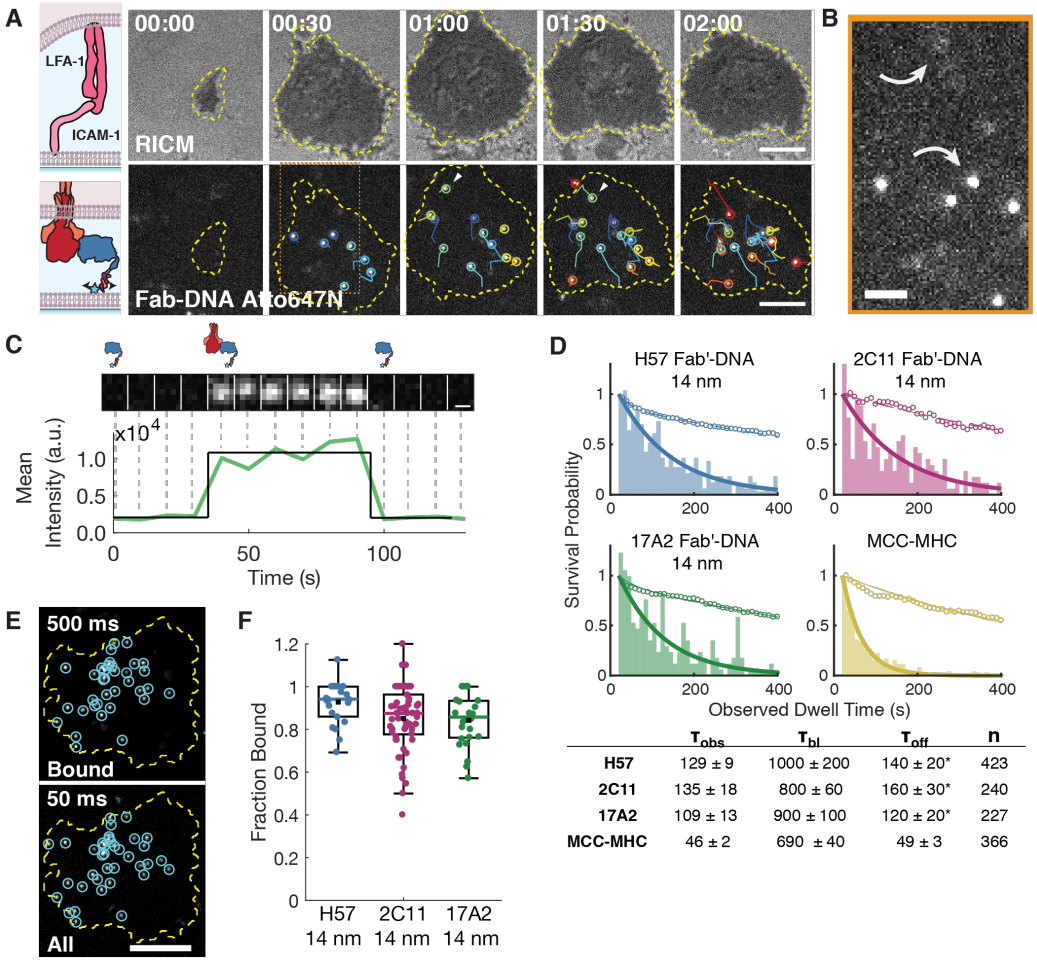

	τ_{obs}	τ_{bl}	τ_{off}	n
H57	129 ± 9	1000 ± 200	140 ± 20*	423
2C11	135 ± 18	800 ± 60	160 ± 30*	240
17A2	109 ± 13	900 ± 100	120 ± 20*	227
MCC-MHC	46 ± 2	690 ± 40	49 ± 3	366

Figure 3.3: Measurements of individual binding events between Fab'-DNA and TCR illustrate that all Fab'-DNA complexes strongly bind TCR. (A) T cells adhere to the bilayer through ICAM-1:LFA-1 interactions, and Fab'-DNA-Atto647N binds TCR within this SLB – T cell junction. Each binding event is tracked through time, denoted with a unique color for each event. Scale bar 5 μm. **(B)** A long, 500 ms exposure time at low power allows slowly-moving bound Fab'-DNA images (bottom arrow) to be resolved while quickly diffusing free Fab'-DNA forms a blurred image (top arrow). Scale bar 2 μm. **(C)** The intensity trace of a Fab'-DNA:TCR binding event through time illustrates that single binding and unbinding events are readily visualized. Scale bar 300 nm. **(D)** Dwell time distributions, corrected for photobleaching (empty circles), for Fab'-DNA ligands illustrate their very slow off-rates. *The reported off for Fab'-DNA ligands are underestimates due to difficulty tracking ligands as they approach the center of the SLB - T cell junction. **(E)** Bound (top) and all (bottom) ligand under a cell are imaged with long and short exposure times, respectively. Scale bar 5 μm. **(F)** The fraction of Fab'-DNA ligands bound under T cells is very high all Fab'-DNA constructs. Colored bar: median; black square: mean; box: IQR; whiskers: data within 1.5x IQR. (H57: n = 27; 2C11: n = 58; 17A2: n = 26). Data are compiled from cells from at least two mice for each condition in dwell time and fraction bound measurements.

directly calculated. The median fraction bound was above 0.85 for all Fab'-DNA constructs, indicating that they all bind AND TCR very efficiently (Fig. 3.3F). By comparison, about 30% of the strong agonist MCC-MHC, is observed bound to AND TCR at similar ligand densities [8].

We considered the possibility that Fab'-DNA constructs with longer tethers may have slower kinetic on-rates due to their increased conformational degrees of freedom and therefore could have a lower measured fraction bound. This, however, was not the case; the measured fraction bound for H57 Fab'-DNA with the medium length (36 nt) and long (76 nt) DNA tethers were almost identical to the fraction of bound H57 Fab'-DNA with the short (16 nt) tether (Fig. S5).

Fab'-DNA potency is independent of binding epitope, but varies with DNA tether length

We characterized Fab'-DNA potency by measuring T cell activation vs. ligand density dose-response curves. Nuclear localization of the transcription factor nuclear factor for the activation of T cells (NFAT) is a reliable, binary indicator of early T cell activation and has been used as a quantitative readout for the activation of the calcium signaling pathway in previous precision ligand density titrations [8, 9, 102]. An NFAT localization reporter, lacking the DNA binding domain and fluorescently tagged with mCherry, allows for facile visualization of NFAT localization without modulating transcriptional activity [82]. T cells transduced with the NFAT reporter were added to SLBs presenting ICAM-1 and Fab'-DNA or the strong pMHC agonist, MCC-MHC. Cells were visualized landing and spreading on the bilayer, binding Fab'-DNA, and within minutes, translocating NFAT from the cytosol to the nucleus (Fig. 3.4A). Cells were defined as activated if the fluorescence intensity from the NFAT reporter was greater in the nucleus than in the cytosol (ratio > 1) (Fig. 3.4B). The potency of each ligand was measured by counting the fraction of activated cells 20 min after adding cells to bilayers with precisely quantified ligand density (Fig. S6A). Regardless of ligand binding epitope, all ligands that allowed about 14 nm spacing between the SLB and T cell plasma membrane at binding events – MCC-MHC and all Fab'-DNA constructs with 16 nt DNA tether – reached a half-maximal response at a ligand density of 0.2-0.4 μm^{-2} (Fig. 3.4C). Additionally, we have previously shown that short-tethered H57 Fab'-DNA and MCC-MHC stimulate similar IL-2 responses from T cells, indicating that later functional outputs of T cell activation are independent of ligand binding site [102]. By contrast, ligand potency was strongly influenced by the length of the thiol-DNA tether. Ligands with DNA tethers that allowed up to 25 nm and 50 nm of space between the SLB and T cell plasma membrane were about 10 times and 100 times less potent, respectively, than the ligands that allowed an intermembrane space of 14 nm (Figs. 4D, S6B). Interestingly, even very high density (100 μm^{-2}) of the longer tethered ligands did not lead to maximal activation of the T cell population (Fig. S6C).

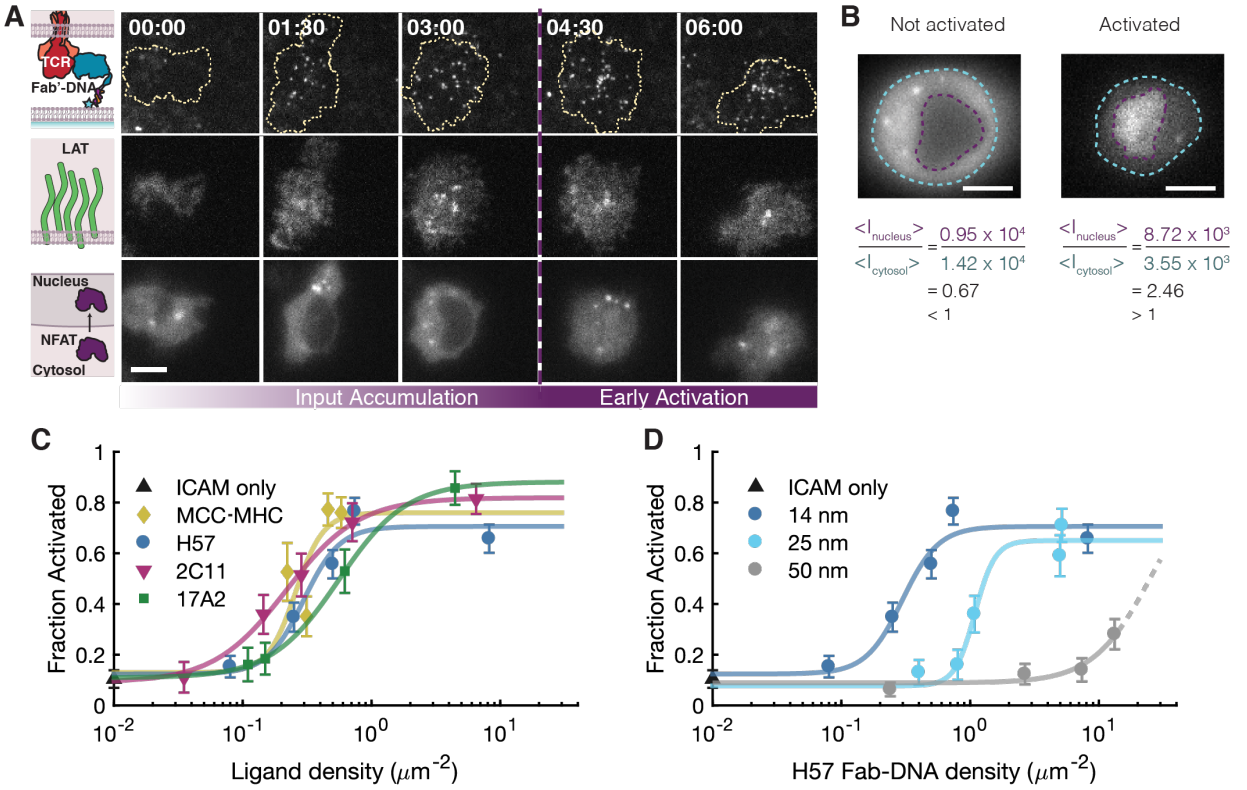

Figure 3.4: All short ligands activate T cells with similar potencies regardless of ligand binding epitope while longer ligands have lower potency. **(A)** Cells added to supported lipid bilayers make adhesion contacts, bind TCR ligand (top row), respond to TCR triggering, visualized by LAT condensate formation (middle row), and may activate, visualized by NFAT reporter fluorescence intensity accumulating in the nucleus. Scale bar 5 μm. **(B)** Cells are defined as activated if the ratio of fluorescence intensity in the nucleus to the cytosol is greater than one and not activated if the ratio is less than one. Scale bar 5 μm. **(C and D)** Dose-response curves for each ligand are built by adding cells to bilayers with precisely quantified density of ligand, letting cells interact with the bilayers for 20 min, then determining the fraction of activated cells for each condition. n $>$ 50 cells for all conditions. Error bars denote the SEM. Data are representative of at least two biological replicates. **(C)** All ligands that create close, 14 nm intermembrane spaces at binding events activate with similar potency, regardless of ligand binding epitope. **(D)** H57 Fab'-DNA potency significantly decreases as the length of the DNA tether increases. The dashed line for longest tether shows the extrapolated fit if a maximum T cell response similar to the shorter ligands is assumed.

Increased tether length decreases the efficiency of LAT activation by bound TCR

We finally imaged TCR-proximal signaling events to investigate whether the low potencies of long-tethered Fab'-DNA constructs are rooted in a poor ability to trigger TCR efficiently despite robust binding. To do this, we visualized condensation of LAT, which results from phosphorylation activity immediately downstream of triggered TCRs [112, 114]. LAT condensates have recently been shown to occur even in response to single ligation events between agonist pMHC and TCR [27], and so here, LAT condensation serves as a measure of TCR-proximal signaling activity from individual Fab'-DNA:TCR binding events. T cells expressing LAT-eGFP were introduced to fluid supported lipid bilayers decorated with ICAM-1 and either a Fab'-DNA construct or the agonist MCC-MHC. Using multichannel TIRF microscopy, binding events were imaged as described above, using a long exposure time at low power to specifically image slowly moving ligand, and LAT-eGFP was imaged using low power and moderate exposure time to best capture the dynamic range of LAT fluorescent intensity in the cell being imaged. Cells were imaged starting upon initial contact with the bilayer and continuing for 120 s, during which LAT condensation in response to binding is most active, with a 2 s time lapse between successive frames. The density of Fab'-DNA on bilayers was kept very low (0.01-0.03 μm^{-2}) in order to best track single ligation events through time and unambiguously capture the LAT condensation response to these events.

Snapshots from time sequences showed clearly resolved binding events between ligand and TCR and concurrent local increase in LAT density at these binding events for potent ligands (Fig. 3.5A, first four columns). Less potent ligands – those with longer DNA tethers that allowed for greater intermembrane space – experienced fewer LAT condensates colocalized binding events (Fig. 3.5A, last two columns). For potent ligands, a single binding event was routinely sufficient to trigger significant LAT condensation (Fig. 3.5B, circled binding event; Fig. S7A), as has been previously reported for strong pMHC agonists [27]. Moreover, T cells formed LAT condensates in response to both Fab'-DNA and MCC-MHC when both ligands were presented on the bilayer at low density, indicating that T cells do not readily distinguish ligand identity and that the effects from multiple agonists are additive (Fig. S7B). Interestingly, instances where LAT clusters formed on bilayers presenting weak ligands with long DNA tethers often colocalized with clusters of binding events (Fig. S7C).

To quantify the signaling efficiency of each ligand, the total number of binding events experienced by a cell and the total number of LAT clusters formed within the cell were counted for first two minutes of the cell interacting with the supported membrane. Binding event trajectories were counted after tracking all events in TrackMate [85]. LAT condensates were first identified in each frame using ilastik [117], a user-friendly machine learning program for bio-image analysis, and then LAT pixel probability maps produced by ilastik were tracked in TrackMate (details in Supporting Materials and Methods). The ratio of the number of LAT condensates to the number of binding events was then calculated for each cell (Fig.

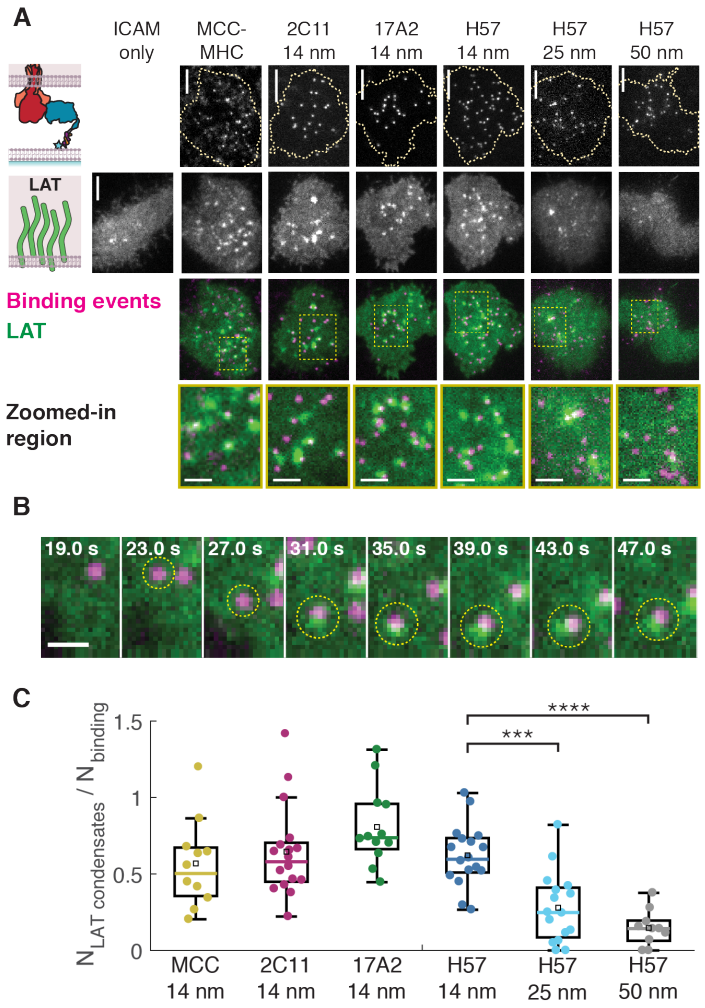

Figure 3.5: Short ligands trigger TCR with similar efficiency, while taller ligands trigger TCR with lower efficiency. (A) Snapshots of binding events underneath a T cell (top row) and LAT-eGFP (second row) show that LAT condensates often colocalize with binding events from short ligands, whereas far fewer LAT condensates form in cells on bilayers with longer ligands (third and fourth rows). Magenta: binding events; green: LAT. Scale bar for first three rows 5 μm. Scale bar for fourth row 2 μm. **(B)** A single binding event between Fab'-DNA and TCR is sufficient to create a proximal LAT condensate. Scale bar 1 μm. **(C)** The numbers of LAT condensates and binding events experienced by cells were counted for the first 2 min after initial cell contact with the bilayer. There is no significant difference in the ratio of the number of LAT clusters to the number of binding events for short ligands, but a significant decrease for ligands with longer DNA tethers. Colored bar: median; black square: mean; box: interquartile range; whiskers: data within 1.5x IQR. Significance was determined by the Mann-Whitney U-test (*** $p < 0.001$; **** $p < 0.0001$; n.s. $p > 0.01$). Data are compiled from cells from at least two mice for each condition.

3.5C). Some LAT condensates formed in the absence of binding (see ICAM only example in Fig. 3.5A), and so these ratios occasionally exceed one. In agreement with the NFAT dose-response curves, all ligands that allowed about 14 nm spacing between the SLB and T cell plasma membrane produced LAT clusters with a similar efficiency per binding events, with medians of around 0.6. The ratio of LAT clusters to binding events significantly decreased with increasing intermembrane space (Fig. 3.5C). These results indicate that the difference in ligand potency seen at the level of transcription factor localization results from differences in the ligands' abilities to trigger TCR.

3.6 Discussion

Implications for further Fab'-DNA development

Fab'-DNA shows promise as a tool to activate of polyclonal T cell populations in a manner similar to agonist pMHC; Fab'-DNA is monovalent and activates T cells at low ligand densities when membrane-associated but is inactive from solution [102]. Here, we use the modular design of Fab'-DNA to test the dependence of T cell response on Fab'-DNA binding epitope and tether length. To achieve the goal of designing a universal TCR agonist, Fabs used in Fab'-DNA constructs must bind the constant region of the TCR, which is far from the pMHC binding site at the apex of the TCR variable region (Fig. 3.1B). The robust result that signaling from the TCR is indifferent to binding site allows flexibility in Fab' choice when using anti-murine Fab'-DNA and in designing Fab'-DNA constructs capable of binding and activating human T cells or perhaps chimeric antigen receptor T cells. That signaling potency depends on the spacing between apposed membranes at binding events is consistent with previous work with pMHC and therapeutic TCR-binding molecules [25, 42, 43].

The experimental system described herein is similar to a recent study by Roffler and coworkers that found that a very high affinity (< 1 nM) anti-CD3 single chain variable fragment (scFv) did not exhibit a tether-length dependence on T cell activation [99]. However, in their study an anti-CD3 scFv with 8 nM affinity exhibited an order of magnitude decrease in potency as the intermembrane spacing at binding events increased from 10 to 40 nm, and 2C11 scFv, with a reported affinity of 70 nM, exhibited a dramatic decrease in potency as tether length increased, in close agreement with the results presented in our study. Notably, moderate-affinity antibody fragments bind TCR/CD3 considerably more strongly than pMHC, and further work developing Fab'-DNA to mimic pMHC would focus on further decreasing, not increasing, Fab' binding affinity, potentially enhancing the tether-length dependence of these ligands. The density-dependent data presented in Chen *et al.*, reporting that the T cell response is nearly identical when interacting with antigen presenting cells decorated with 10 μm^{-2} compared to 100 μm^{-2} of their shortest ligand [99], also agree with our data, which show that the threshold activation density for short ligands is around

0.2 μm^{-2}, near physiological pMHC densities, and T cell populations are fully activated by about 1 μm^{-2} ligand.

Relating results to proposed mechanisms of T-cell receptor triggering

The data presented in this study most closely relate to two proposed (and by no means mutually exclusive) mechanisms of TCR triggering: (1) kinetic-segregation and (2) anisotropic mechanosensing by the TCR. The kinetic-segregation model proposes that when TCRs are localized in close contact zones between apposed membranes for a sufficient length of time, whether by ligand binding or not, the bulky and abundant phosphatase CD45 is excluded from their proximity [16–19, 28, 104, 105]. CD45 exclusion increases the probability that TCR and proximal downstream kinases and scaffolding molecules are phosphorylated and leads to signal transduction [120]. All results presented herein are consistent with kinetic-segregation. Interpreting the data according to this model, short Fab'-DNA ligands are able to pin TCR in close contact zones that exclude CD45 for extended lengths of time, even if that zone is created by only a single binding event. Increasing the DNA tether length prevents the formation of close contact zones at binding events and increases the availability of bound TCR to CD45.

The relation of these data to the mechanosensing model is more complex. The model of the TCR as an anisotropic mechanosensor proposes that ligands able to exert a certain torque on the TCR are more effective at triggering TCR than ligands incapable of applying such torque. According to this model, force from pMHC binding is transmitted through the FG loop of TCRβ, causes allosteric change in the TCR/CD3 constant regions, and brings TCR/CD3 to a signaling-competent state [103, 121]. H57 binds the FG loop of TCRβ, and is thought to trigger TCR by directly acting on this hinge when its Fab fragment is bound to a surface [78]. 2C11 has two potential binding sites on the TCR/CD3 complex, as each complex has two CD3ϵ subunits. One CD3ϵ subunit sits directly above the FG loop, and 2C11 binding to this subunit has been proposed to act on the FG loop hinge similarly to H57 [20]. The second CD3ϵ subunit sits approximately 120° away from the first [122]. The observation that 2C11 Fab'-DNA has a similar potency as H57 Fab'-DNA and MCC-MHC suggests that 2C11 Fab'-DNA is able to trigger TCR regardless of which CD3ϵ subunit it binds. This interpretation is corroborated by 2C11 Fab'-DNA:TCR binding events producing LAT clusters with the same efficiency as H57 Fab'-DNA and MCC-MHC. Due to the relatively low densities of Fab'-DNA used in these studies (0.01 - 1 μm^{-2}), it is unlikely that two 2C11 Fab'-DNA molecules bind the same TCR.

The results from 17A2 Fab'-DNA, matching results from all ligands that bind other epitopes, further underscore that TCR/CD3 appears to be indifferent to where it is bound. 17A2 binds the CD3ϵ/CD3γ cleft, off-axis from the FG loop fulcrum [20, 122]. In experiments by Kim and coworkers, using optical tweezers and in the absence of adhesion, 17A2

antibody activated T cells only with the exertion of a tangential force. However, the experimental data we present here are from supported lipid bilayer assays with low 17A2 Fab'-DNA ligand density and in the context of physiologically dense ICAM-1:LFA-1 adhesion. In this configuration, Fab'-DNA:TCR binding always occurs within a few tens of nanometers of ICAM-1:LFA-1 adhesion complexes, and is not mechanically isolated from these [123, 124]. Mechanical coupling among protein complexes within the intermembrane junction may obviate the previously observed requirement of directional torque to trigger TCR. Notably, free lateral diffusion of ligands in the SLB prevents sustained tangential forces, and normal force applied to a single half antibody at a T cell–bead interface has been shown to be sufficient to activate T cells [70]. It does not appear that TCR/CD3 is sensitive to which region or regions of the complex bear the load of a normal force in context of ICAM-1:LFA-1 adhesion.

These experiments, however, do not rule out force as an important mediator of TCR triggering by Fab'-DNA. TCRs bound the Fab'-DNA with short DNA tethers are more likely to sustain normal forces, due to the presence of larger ICAM-1:LFA-1 binding interactions and proteins on the T cell with large extracellular domains like CD45, compared to TCRs bound by Fab'-DNA with longer tethers. It is possible that the forces on TCR bound to short ligand are greater in our experimental platform compared to a junction between an antigen presenting cell and a T cell because small adhesion proteins such as CD2 are not included in our bilayers.

Binding of a single Fab'-DNA is capable of creating significant TCR-proximal signaling

Our experiments are designed for facile, direct observation of single binding events between ligand and TCR with the ability to simultaneously image signaling response. With this design, we routinely see LAT condensates triggered by single ligand:TCR binding events with both pMHC [27] and Fab'-DNA ligands (Fig. 3.5). These data stand in apparent contrast to a recently published, and carefully executed, study by Sevcsik and coworkers that concludes that a similar monovalent H57-derived ligand, reported to allow 12-19 nm space between the SLB and T cell, activates T cells as efficiently as MCC-MHC only if two ligands are within a lateral distance of 20 nm from each other [125]. Interestingly, in our study, the weaker Fab'-DNA ligands with longer DNA tethers were measured to be more likely to generate a LAT condensate if multiple ligands are bound in a diffraction-limited area. This observation, that less potent ligands cause TCR-proximal signaling more readily when they are clustered, may relate to other studies that report ligand clustering as a requirement for signaling using similar experimental platforms [95, 125].

In conclusion, through modulating the binding epitope and DNA tether length of Fab'-DNA constructs, we find that varying the DNA tether length affects Fab'-DNA potency, but varying the binding epitope does not. These findings advance the utility of membrane-linked Fab'-DNA ligands as universal T cell agonists and clarify design criteria for further

development of this class of synthetic T cell activators.

3.7 Supplementary Materials

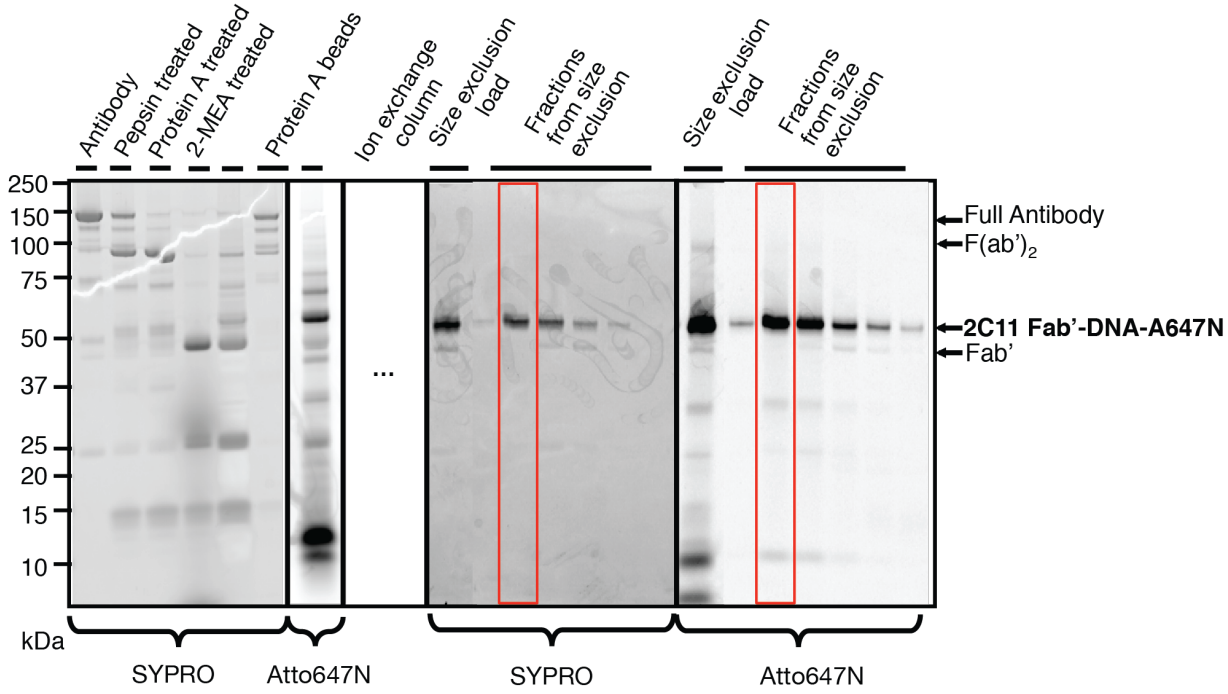

Figure 3.6: Supplementary Figure 1. 2C11 Fab'-DNA synthesis and purification. The fragmentation of 2C11 is monitored by SDS-PAGE and the purity of 2C11 Fab'-DNA-Atto647N after purification over ion exchange and size exclusion columns is confirmed.

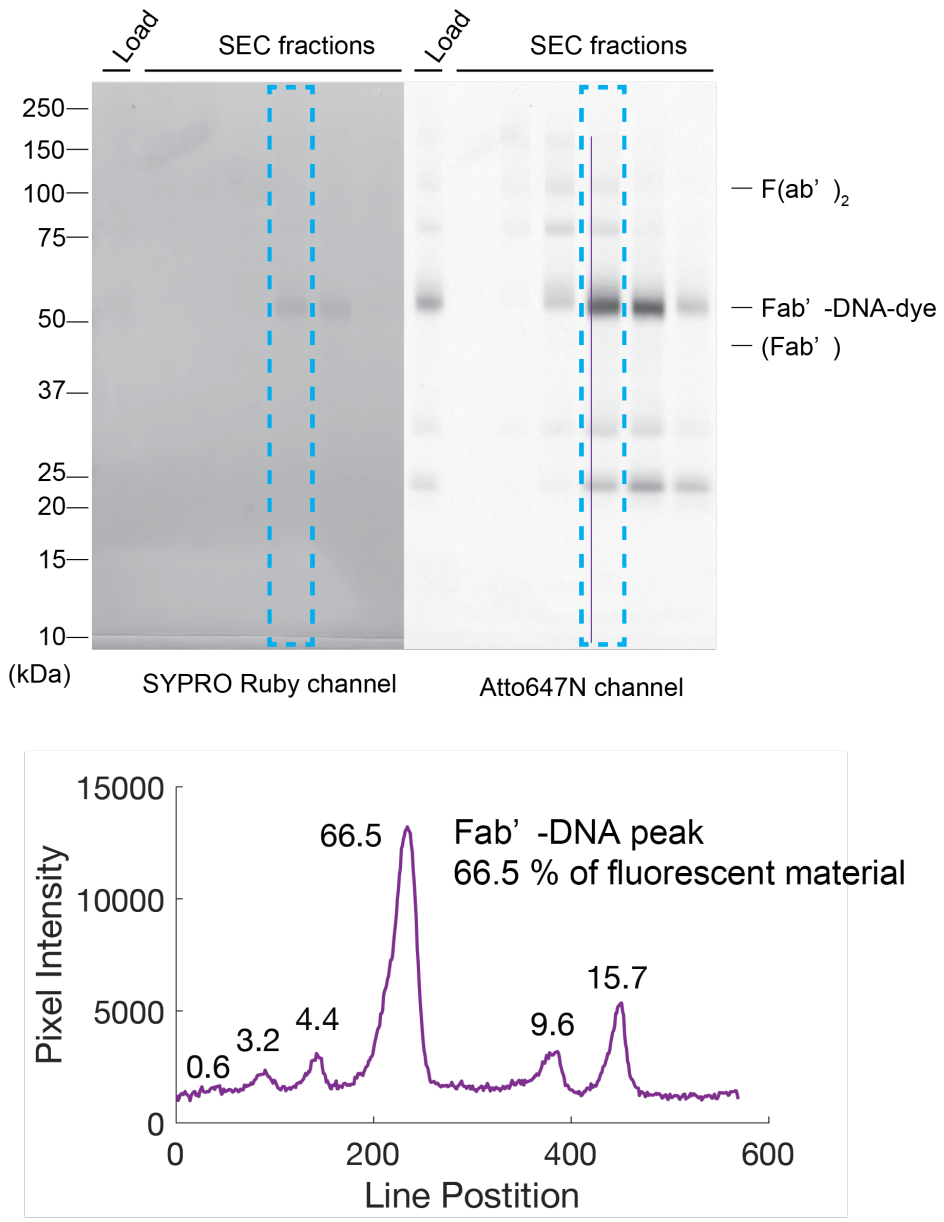

Figure 3.7: Supplementary Figure 2. 17A2 Fab'-DNA synthesis and purification. The fragmentation of 17A2 is monitored by SDS-PAGE and the purity of 17A2 Fab'-DNA-Atto647N after purification over ion exchange and size exclusion columns is assessed. A line scan of the purified Fab'-DNA shows that about two thirds of the fluorescent species are Fab'-DNA and the majority of the contaminants are smaller DNA-conjugated fragments which cannot bind TCR.

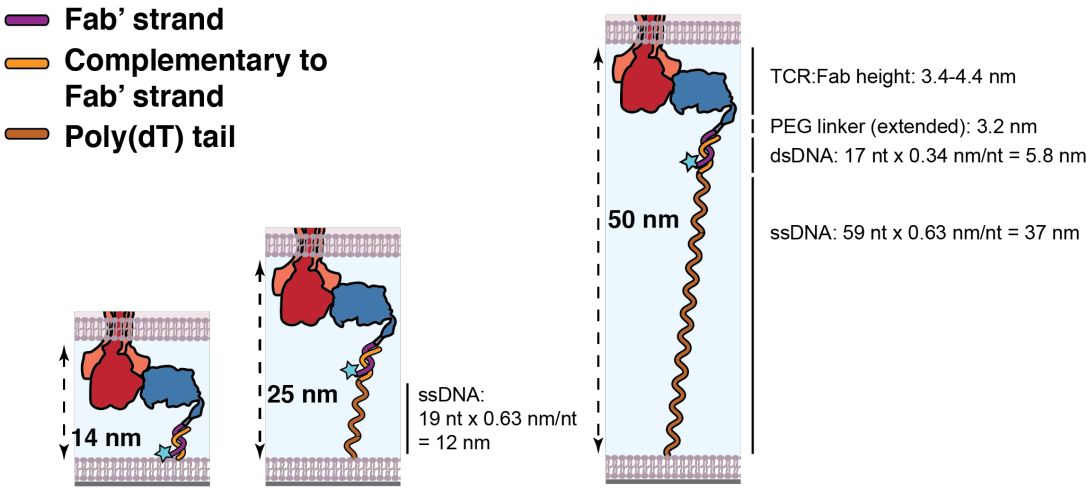

Figure 3.8: Supplementary Figure 3. Approximation of intermembrane space allowed at binding events, assuming oligonucleotides can fully stretch. The intermembrane space for each thiol-DNA tether was estimated using the structure of H57 Fab bound to TCR, PDB 1NFD, the estimated length of the PEG linker, the height of a double stranded DNA base pair, and the height of a single stranded DNA nucleotide.

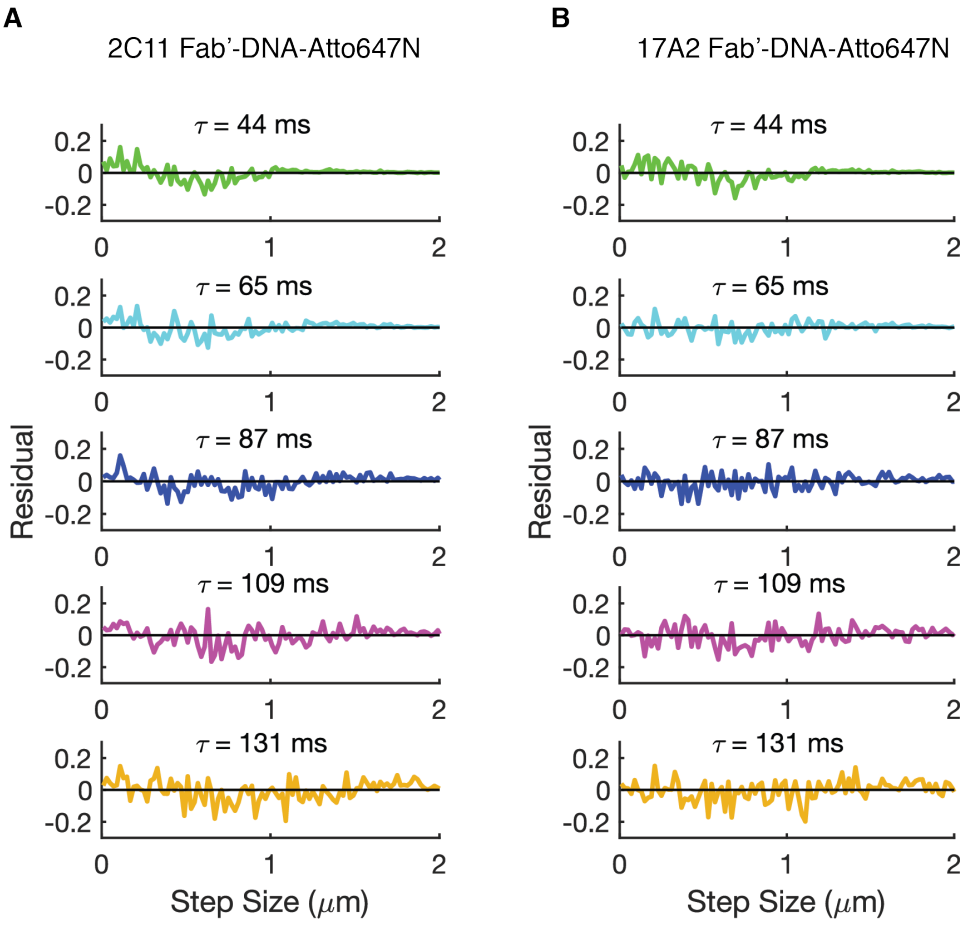

Figure 3.9: Supplementary Figure 4. Step size distributions. Residuals from **(A)** 2C11 Fab'-DNA and **(B)** 17A2 Fab'-DNA step size distributions at multiple delay times, fit by a two-dimensional single component Brownian diffusion model. Data from all time delays were fit simultaneously with Eqn. 1 to obtain a single diffusion coefficient for each Fab'-DNA construct.

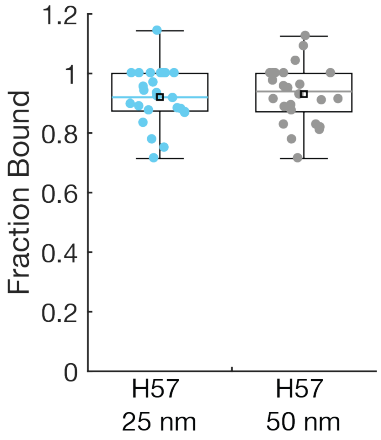

Figure 3.10: Supplementary Figure 5. Fraction bound of longer tethers. Fraction bound for H57 Fab'-DNA with medium and long tether lengths are nearly identical to each other and H57 Fab'-DNA with the short tether. Colored bar: median; black square: mean; box: interquartile range; whiskers: data within 1.5x IQR. H57 25 nm: n = 25; H57 50 nm: n = 26.

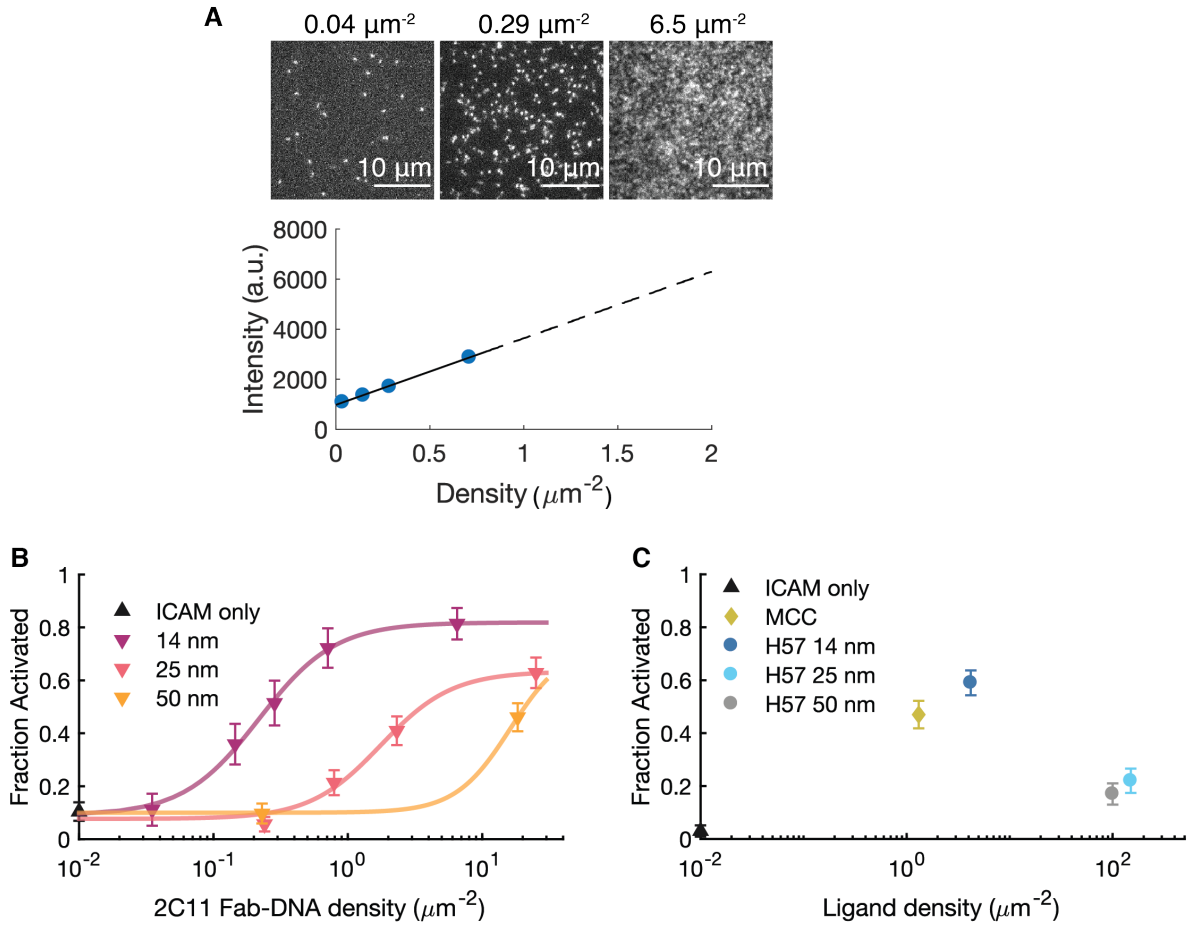

Figure 3.11: Supplementary Figure 6. Supplemental NFAT activation data. (A) The density of ligand on the bilayer is determine by TIRF intensity. The total intensity and particle density are measured at densities for which particles are countable. The density-intensity calibration curve is then extrapolated to determine the density of ligand on high-density bilayers. **(B)** NFAT titration curves for 2C11 Fab'-DNA with varied tether lengths. The inflection points for all three constructs roughly match those for the corresponding H57 constructs. **(C)** Even at very high (100 μm^{-2}) density, H57 Fab'-DNA constructs that allow up to 25 nm and 50 nm intermembrane space do not fully activate T cells compared to the 14 nm Fab'-DNA and pMHC controls, though they do activate significantly above the ICAM only negative control. Of note, cells in the experiment shown had a low maximal fraction of cells that activated in response to short ligands (0.6 compared to 0.8), which may relate to why the fraction activated, especially from the medium tether ligand, is low compared to the data set shown in panel (B) and Fig. 3.4D.

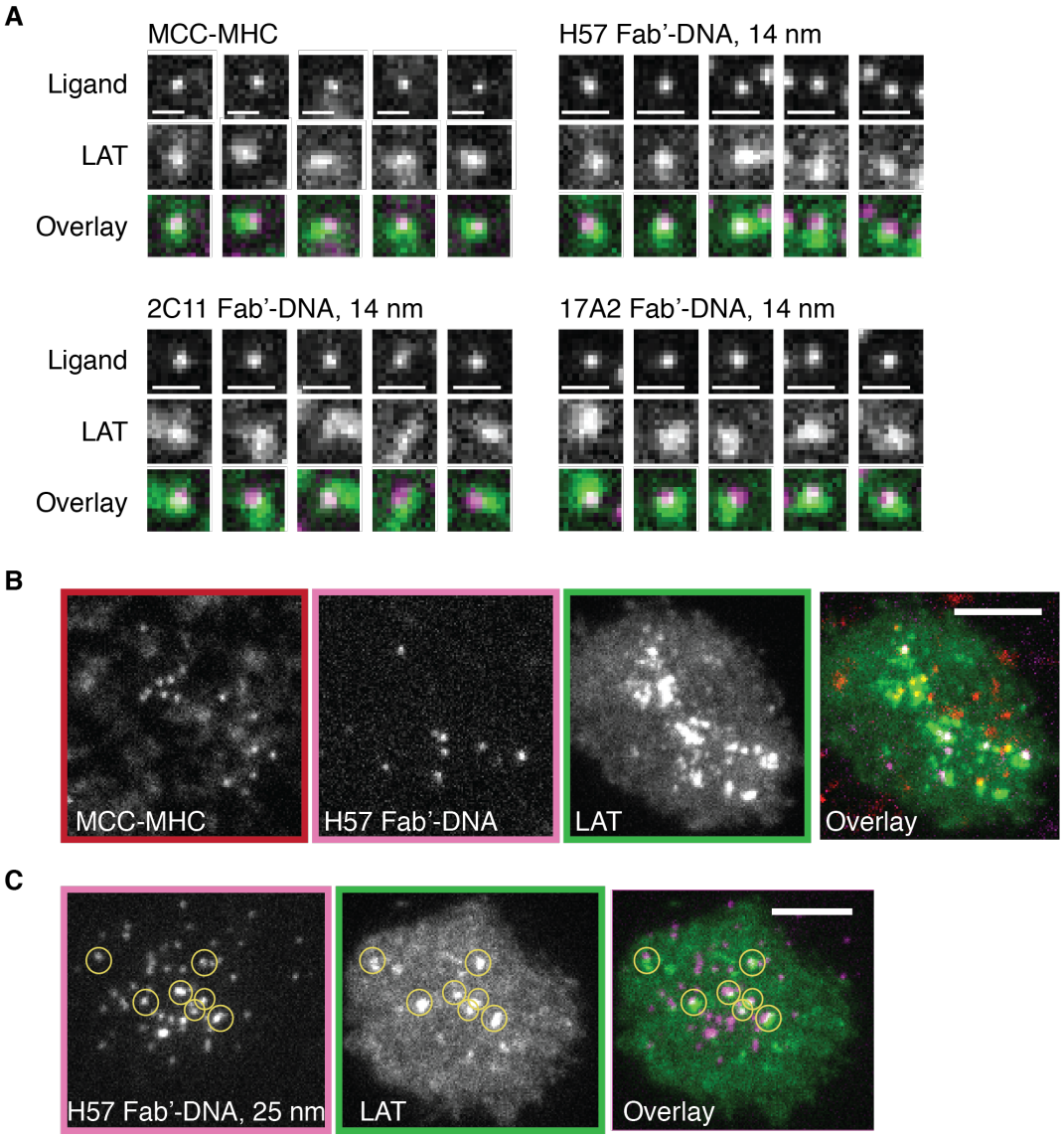

Figure 3.12: Supplementary Figure 7. LAT clustering in response to binding events. **(A)** Examples of single binding events colocalized with LAT clusters for potent ligands. Scale bars 1 μm. **(B)** LAT condensates form in response to binding events between TCR and both H57 Fab'-DNA-AlexaFluor555 (14 nm) and pMHC-Atto647N when both ligands are presented at low density on the SLB. Binding events from both ligands appear to have an additive effect on signal transduction. Scale bar 5 μm. **(C)** Instances where LAT clusters form in response to weak ligands often colocalize with a cluster of binding events. Scale bar 5 μm.

3.8 Appendix: Analysis of Long Dwell Times In Limited Detection Windows Using A Maximum Likelihood Estimate

Introduction

Fab'-DNA constructs synthesized from commercially available antibodies have very high affinities. Single molecule dwell times often last longer than the observation time or become obscured as they are tracked to the geometric center of the cell and merge with fluorescent signal from other bound ligands. Ideally, dwell time distributions should be built from binding events, tracked reliably throughout their lifetime, that either unbound or photobleached within the observation window. However, this condition would result in tossing out the nearly half of all collected dwell time data. Dwell time distributions presented in this published work therefore include all data and provide a lower bound for the mean dwell time of each Fab'-DNA ligand. However, they do not represent an accurate measure of each ligand's mean dwell time.

Given the experimental constraints on accurately visualizing the dwell time of each binding event experienced by cells with these long-dwelling ligands, a more appropriate method for analyzing mean dwell time would take into account binding events that unbound or photobleached, in this appendix, referred to as dwell events, and events that become untrackable due to localization to the immunological synapse or are present in the last frame of the acquisition, referred to here as survival events. By properly analyzing both the dwell events and survival events, we can more accurately measure the true mean dwell time of each ligand.

Derivation

A maximum likelihood estimate can incorporate both dwell events and survival events to estimate the most likely true mean dwell time for a species.

Let λ be the characteristic off-rate of Fab':TCR binding interaction.
Let $t_1, t_2, ..., t_m$ be the dwell times of Fab's that either unbind TCR or bleach within the acquisition.
These events sample a normalized single exponential decay:

$$p(t_m) = \lambda e^{-\lambda t_m}$$

$$p(t_1, t_2, ..., t_m) = \lambda^m e^{-\lambda \sum_{i=1}^{m} t_i}$$

Let $c_1, c_2, ..., c_n$ be the survival times of Fab's that neither unbind TCR nor bleach within the acquisition.
These events sample the survival distribution of a single exp decaying variable:

$$p(c_n) = e^{-\lambda c_n}$$

$$p(c_1, c_2, ..., c_n) = e^{-\lambda \sum_{j=1}^{n} c_j}$$

The likelihood of a given value λ for the set of observed dwell times and survival times is:

$$\mathcal{L}(\lambda; t_1, t_2, ..., t_m, c_1, c_2, ..., c_n) = \lambda^m e^{-\lambda \sum_{i=1}^{m} t_i} e^{-\lambda \sum_{j=1}^{n} c_j}$$

$$= \lambda^m e^{-\lambda \sum_{i=1}^{m} t_i + \sum_{j=1}^{n} c_j}$$

The maximum likelihood of λ can be found by taking the derivative of L with respect to λ and setting it to zero:

$$\frac{d\mathcal{L}}{d\lambda} = 0$$

Or, because logarithms are monotonically increasing functions, we can maximize the log of L:

$$\frac{dln(\mathcal{L})}{d\lambda} = 0$$

$$ln(\mathcal{L}) = mln\lambda - \lambda(\sum_{i=1}^{m} t_i + \sum_{j=1}^{n} c_j)$$

$$\frac{dln(\mathcal{L})}{d\lambda} = \frac{m}{\lambda} - (\sum_{i=1}^{m} t_i + \sum_{j=1}^{n} c_j) = 0$$

$$\frac{m}{\lambda} = (\sum_{i=1}^{m} t_i + \sum_{j=1}^{n} c_j)$$

$$\lambda = \frac{m}{(\sum_{i=1}^{m} t_i + \sum_{j=1}^{n} c_j)}$$

m – number of dwells that unbind or bleach.
$\sum_{i=1}^{m} t_i$ – total duration of all dwells that unbind or bleach.
$\sum_{j=1}^{n} c_j$ – total duration of all dwells that last until the final frame.

This relatively simple calculation, dividing the number of dwell events by the cumulative time of all dwell and survival events, gives the characteristic off-rate of a ligand. The inverse gives the ligand's characteristic dwell time.

Analysis of 2C11 Fab'-DNA and MCC-MHC characteristic dwell times

To demonstrate the power and relative simplicity of this method, I analyze dwell time data from two cells, one on a 2C11 Fab'-DNA bilayer and one on an MCC-MHC bilayer, and extract the maximum likelihood estimate for each ligand's true mean dwell time. Each binding event experienced by a cell (Figs. 3.13 and 3.14, panel A) is sorted based on whether

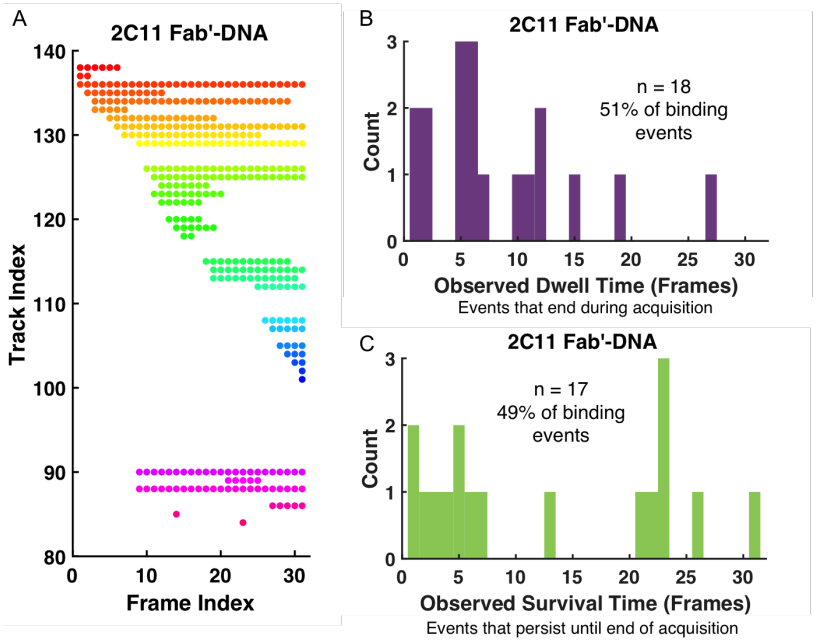

Figure 3.13: 2C11 Fab'-DNA binding events experience by a landing cell. **(A)** Start time and duration of each binding event, sorted by track index. Frame rate: 10 s. **(B)** Histogram of all dwell events, sorted by their duration. **(C)** Histogram of all survival events, sorted by their duration

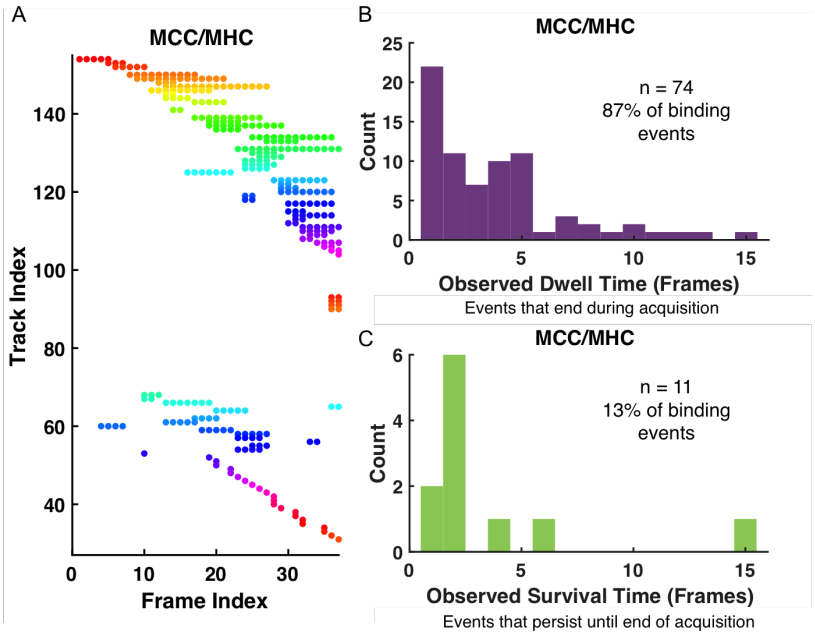

Figure 3.14: MCC-MHC binding events experience by a landing cell. **(A)** Start time and duration of each binding event, sorted by track index. Frame rate: 10 s. **(B)** Histogram of all dwell events, sorted by their duration. **(C)** Histogram of all survival events, sorted by their duration

it unbinds or photobleaches within the acquisition (Figs. 3.13 and 3.14, panel B) or persists until the end of the acquisition (Figs. 3.13 and 3.14, panel C).

Only 51% of 2C11 binding events unbind or bleach during the acquisition, and those that do sample a single exponential decay quite poorly (Fig. 3.13 B). Much more data would need to be gathered to better sample the short-dwell-time region of the dwell time distribution, and the long-dwell-time region would not be able to be sampled due to experimental limitations. In contrast, 87% of MCC-MHC binding events unbind or bleach during the acquisition and these events, even from only one cell, could be fit by a single exponential decay (Fig. 3.14 B). The entire distribution, both at shorter and longer dwell times, appears to be well-sampled.

Analyzing the maximum likelihood estimate (MLE) for both 2C11 Fab'-DNA and MCC-MHC yields the following. Error is estimated from bootstrapping the data.

2C11 Fab'-DNA

$$\begin{aligned}
\lambda &= \frac{m}{(\sum_{i=1}^{m} t_i + \sum_{j=1}^{n} c_j)} \\
&= \frac{number\ of\ dwell\ events}{cumulative\ sum\ of\ dwells\ +\ cumulative\ sum\ of\ survivals} \\
&= \frac{18}{152 + 216} \\
&= 0.0498\ frames^{-1} \\
\tau &= \frac{1}{\lambda} = 20.4\ frames = 200 \pm 30\ s\ (SD)
\end{aligned} \tag{3.2}$$

MCC-MHC

$$\begin{aligned}
\lambda &= \frac{m}{(\sum_{i=1}^{m} t_i + \sum_{j=1}^{n} c_j)} \\
&= \frac{74}{283 + 39} \\
&= 0.23\ frames^{-1} \\
\tau &= \frac{1}{\lambda} = 4.35\ frames = 44 \pm 4\ s\ (SD)
\end{aligned} \tag{3.3}$$

The results from MCC-MHC match very well with the accepted MCC-MHC:AND TCR mean dwell time of about 50 s, noting that the MLE presented here is not yet corrected for photobleaching. The MLE is within error of the reported τ_{obs} for MCC-MHC of 46 ± 2 s (Fig. 3.3). In contrast, the mean dwell time of 2C11 Fab'-DNA resulting from the maximum

likelihood estimate, 200 ± 30 s is significantly longer than the reported observed dwell time for 2C11 Fab'-DNA of 135 ± 18 s. Moving forward, the mean dwell time for long-dwelling ligands in these live-cell SLB assays should use this maximum likelihood estimate method, incorporating both dwell events and survival events, in order to best capture the true binding kinetics of the ligands under investigation.

Analyzing the precision of the MLE method with simulations

The precision with which the MLE method can estimate the true mean dwell time of a ligand depends on the length of the dwell time and imaging parameters such as the length of time once cell is imaged and the number of binding events captured in each acquisition. Practical constraints in the experiment, such as binding events funneling to the geometric center of the cell within two to four minutes (12 to 24 frames, with the 10 s time lapse used for these long-dwelling ligands), and low ligand density in order to reliably track binding events through time, limit the amount of information that can be obtained from one cell. I ran simulations for a general ligand with a 20 frame true dwell time to visualize the distribution of measured mean dwell times under a range of imaging acquisition parameters (Fig. 3.15). I find that, if the number of frames per acquisition is at least on par with the true mean dwell time, precision can be notably enhanced by increasing sampling of the distribution from 50 events to 800 events.

The simulation condition that most closely matches the experimental 2C11 Fab'-DNA data (Fig. 3.13) is the condition with a 30-frame acquisition and 200 binding events. The standard deviation of 500 simulation replicates is about 3 frames, or 30 s, in agreement with the bootstrapping protocol done to estimate error from the experimental data. As these data are assembled from only one cell, it is reasonable to collect data from four to six cells to enhance the precision by a factor of two or more.

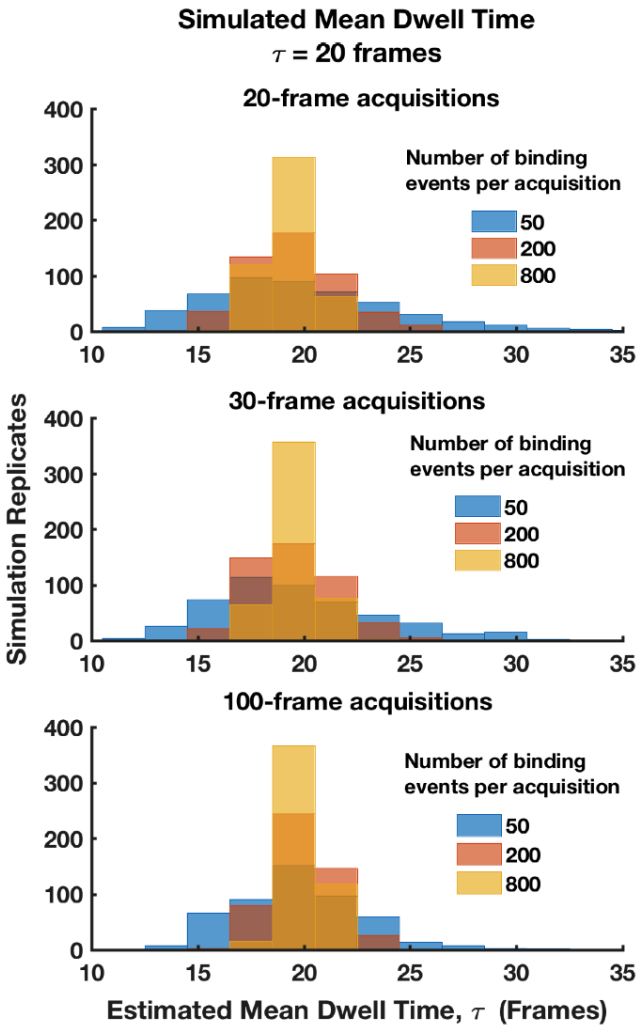

Figure 3.15: Simulated precision of the maximum likelihood estimate given a true mean dwell time of 20 frames and varied acquisition parameters. The distribution of 500 simulation replicates is given for acquisitions of 20, 30 and 100 frames and for 50, 200, and 800 binding events occurring across those frames in time. The width of the distribution for a given set of acquisition parameters indicates the precision with which the true mean dwell time can be known under those conditions.

Chapter 4

Modulating Fab binding kinetics through mutations

Kiera B. Wilhelm[1], Anand Vissa[1], Jay T. Groves[1]

[1] Department of Chemistry, University of California, Berkeley, Berkeley, United States

4.1 Introduction

T cells integrate information from binding interactions between their T cell receptors (TCRs) and peptide major histocompatibility complex (pMHC) ligands displayed on antigen presenting cells (APCs) to make cell fate decision. Developing thymocytes undergo differential positive or negative selection across a narrow affinity range, ensuring that they are able to interact with self- MHC molecules while minimizing escape of T cells reactive to self-peptides to the periphery [126, 127]. In the periphery, T cells receive survival signals from low-affinity self pMHC and activate and differentiate in response to higher-affinity pathogenic pMHC [128]. Both binding affinity [129, 130] and kinetic off-rate [131, 132] correlate with cellular response, though neither are fully predictive of ligand potency [58, 133].

Kinetic proofreading [134] provides a model for how the T cell signaling machinery senses and responds to ligand dwell time. According to the kinetic proofreading model, a series of irreversible, energy-requiring steps, such as phosphorylations, must occur at the TCR while it is bound to ligand before reaching a signaling-competent state [26, 27]. For individual dwell events to be accurately sensed, the TCR signaling complex must rapidly dissociate upon ligand unbinding. The molecular details of kinetic proofreading at the TCR, and the mechanisms by which they set ligand discrimination thresholds, are beginning to be illuminated [97, 135, 136].

High ligand on-rates are proposed to create long effective dwells for ligands with shorter dwell times but high affinity through serial triggering of the same TCR [34, 137]. Serial triggering models assume that rebinding can occur very rapidly relative to the mobilities of pMHC and TCR in their respective membranes, allowing a pMHC molecule to rebind the same TCR. If rebinding also occurs rapidly relative to the dissociation of the TCR signaling complex required for kinetic proofreading, the argument goes, serial triggering could provide a unified model for explaining discrepancies in correlations between activity either dwell time or affinity [34]. In experiments studying TCR triggering and cell activation from ligand presented on supported lipid bilayers, pMHC mobility is too high to support serial triggering of the same TCR [47], yet coordination between brief binding events that occur sequentially in the same spatial neighborhood may cooperatively contribute to downstream signaling[9].

However, very strong TCR binders, while the most potent in *in vitro* assays [133], do not necessarily elicit the greatest immune response *in vivo*[96]. Solution affinities for native pMHC binding TCR range from 1-10 μM for agonist pMHC and > 10 μM for antagonist or null pMHC, which is quite weak for ligand:receptor interactions. The T cell signaling network may be tuned to respond optimally to TCR ligands in the low- to mid-micromolar range [138, 139].

Understanding how T cells mechanistically integrate information from binding kinetics and respond to non-physiological TCR binding parameters is of critical importance given the rapid development of synthetic T cell engagers for cancer immunotherapy. Current efforts to therapeutically control T cell activation by directing T cell cytotoxic activity to cancerous cells employ moieties that bind receptors on T cells very strongly. Bispecific T cell engagers use antibody-derived fragments to bridge cancer markers on tumors to T cell receptors [41–43]. These T cell engagers are capable of universally binding all T cells and the antibody fragments used have very high, low-nanomolar affinities. Strong binding and lack of targeted T cell response are accompanied by serious clinical complications such as cytokine storm [39, 140]. Alternatively, chimeric antigen receptors (CARs), with an antibody-derived tumor binding moiety engineered directly into the receptor, are transfected into patients' T cells and reintroduced, redirecting these cells' activity to the target of interest. CARs fail to trigger classic signatures of T cell activation [141] and have blunted antigen sensitivity [142]. There is growing acknowledgement that care needs to be taken with ligand:receptor binding affinity during the design of synthetic T cell engager and CAR therapeutics in order to maximize efficacy while minimizing adverse side effects. However, specifics of how to design ligand binding kinetics into cancer immunotherapeutic remains under investigation, in part because the mechanism by which T cells read and integrate TCR ligation kinetics remains unresolved.

We have previously introduced a class of antibody-derived T cell engagers, composed of an anti-TCR/CD3 Fab' fragment covalently linked to a short DNA oligonucleotide, to universally activate T cells in quantitative supported lipid bilayer (SLB) assays [102]. These

Fab'-DNA ligands mimic many properties of physiological TCR triggering and cellular activation by pMHC ligands [4–6, 12, 47]. They are strictly monovalent ligands incapable of activating T cells from solution at any concentration, but become potent activators when bound to an SLB [102]. Single ligation events between Fab'-DNA and TCR are sufficient to produce significant TCR-proximal phosphorylation activity [48], and cells can activate in response to a handful of sparse, well-spaced ligation events [8, 102]. Like with pMHC and other T cell engagers [25, 42, 43], T cells are sensitive to the spacing between apposed membranes enforced at Fab'-DNA:TCR binding events [48]. Because the anti-TCR/CD3 Fab' fragments bind constant regions of the TCR complex rather than the hypervariable pMHC recognition site, they are able to activate T cells regardless of their clonotype. However, like other antibody-based TCR binders, the Fab'-DNA ligands developed thus far have very high affinities and long dwell times, binding the TCR for a mean dwell time of over 2 min [48] compared to a range of subsecond to about 10 seconds for self- and agonist- pMHC [8].

Series of altered peptide ligands have been critically important to gaining understanding of how T cells discriminate between self- and foreign peptide-loaded MHC molecules [34, 96, 97, 127, 137, 143, 144]. These systems require studying clonal T cells that are all reactive to the same altered peptide ligand series, often requiring design and maintenance of particular murine lines, with additional manipulations engineered within this specific TCR background [97, 145]. A Fab'-DNA affinity panel would allow T cell response to ligands with varied binding kinetics to be studied directly in any clonal or polyclonal background, easing engineering requirements. Moreover, Fab'-DNA ligands with binding kinetics similar to pMHC could be used to quantitate the sensitivity of cells to ligand binding kinetics in polyclonal T cell populations.

Here, we express the anti-TCRβ Fab fragment H57-597 recombinantly in *E. coli* and modulate its binding affinity with TCR by introducing point mutations at the Fab:TCR binding interface. Expressed Fabs are covalently linked to short, fluorescently labeled DNA oligonucleotides, as done with Fabs previously purified from commercially available antibody, and introduced to SLBs bearing the complementary DNA oligonucleotide. T cells land on the SLB through adhesion interaction between intercellular adhesion molecule 1 (ICAM-1) on the SLB and lymphocyte function-associated antigen 1 (LFA-1) on the T cell. Fab'-DNA:TCR binding events at the SLB-T cell interface and resulting downstream signaling consequences are visualized concurrently using fluorescence microscopy. The goals of developing lower-affinity Fabs through expression and mutation are two-fold: (1) to gain mechanistic insight into how on- and off-rate are read and integrated by the T cell signaling network and (2) to develop synthetic anti-TCR ligands with binding kinetics more similar to pMHC to quantitatively study signal integration in polyclonal T cell populations.

We find that the point mutant H57 R97L Fab'-DNA retains a high on-rate but has a significantly shorter dwell time than parental H57 Fab'-DNA. Like with pMHC and other Fab'-DNA constructs, the linker for activated T cells (LAT) condenses downstream of single

H57 R97L Fab'-DNA:TCR ligation events, but only after a long delay. LAT is a disordered protein that scaffolds a TCR-proximal signaling hub from which major pathways in the TCR signaling network, Ca^{2+} release and mitogen-activated protein kinase cascade, branch [114]. LAT undergoes a phosphorylation-dependent phase transition downstream of TCR triggering [146, 147], and this phase transition regulates activity of critical enzymes such as the Ras guanine exchange factor Son of Sevenless (SOS) [148] and phospholipase Cγ1 (γ1) [149]. The long delay between single ligation events and LAT condensation is suggested to provide another layer of kinetic proofreading beyond the TCR itself. In addition, the high on-rate of H57 R97L Fab'-DNA leads to enhanced cooperativity between binding events. LAT condensates have been suggested to integrate information across spatially correlated short-dwelling binding events that exceed some minimal threshold to trigger TCR, providing persistence in the signaling network across multiple TCR ligation events [7, 9]. We find that the high on-rate of H57 R97L Fab'-DNA leads to increased probability of a cell experiencing multiple short, successive binding events in the same neighborhood, and that these multiple short successive binding events are able to cooperatively contribute to increasing the probability of LAT condensate formation. These findings provide a mechanistic explanation to how effective dwell times predicted by serial triggering models [34, 137] are calculated and processed using cellular machinery.

We investigate cellular activation in response to H57 R97L Fab'-DNA by imaging translocation of the nuclear factor of activated T cells (NFAT), which provides a binary readout of signaling through the calcium pathway. The dose-response curve of primary murine $CD4^+$ effector T cells clonally expressing the AND TCR in response to H57 R97L Fab'-DNA falls between curves for the long-dwelling MCC-MHC and dwell-time-matched T102S-MHC. Moreover, parental H57 Fab'-DNA and the R97L mutant are able to activate polyclonal murine $CD4^+$ effector T cells in a dwell-time-dependent manner. T cells exposed to H57 Fab'-DNA bilayers reach half-maximal activation at 0.15 μm^{-2} while those exposed to H57 R97L Fab'-DNA bilayers reach half-maximal activation at 1 μm^{-2}. This Fab' expression platform provides the means to develop affinity panels reactive to T cells regardless of their clonotype in order to quantitatively study how T cells integrate kinetic information and variation in sensitivity across different T cell populations.

4.2 Results

H57 Fab' expression enables the introduction of affinity-modulating mutations

Commercial antibodies developed to bind and trigger TCR have high affinities for these purposes. In order to develop Fab'-DNA ligands with decreased binding affinities that more closely resemble pMHC, we adopted the pCES1 Fab expression vector designed to screen Fabs using phage display and express hits in *E. coli* (Fig. 4.1A) [150, 151]. The pCES1 vector

contains signal sequences directing the heavy chain and light chain to the periplasm, an oxidizing environment, where disulfide bonds form a fully-assembled Fab. His- and myc- tags are included at the c-terminus of the heavy chain for Fab purification and Western blotting applications. We appended a GGGC linker directly to the Fab heavy chain for conjugation to maleimide-functionalized DNA and a TEV recognition site between the GGGC linker and the His-tag. Cleaving off this His-tag prevents multivalent interactions between Fab'-DNA and supported lipid bilayers (SLBs) functionalized with the complementary oligonucleotide and Ni^{2+}-chelated nitrilotriacetic acid (NTA). An amber stop codon separates the tags and geneIII, terminating expression after the Fab heavy chain in standard *E. coli* strains and enabling phage display in amber suppressor strains.

Targeted point mutations were introduced into H57 Fab, informed by its crystal structure [77], to weaken interfacial contacts. The complementarity-determining region 3 (CDR3) of the H57 Fab heavy chain forms numerous atomic contacts with TCRβ, including hydrogen bonding between R120 on TCRβ and R97 and F98 on the Fab (Fig. 4.1B). A flow cytometry screen of crude periplasm extract from three Fabs with point mutations in CDR3 show that all mutants tested had decreased binding affinity to primary murine T cells compared to the parental Fab, but none had a signal that rose significantly above the negative background controls. An arginine to leucine mutation that breaks a hydrogen bond and decreases affinity in the anti-human CD3ϵ OKT3 Fab fragment [99] suggested that a similar mutation in H57 could be effective. Purifying the H57 R97L Fab' in *E. coli* and conjugating to a dye-labeled DNA oligonucleotide through maleimide-thiol chemistry [102] yielded a clean sample of H57 R97L Fab'-DNA for analysis in live-cell imaging assays (Fig. 5.1C).

R97L point mutation lowers H57 Fab'-DNA dwell time while retaining a high on-rate

Binding kinetics between H57 R97L Fab'-DNA and TCR were characterized at the interface between SLBs and primary AND $CD4^+$ effector T cells in the context of ICAM-1:LFA-1 adhesion at 37 °C. Fluid, low-defect SLBs were formed from 95% DOPC, 3% MCC-PE, and 2% Ni-NTA-DOGS lipids. A thiol-functionalized DNA oligonucleotide, complementary to the Fab'-DNA, was covalently linked to MCC-PE lipids at 100's μm^{-2}, and Fab'-DNA density on the bilayer was then precisely controlled by incubation concentration and duration. ICAM-1 coupled to SLBs at 100's μm^{-2} through multivalent interactions between the His-tag on ICAM-1 and Ni^{2+} chelated by NTA-DOGS lipids.

T cells added to SLBs adhered through ICAM-1:LFA-1 interactions and bound Fab'-DNA within this intermembrane junction (Fig. 4.2A). All Fab'-DNA on the bilayer were visualized using total internal reflection fluorescence (TIRF) microscopy with a short, 20 ms exposure time (Fig. 4.2B, top). Fab'-DNA molecules bound to TCRs have dramatically reduced mobility compared to free Fab'-DNA, and so they can be selectively resolved using a long, 500 ms exposure time (Fig. 4.3B, bottom) [47]. The long exposure time blurs the image

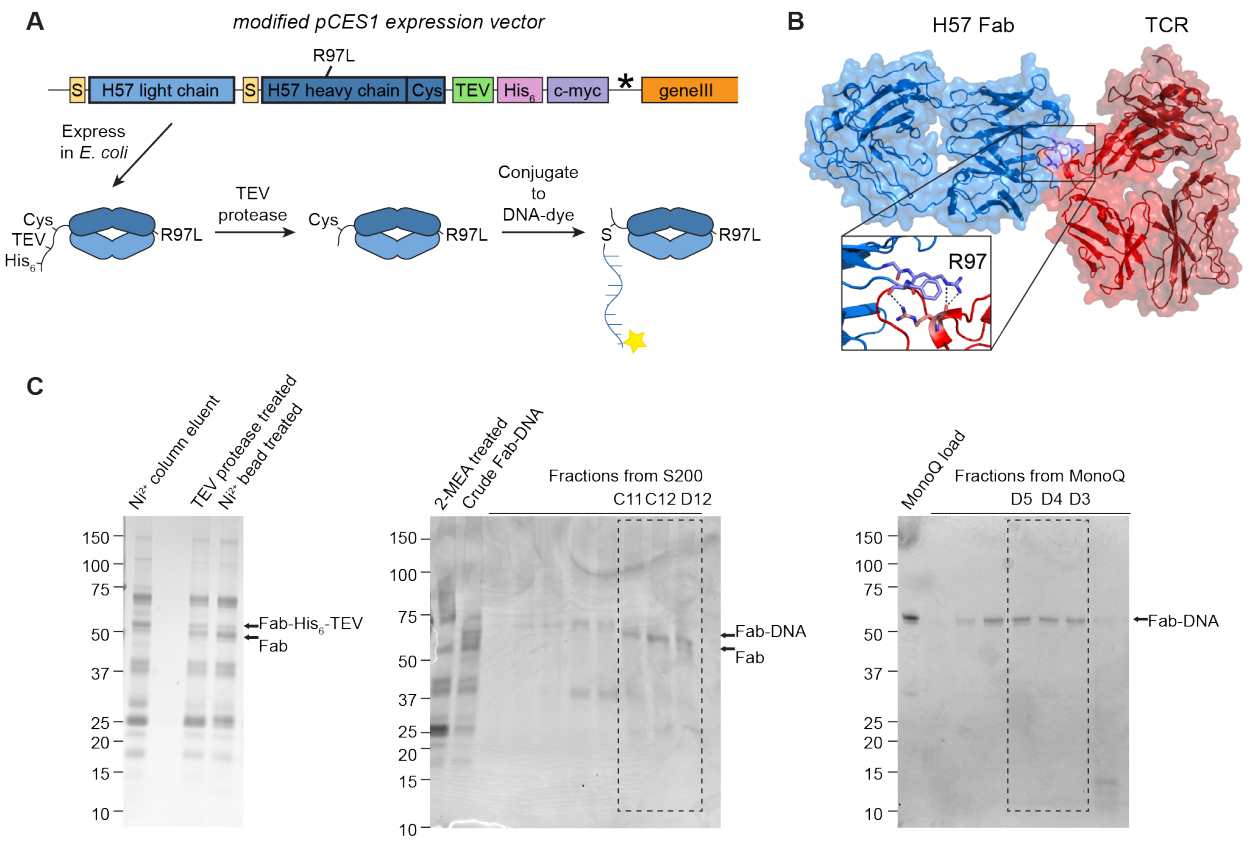

Figure 4.1: H57 Fab' expression enables the introduction of point mutations. (A) The pCES1 expression vector was used to express H57 Fab in *E. coli*. The R97L mutation was introduced to decrease the affinity between the H57 Fab and TCR. A GGGC linker was appended to the c-terminus of the heavy chain to allow for conjugation to the dye-labeled DNA oligonucleotide. A TEV site was introduced to cleave off the His_6 tag after purification. An amber stop codon (*) followed by bacteriophage geneIII allows for phage display in amber surpressor *E. coli* strains. **(B)** Crystal structure of H57 Fab bound to TCR shows hydrogen bonding contacts between R97 and F100 on H57 Fab heavy chain and R120 on TCRβ. PDB: 1NFD. **(C)** Expression and purification of H57 R97L Fab'-DNA was monitored by SDS-PAGE.

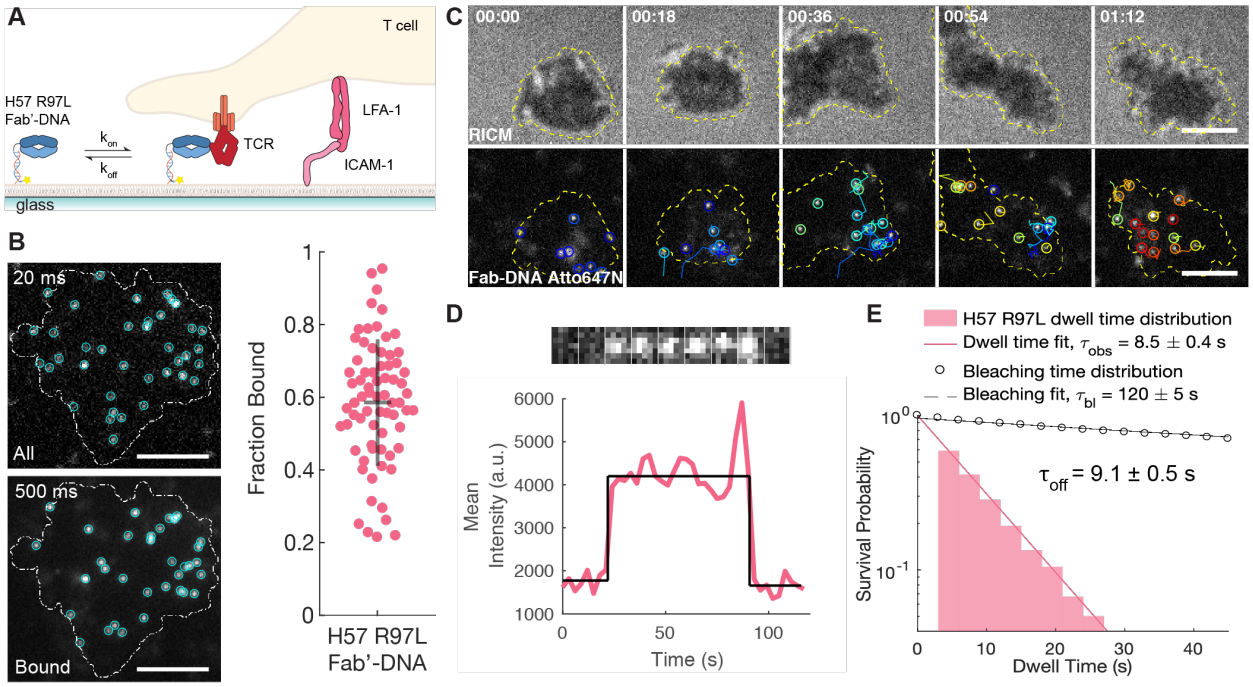

Figure 4.2: R97L point mutation lowers H57 Fab'-DNA dwell time while retaining a high on-rate. **(A)** H57 R97L Fab'-DNA presented on a glass-supported lipid bilayer binds to TCR in the context of LFA-1:ICAM-1 adhesion in live cell assays. **(B)** All H57 R97L Fab'-DNA under a cell footprint are resolved with a short exposure time and bound ligand are resolved with a long exposure time. The fraction of ligand bound is 0.6 ± 0.2. **(C)** Using a long exposure time, the R97L Fab'-DNA bound to TCR are imaged through time. **(D)** Tracks of single molecules are used to measure single interaction dwell times. **(E)** The observed dwell time distribution of H57 R97L Fab'-DNA fits a single exponential decay with an average dwell time of 8.5 ± 0.4 s. The dwell time is 9.1 ± 0.5 s after correction for photobleaching.

of fast-diffusing ligands, while slowly-moving bound ligands form a clear image. By taking successive images of all and bound Fab'-DNA under a T cell, the fraction of ligands bound to TCR can be directly measured. A high fraction, 0.6 ± 0.2, of H57 R97L Fab'-DNA ligands under cell footprints, visualized using reflection interference contrast microscopy (RICM), were bound to T cells (Fig. 4.2C). This is not as high as Fab'-DNA constructs derived from commercially available ligands, for which nearly all ligands under a cell are bound [48, 102], but is significantly higher than fraction bound measurement for pMHC ligands [8]. The fraction of bound ligands under a cell footprint is a measurement of the efficiency of ligand-receptor binding, and it can be used to determine the kinetic on-rate of a ligand when coupled with a quantification of TCR density [8].

Fab'-DNA dwell time, the inverse of kinetic off-rate, was directly visualized in supported bilayer assays. With Fab'-DNA presented at low density on the bilayer (0.08 μm^{-2}), single

ligation events between Fab'-DNA and TCR that occur at the SLB-T cell junction were tracked through time (Fig. 4.2C). Binding events were identified by a single step appearance in fluorescence intensity compared to background and tracked until bleaching or unbinding in a single step (Fig. 4.2D). The duration of every binding event was compiled into a dwell time distribution for H57 R97L Fab'-DNA, and the distribution was well-fit by a single exponential decay, indicating that unbinding occurs with first-order kinetics (Fig. 4.2E). After correcting for photobleaching, the mean dwell time for H57 R97L Fab'-DNA was 9.1 $\pm$ 0.5 s. This is much shorter than parental H57 Fab'-DNA dwell time of over 2 min and similar to the 5.2 s mean dwell time of native 5c.c7 TCR binding to its native agonist MCC-MHC [47].

Single binding events between H57 R97L Fab'-DNA and TCR can lead to LAT condensation after a significant delay

To investigate signaling in response to H57 R97L Fab'-DNA:TCR binding events, a bicistronic plasmid composed of LAT-eGFP-P2A-NFAT-mCherry was transduced into T cells two days after organ harvest using murine stem cell virus retroviral transduction. Overexpression of fluorescently-tagged LAT does not change signaling outcomes in T cells [7], and the fluorescently-tagged NFAT reporter lacks a DNA-binding domain, and so it also does not affect downstream signaling [82]. Binding events and LAT signal were imaged nearly concurrently through time, imaging first binding events using a long, 500 ms exposure time in the 640 TIRF followed by an image of the LAT signal using a 70-200 ms exposure time in the 488 TIRF channel. Single ligation events between H57 R97L Fab'-DNA and TCR were tracked through time using a 2 s time lapse and could trigger formation of a local LAT condensate (Fig. 4.3A). The binding events and resulting LAT condensates tracked together in time for their lifetimes, though over time the center of the LAT condensate drifts from the location of the bound TCR, indicating weak physical coupling (Fig. 4.3B). Significant signal amplification occurs upon LAT condensation, as one binding event leads to hundreds of phosphorylated, condensed LAT molecules [7] that recruit and are scaffolded by critical enzymes such as SOS [146, 147] and PLCγ1 [149].

A snapshot of all binding events and LAT condensates present in a cell shows that, at the low ligand density of 0.08 μm^{-2}, most LAT condensates colocalize with a single binding event (Fig. 4.3C). Montages of these binding events through time illustrate the relative timing and spatial localization of binding and LAT condensation (Fig. 4.3D). The first two montages show H57 R97L Fab'-DNA first binding TCR and then proximal LAT condensation, visualized by a rapid increase in local LAT intensity, after a delay of several seconds. The third montage shows a LAT condensate for which a preceding binding event was not observed, possibly due to fluorophore bleaching on the ligated Fab'-DNA [7]. Several seconds later, a fluorescent H57 R97L Fab'-DNA molecule binds a TCR located centrally in the condensate, and a few seconds after that, the condensate grows. Montages 4 through 6 show the lifetime of binding events for which LAT never condenses locally. It is noteworthy that these are

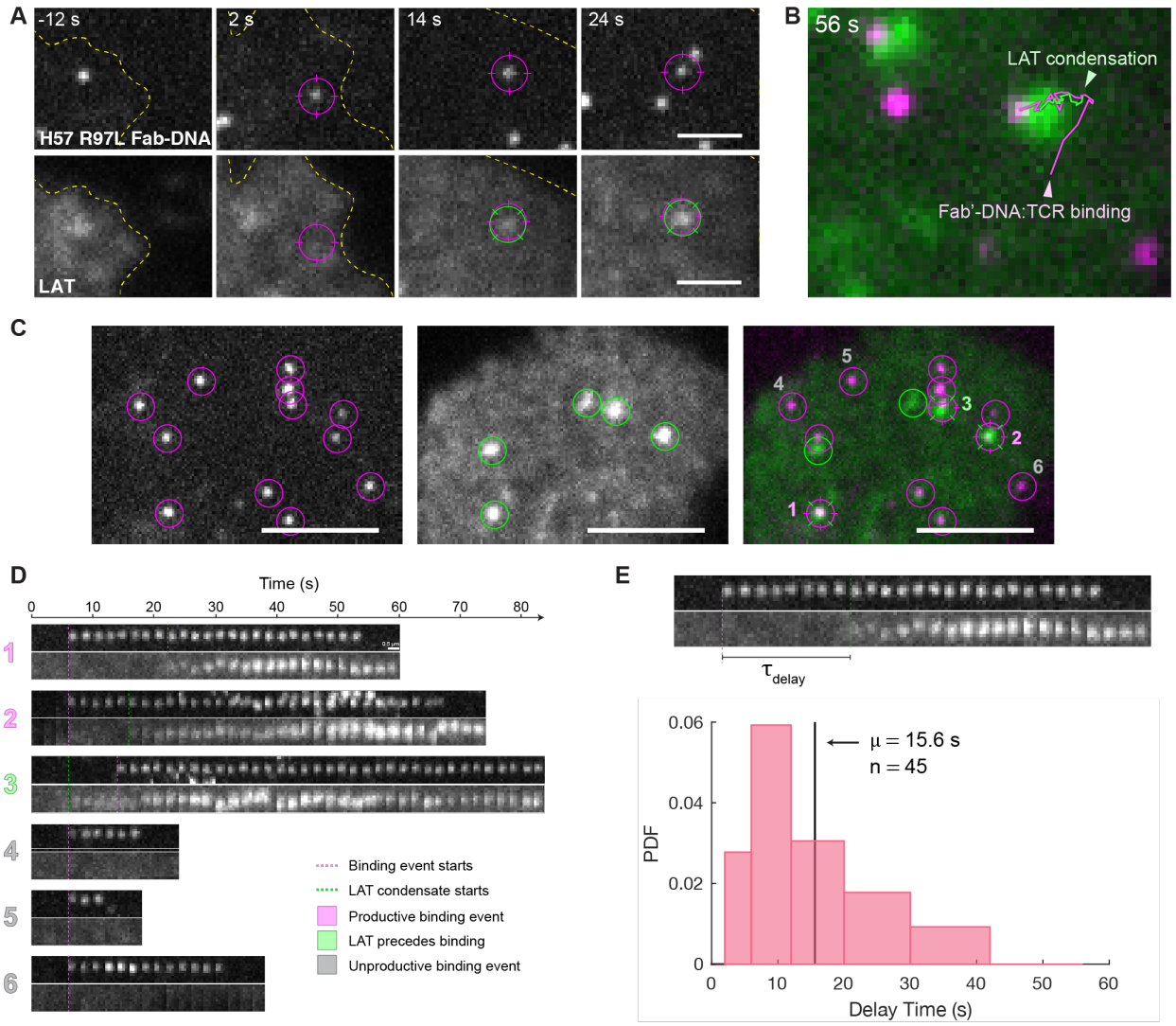

Figure 4.3: Single binding events between H57 R97L Fab'-DNA and TCR can lead to LAT condensation after a significant delay. **(A)** A montage illustrates a single binding event (magenta) followed by a proximal LAT condensate (green). Scale bar 2 μm. **(B)** The binding event and LAT condensate stay colocalized through time. Scale bar 2 μm. **(C)** In a still frame, some binding events colocalize with LAT condensates. Scale bar μm. **(D)** Tracks of those binding events through time and the local LAT signal. Binding events that last for a longer time are more likely to produce a local LAT condensate. Pink: Binding event produces a local LAT condensate. Green: A molecule of Fab'-DNA binds into an existing LAT condensate. Grey: Binding event does not produce a local LAT condensate. Scale bar 0.5 μm. **(E)** The delay time is defined as the time between Fab'-DNA binding to TCR and the initial formation of a LAT condensate. The distribution of delay times has a mean of 15.6 s, nearly twice as long as the mean dwell time.

among the shortest binding events of those that appear in the snapshot in Fig. 4.3C.

Single binding events that remained isolated from other binding events for the duration of their visualizable lifetime and produce local LAT condensates were identified, and the delay between initial ligand binding and the beginning of LAT condensation (τ_{delay}) was quantified. The histogram of delay times has a rise-and-fall shape with a mean delay of 15.6 s (Fig. 4.3E). The mean delay time is nearly twice as long as the mean ligand dwell time before correcting for photobleaching, indicating that it is the rare long-dwelling binding events that are generating significant downstream signaling activity. As it is only possible to extract a delay time from binding events that haven't bleached before LAT condensation commences, favoring LAT condensates that start sooner rather than later, the delay time measurement underestimates the true mean delay time between ligand binding and LAT condensation. The mean delay time for the much longer dwelling MCC-MHC is 23 $\pm$ 2 s [7]. Future analysis of the probability of LAT condensation given a dwell time will allow us to compare LAT response from H57 R97L, and also parental H57, directly to that of pMHC ligands. This preliminary evidence from dwell time distributions suggests that the delay time is similar between Fab'-DNA and pMHC and suggests that cells may employ a similar kinetic proofreading mechanism at the level of LAT condensation.

High on-rate leads to cooperativity among H57 R97L Fab'-DNA:TCR binding events in signaling to LAT

While isolated binding events must stay bound for a long period of time in order to generate sufficient downstream phosphorylation for LAT condensation, multiple nearby binding events can cooperate to contribute to a single condensate (Fig 4.4A). Each binding event is only present for a couple seconds, yet LAT condenses 6 s after the appearance of the first local binding event. This behavior suggests a local memory at the level of LAT phosphorylation, allowing information integration across binding events before the visualized transition from diffuse to condensed LAT. LAT condensation in response to sequential short binding events in the same spatial neighborhood has been seen previously with T102S-MCC [7] which has a dwell time of 9.6 s [9], nearly identical to that of H57 R97L Fab'-DNA. The high on-rate also appears to impact the distribution of cell-wide LAT condensation through time, with many condensates forming soon after cells landing on the bilayer and resuming a slower, more steady rate after an initial burst. This behavior is seen with both parental and R97L ligands, both of which have high on-rates (Fig 4.4 B,C). In contrast, LAT accumulates linearly in time for pMHC ligands [7]. The impact of an initial, coordinated burst in LAT condensation across the cell on the cell activation decision is, as of yet, unclear. As expected, LAT does not condense on bilayers presenting only ICAM, and the cumulative number of LAT condensates experienced by cells is greater for the higher affinity parental H57 Fab'-DNA compared to the R97L mutant.

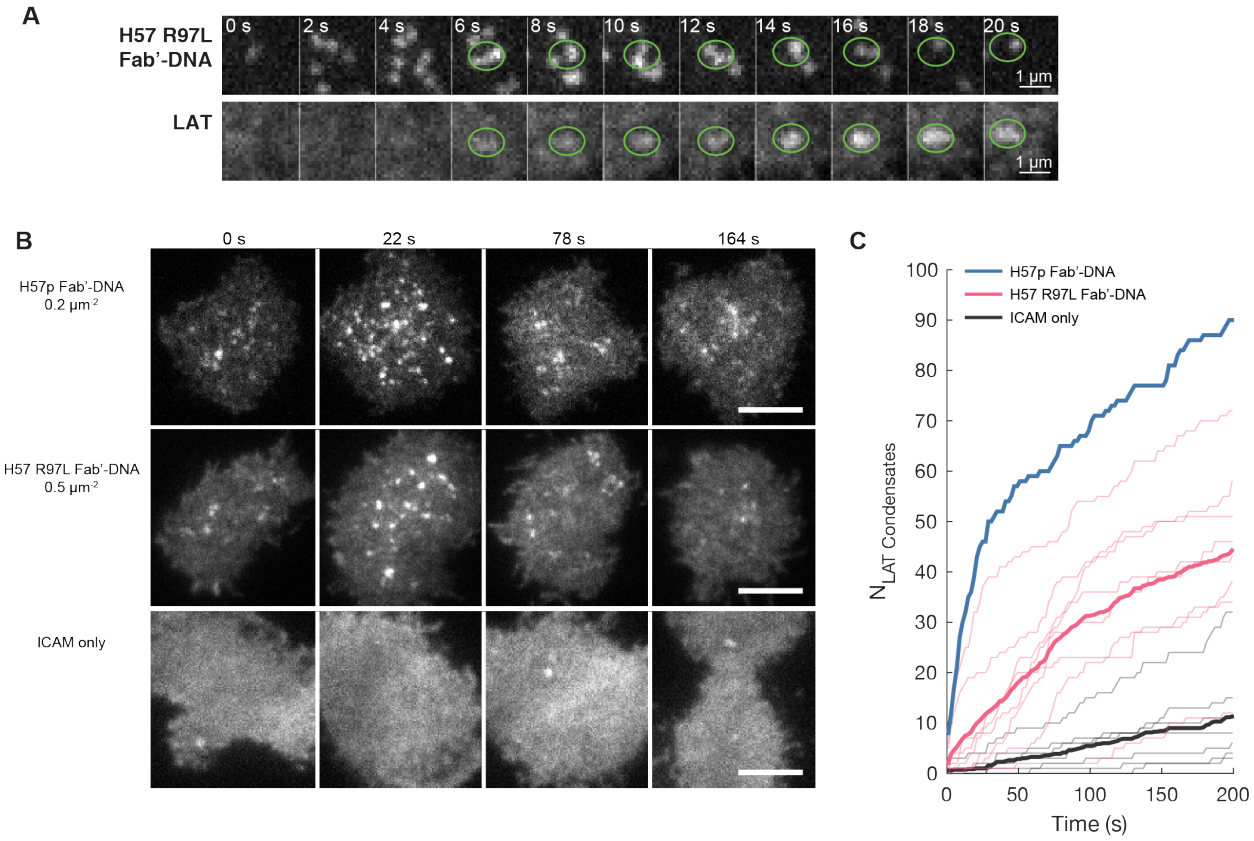

Figure 4.4: High on-rate leads to cooperativity between H57 R97L Fab'-DNA:TCR binding events in signaling to LAT. (A) Multiple binding events (top row) occur in the same region and cooperatively contribute to the formation of a LAT condensate (bottom row). Scale bar 1 μm.**(B)** Montages of LAT signal from cells shows a rapid accumulation of LAT condensation soon after landing on Fab'-DNA bilayers, which then settles to a more modest rate of LAT condensation accumulation. LAT condensates are sparse in cells on ICAM only bilayers. Scale bar 5 μm. **(C)** The cumulative number of LAT condensates through time for cells on parental H57 Fab'-DNA, H57 R97L Fab'-DNA, and ICAM only bilayers. Individual cell traces are denoted by thin lines and the average is denoted by thick, bold lines.

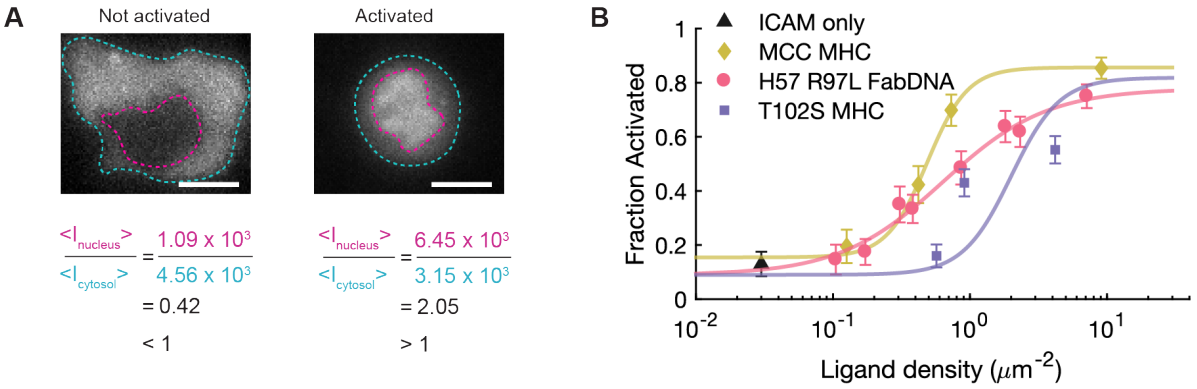

Figure 4.5: H57 R97L Fab'-DNA potency falls between MCC and T102S (A) Cells are defined as activated if the ratio of fluorescent signal in the nucleus to cytosol is greater than one. Scale bar 5 μm. **(B)** NFAT dose-response curve for MCC-MHC, H57 R97L Fab'-DNA and T102S-MHC.

H57 R97L Fab'-DNA potency falls between MCC and T102S

Activation of the calcium signaling pathway was determined using a fluorescent NFAT reporter protein. NFAT translocates to the nucleus downstream of calcium flux and is a binary reporter of early T cell activation [82]. Unlike calcium flux, which gives an analog response, NFAT translocation can be used to identify cells as either activated or not depending on whether or not fluorescence signal has accumulated in the nucleus. In our assays, a cell is defined as not activated when the ratio of signal in the nucleus compared to the cytoplasm is less than one (Fig. 4.5A, left) and active when the ratio is greater than one (Fig. 4.5A, right). The fraction of activated cells was assessed as a function of bilayer density after cells have interacted with the bilayer for 15 min. The dose-response curve for H57 R97L falls between that of MCC-MHC and T102S-MHC (Fig. 4.5B). The Fab'-DNA activates a similar fraction of cells at low antigen densities as MCC-MHC, perhaps due to coordinated binding events from the high on-rate. However, high antigen densities of R97L Fab'-DNA activate T cells more comparably to density-matched T102S-MHC bilayers. The H57 R97L Fab'-DNA reaches a half-maximal response (EC50) at about 1 μm^{-2}, which is greater than the EC50 of MCC-MHC of about 0.2 μm^{-2} and more similar to the EC50 of dwell-time-matched T102S-MHC of about 2 μm^{-2} [9, 102].

Polyclonal T cells discriminate Fab'-DNA in a dwell-time-dependent manner

To illustrate the broad applicability of Fab'-DNA constructs and the potential of a Fab'-DNA affinity panel, we investigated the activation of $CD4^+$ effector T cells from polyclonal

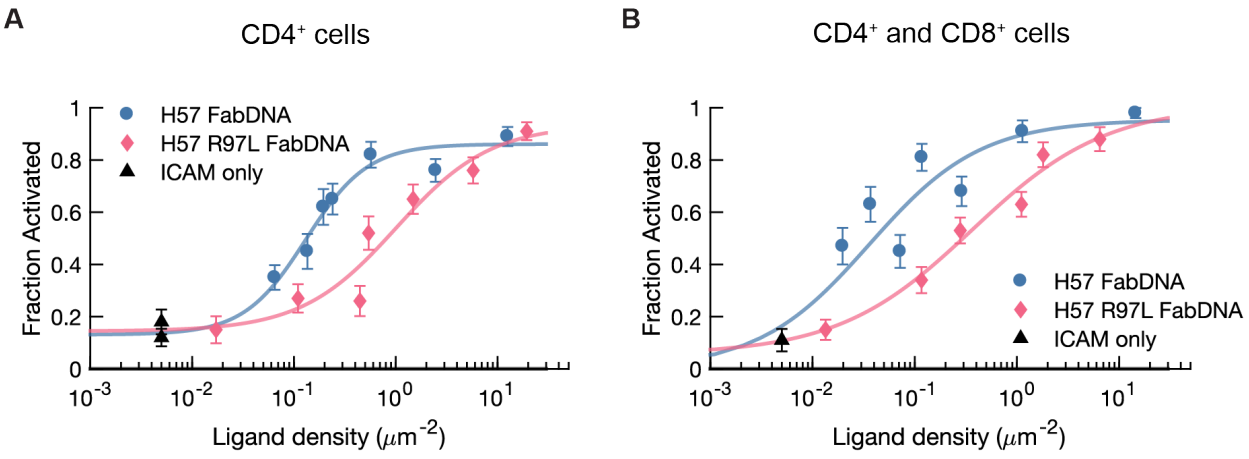

Figure 4.6: Polyclonal T cells discriminate Fab'-DNA in a dwell-time-dependent manner. NFAT dose-response curves of polyclonal **(A)** $CD4^+$ and **(B)** $CD4^+$ and $CD8^+$ T cells for parental H57 Fab'-DNA and H57 R97L Fab'-DNA show that the R97L mutant is a less potent ligand.

B6 mice with both parental H57 Fab'-DNA and the lower-affinity H57 R97L Fab'-DNA. The dose-response curve for R97L is shifted significantly to the right compared to parental H57, requiring nearly ten times the amount of ligand present on the bilayer to reach half-maximal activation (1 μm^{-2} compared to 0.15 μm^{-2}) (Fig. 4.6A). The shift in to a greater EC50 with decreased ligand dwell time aligns with observations that, in vitro, cellular activity correlates well with kinetic off-rate and affinity [34, 131, 132, 137, 139]. The dose-response curve for both polyclonal and clonal $CD4^+$ cells studied are very similar, both with ED50 of about 1 μm^{-2} and exhibiting a shallower slope than seen for pMHC ligands. $CD4^+$ cells were isolated for these experiments to best compare to the $CD4^+$ AND T cells, but experiments were also conducted with the full population of $CD4^+$ and $CD8^+$ T cells isolated from B6 mouse lymph nodes and spleens, yielding similar results (Fig. 4.6B). These results indicate that T cells read Fab'-DNA binding kinetics similarly to how they read pMHC binding kinetics and suggests future success in creating Fab'-DNA affinity panels to study signal integration and ligand discrimination in polyclonal T cells.

4.3 Discussion

Fab'-DNA ligands have previously been shown to mimic many critical aspects of native TCR triggering by pMHC ligand, while having the additional ability to bind and trigger any TCR from a species regardless of clonotype [48, 102]. However, all previous Fab'-DNA ligands have been very strong TCR binders. Here, we show that lower-affinity Fab'-DNA constructs can be synthesized using recombinantly expressed Fabs, enabling the introduction of mutations

to decrease Fab:TCR binding affinity. The major implications of this work are two-fold. First, the creation of a Fab'-DNA with a unique combination of a modest, 9 s dwell time and a high on-rate enabled mechanistic insight into how T cells integrate information across spatiotemporally correlated short binding events. Second, this work provides a roadmap to creating Fab'-DNA affinity panels in order to study quantitative aspects of T cell signal integration in any clonal or polyclonal background.

Relating findings to models of TCR ligand discrimination

Studying the response of clonal AND T cells to the lower-affinity Fab'-DNA mutant, H57 R97L Fab'-DNA provided some insight into how T cells integrate information from ligand binding kinetics using their cellular machinery. Like with pMHC ligand, single isolated Fab'-DNA:TCR binding events must persist for several to tens of seconds in order to have a significant likelihood of triggering local LAT condensation. For H57 R97L Fab'-DNA, which has a mean dwell time of 9 s, only a small fraction of TCR ligation events are long enough to trigger LAT condensation on their own (Fig. 3). However, by simultaneously monitoring all binding inputs experienced by a cell in space and time and directly observing the LAT response, we see that multiple short binding events that occur in the same spatiotemporal neighborhood can increase the probability of LAT condensation beyond what each binding event could contribute if isolated (Fig. 4A). The fast binding kinetics of H57 R97L Fab'-DNA increases the probability that binding events occur closely in space and time even when presented at a low ligand density (0.08 μm^{-2}). The high on-rate gives H57 R97L Fab'-DNA a strong propensity to bind, and the relatively high off-rate allows it to be released back into the pool of free ligand to potentially bind again elsewhere.

The ability for short binding events to contribute cooperatively to LAT condensates is significant because T cells count LAT condensation events rather than ligand binding inputs such as the total number of binding events or total duration of binding events to make activation decisions [7, 9]. These results from H57 R97L Fab'-DNA align with previous observations that, for the weak agonist T102S binding to the AND TCR, cells that experienced spatiotemporally correlated binding events were far more likely to activate compared to cells that did not experience correlated binding events [9]. The authors proposed a mechanism by which these correlated binding events contribute through time to the same pool of phosphorylated LAT. Supporting this proposal, McAffee and coworkers identified that in rare instances where, at low T102S density, binding events occurred sequentially in the same spatial neighborhood, LAT condensed several seconds after the start of the first binding event [7].

Together, these studies suggest a new mechanism by which ligands with high on-rates are able to exhibit a stronger activation than their dwell time predicts. The debate over whether ligand dwell time or affinity best correlates with cellular activation has defined investigations into how T cells discriminate ligands. Govern textitet al., and Aleksic *et al.*, independently

reconciled discrepancies in correlations between activity and both dwell time and affinity by proposing serial triggering models [34, 137]. In these models, an enhanced on-rate lengthened the effective dwell time of a single pMHC ligand by serially rebinding the same TCR, thereby allowing short-dwelling ligands to overcome kinetic proofreading steps at the TCR. Serial triggering models were based on experimental systems studying T cell activation in response to antigen presenting cells loaded with specific peptides. In these systems, the mobility of both pMHC and TCR are low, 0.02-0.04 $\mu m^2/s$, which makes it conceivable, if unlikely, that pMHC with very high on-rates could rebind the same TCR. In supported bilayer studies such as this one, the mobility of the SLB is too high for rebinding of the same TCR, or even a TCR in the same nanoscale environment, even for ligands with very high on-rates [47]. While kinetic proofreading at the TCR enforces strict discrimination thresholds for very short-dwelling ligands (half life of less than 1 s), proofreading steps further from the TCR [152] could provide an alternate means for ligands with high on-rates to cooperatively contribute to productive signaling.

LAT condensation, a discrete kinetic proofreading step downstream of the TCR [7, 148], provides a means to integrate kinetic information across multiple short binding events to different TCR in the same spatial neighborhood. We propose that instead of one pMHC serially triggering the same TCR, high on-rates enhance ligand activity by increasing the probability of LAT condensate formation within the cell. Spatiotemporal correlation can arise from the same ligand unbinding and quickly rebinding in the same spatial neighborhood or from multiple ligands binding in the same neighborhood through time. A high fraction of H57 R97L Fab'-DNA under the T cell are bound at once (Fig. 4.2B) and so the probability of them being bound closely in space and time is high. In this model, each binding event must be independently long enough to pass kinetic proofreading steps at the TCR and activate zeta-chain associated protein of 70 kDa (ZAP70) on its own, but may not be long enough to pass the threshold of LAT condensation without help from nearby ligated TCR contributing to the same pool of phosphorylated LAT.

Generation and uses of a universal TCR affinity panel

The Fab expression system opens the doors to creating a Fab'-DNA affinity panel that is reactive to all T cells. Series of altered peptide ligands have long been used to understand how T cells discriminate between self- and foreign peptide-loaded MHC molecules [34, 96, 97, 127, 133, 137, 143, 144], but these panels restrict researchers to studying specific T cell clonotypes. A Fab'-DNA affinity panel will allow T cell response to ligands with varied binding kinetics to be studied directly in any clonal or polyclonal background, easing engineering requirements and opening lines of inquiry that have been previously inaccessible.

As seen in this study, mutations that weaken Fab:TCR contacts can dramatically decrease dwell time but retain a high on-rate. Further mutations at the binding interface could further decrease Fab dwell time [99], possibly creating ligands with both extremely fast on-

and off-rates. Mutations to the framework region of the Fab could introduce conformational flexibility to the otherwise rigid Fab, thereby decreasing on-rate. High throughput screening of lower affinity mutants using phage display and fluorescence-activated cell sorting [153], can identify ligands with varied binding affinities, and techniques such as surface plasmon resonance can be additionally used to precisely characterize the three-dimensional on- and off-rates of screened Fabs. As seen with parental H57 and H57 R97L Fab'-DNA constructs, Fabs can access kinetic extremes and combinations of on- and off- rates that are difficult to access with pMHC. Therefore, these ligands can be used to test the signaling outcomes from ligands with extreme kinetics in models that predict how T cells process kinetic information.

The supported lipid bilayer platform allows binding kinetics and signaling outcome at numerous junctions in the cell signaling network to be quantitatively measured in the same cells, on the same platform, in the same assay. A Fab'-DNA panel enables quantitative mechanistic investigation of manipulations in T cells without requiring a specific clonal TCR background. For example, Fab'-DNA can be used to examine how disease-state mutations, such as an activating ZAP70 R360P mutant [145, 154], affect critical proofreading steps in T cells, such as the delay between ligand binding and LAT condensation. Fab'-DNA can also be used to study human T cell lines, such as Jurkats and HuT 78 cells, where CRISPR genetic manipulations are relatively easy but cognate pMHC ligands for the lines' native TCRs are not known. T cell lines are often activated with antibody plated on glass or from solution. The ability to quantitatively study manipulations using membrane-bound, monovalent ligand with controllable binding kinetics can enable new mechanistic insights.

Moreover, Fab'-DNA ligands with binding kinetics similar to pMHC could be used to quantitate the sensitivity of cells to ligand binding kinetics in polyclonal T cell populations, such as cells from human patients. Questions can be addressed such as: What range of sensitivities do T cells within native polyclonal populations exhibit? Does sensitivity to binding kinetics depend on TCR clone in a way that is independent of how it binds its cognate pMHC? Can cellular sensitivity be correlated with other variation within cells, such as copy number of critical signaling enzymes? Are there signatures of pathology or susceptibility to disease that can be untangled with an assay capable of assessing inputs from binding events and resulting cell signaling consequences in single cells? The work presented in this chapter provides a roadmap for building anti-human TCR Fab'-DNA ligands in order to begin addressing these questions.

4.4 Materials and Methods

Gene Blocks and Primers

Gene blocks were ordered from Integrated DNA Technologies (IDT) (Coralville, IA). Primers for site-directed mutagenesis were ordered from Elim Biopharmaceuticals Inc. (Heyward, CA).

Table 4.1: Gene blocks and primers for the H57 Fab expression vector

Modification	Sequence
H57 Fab Light Chain	GTTCCTTTCTATTCTCACAGTGCACTTTATGAGTTGATTCAGCCAAGTTCCGCCTCAGTAAC GGTCGGTGAAACCGTAAAGATCACATGCTCGGGGGACCAATTACCCAAGAACTTCGCCTATT GGTTTCAGCAGAAGTCGGACAAAAACATTTTATTATTGATCTACATGGACAACAAGCGCCCA AGCGGCATCCCGGAACGCTTCTCTGGGTCTACGAGCGGTACTACGGCGACATTAACGATCTC AGGAGCTCAACCAGAAGATGAGGCGGCGTACTATTGTCTTAGTTCATACGGTGACAACAATG ACTTAGTCTTTGGTAGCGGCACGCAACTTACAGTGCTTCGCGGTCCTAAGTCAAGCCCCAAA GTCACAGTGTTCCCGCCATCCCCGGAAGAGTTGCGCACTAATAAAGCGACATTAGTATGCTT AGTCAACGACTTTTATCCAGGCAGCGCAACAGTCACCTGGAAGGCAAATGGCGCGACTATTA ACGATGGCGTTAAGACCACGAAACCGTCGAAACAGGGGCAAAACTACATGACTTCCTCCTAC CTTTCTCTTACAGCGGACCAATGGAAGAGTCATAACCGCGTGAGTTGCCAGGTCACACATGA GGGCGAAACTGTCGAAAAATCCCTGTCGCCAGCCGAGTGCTTATAATAAGGCGCGCCAATTC TATTTCAAGGAG
H57 Fab Heavy Chain	CAGCCGGCCATGGCCCAGGTGCAGCTGCAGGAAGTGTATTTGGTGGAGTCTGGGGGCGACCT GGTACAACCTGGGAGTAGTTTAAAAGTATCCTGCGCGGCTAGTGGTTTTACTTTCAGCGATT TCTGGATGTATTGGGTTCGCCAGGCACCCGGAAAGGGTCTGGAATGGGTCGGCCGCATTAAA AACATCCCCAATAATTACGCGACTGAATATGCGGACTCGGTGCGTGGTCGCTTCACGATTAG CCGTGACGATTCACGTAATAGTATCTACTTGCAAATGAATCGTTTACGTGTTGACGACACCG CAATTTACTATTGCACCCGTGCGGGCCGCTTTGACCACTTTGACTACTGGGGTCAAGGAACG ATGGTCACTGTCTCTTCGGCAACCACAACGGCACCTTCCGTCTATCCCTTAGCACCTGCCTG CGACAGTACAACTTCGACGACCGACACTGTTACATTGGGCTGTTTAGTCAAAGGATACTTCC CAGAACCCGTTACAGTAAGTTGGAACAGTGGCGCATTGACGTCTGGAGTCCATACGTTTCCA TCGGTGCTTCACTCTGGGCTTTATAGCCTGTCCTCTAGTGTAACTGTCCCATCCTCAACATG GCCTAAGCAGCCGATTACATGTAATGTGGCTCATCCGGCGTCGTCTACAAAGGTGGATAAGA AAATTGAACCGCGTGGGGGTGGTTGTGCGGCCGCACATCATCATCACCATCACGGGGCCGCA
Add TEV site, fwd	cttccagtcaCATCATCATCACCATCACGGGGCC
Add TEV site, rev	tacaggttttcTGCGGCCGCACAACCACC
R97L, fwd	CGTGCGGGCCtCTTTGACCAC
R97L, rev	GGTGCAATAGTAAATTGCGGTG
R97A, fwd	CCGTGCGGGCgcCTTTGACCAC
R97A, rev	GTGCAATAGTAAATTGCGG
H100A, fwd	CCGCTTTGACgcCTTTGACTACTGGGGTCAAG
H100A, rev	CCCGCACGGGTGCAATAG

Buffer, broth, and media recipes

Luria Broth (LB) – 10 g tryptone, 5 g yeast extract, 5 g NaCl per 1 L, pH adjusted to 7
2xYT – 16 g tryptone, 10 g yeast extract, 5 g NaCl per 1 L, pH adjusted to 7

TES buffer – 0.2 M Tris pH 8, 0.5 mM EDTA, 0.5M sucrose
Wash buffer 1 – 50 mM Tris pH 8, 250 mM NaCl, filtered
Wash buffer 2 – 50 mM Tris pH 8, 500 mM NaCl, 20 mM Imidazole
Elution buffer – 50 mM Tris pH 8, 500 mM NaCl, 500 mM Imidazole
Wash buffer 1.5 – 50 mM Tris pH 8, 250 mM NaCl, 10 mM Imidazole

Cloning the H57 Fab' into a pCES1 expression vector

The pCES1 expression vector was a kind gift from the Charles Craik lab at UCSF. The protein sequence for the H57 Fab heavy chain and light chain were determined from the crystal structure of the H57 Fab bound to TCRβ. An additional GGGC linker was appended to the c-terminus of the heavy chain for conjugating the Fab fragment to the fluorescently labeled DNA oligo functionalized at the 5' end with a reactive maleimide group. Light and heavy chain sequences were codon optimized for expression in *E. coli* using the IDT codon optimization tool. Flags of 20-30 amino acids matching the plasmid on either side of the Fab sequence were appended to the H57 heavy chain and light chain sequences for incorporating gene blocks with Gibson Assembly.

The H57 heavy chain and light chain were incorporated sequentially into the pCES1 backbone. First, a restriction digest was used to remove the light chain sequence currently in the vector and the linearized backbone was purified by gel extraction. The H57 light chain was then incorporated using Gibson Assembly, with reagents supplied by the QB3 Stanley MacroLab. The Gibson product was transformed into XL1-Blue cells to amplify individual plasmids and sequencing confirmed proper light chain incorporation into pCES1. The process was then repeated for the H57 heavy chain.

A TEV site was added using site-directed mutagenesis (Q5 site-directed mutagenesis kit, New England Biotech, Cat #: E0554S, Ipswich, MA) between the GGGC linker and the His_6 tag in the heavy chain used for Fab purification over a Ni^{2+} column. Cleavage of the His_6 tag with TEV protease ensures that the Fab'-DNA only associates with the SLB through the DNA oligonucleotide and cannot also bind the SLB through Ni^{2+}:His_6 interactions, which would decrease the effective concentration of Fab' on the SLB and prevent quantitative measurements of on-rate and cellular input-response as a function of ligand density. With greater foresight, this site could have been incorporated into the original gene block. Site-directed mutagenesis was also used to introduce point mutations in the complementarity-determining region 3 (CDR3) of the H57 Fab heavy chain in order to lower the Fab binding affinity.

Fab' Expression and Purification

Fabs were expressed and purified as described in Kim, J., *et. al* 2011 *Methods* [151]. On day 1, BL21-CodonPlus (DE3) competent cells were transformed with the Fab plasmid and plated on LB agar plates containing 100 μg /mL carbenicillin for growth overnight. On day 2, four starter cultures of 50 mL 2xYT, 2% glucose, and 100 μg/mL carbenicillin were inoculated each with one colony. Starter cultures were grown overnight at 30 °C, 200-250 rpm. On day 3, each starter culture was diluted into 1 L of 2xYT, 0.1% glucose, and 100 μg/mL carbenicillin to OD600 of about 0.05. Large cultures were grown at 37 °C at 200-250 rpm to an OD600 of about 0.6. Upon reaching an OD600 of 0.6, large cultures were induced with IPTG to a final concentration of 1 mM and grown overnight strictly at 20 °C and 200 rpm.

Expressed Fab, directed to the oxidizing periplasm by signal sequences on both the heavy and light chains, was isolated from the periplasm on day 4. Bacteria were collected by centrifugation at 5,000 g for 30 min at 4 °C. Each pellet was thoroughly resuspended in 15 mL of ice-cold, freshly prepared TES buffer and transferred to a 50 mL falcon tube to incubate for at least 1 h on an orbital shaker at 4 °C. Ice cold Milli Q water was then added, either 15 mL or to an approximate volume of 50 mL total solution, and the incubated for another 45 min on an orbital shaker at 4 °C. The falcon tubes were then centrifuged at 10,000 g for 30 min at 4 °C and the supernatant was saved as the periplasmic fraction.

Next, Fabs were isolated from the periplasmic fraction using a Ni^{2+} affinity column. To do this, 1mL Ni^{2+} agarose bead (Cat R90101, ThermoFisher Scientific, Waltham, MA) slurry per liter of cell culture were washed in wash buffer 1 three times, centrifuging at 900 x g for two minutes, removing supernatant, and resuspending. 100 μL of 1 M $MgCl_2$ and imidazole to a final concentration of 10 mM were added to each periplasmic fraction, and tubes were gently inverted to mix. Washed Ni^{2+} were then added to each fraction and allowed to incubate for 1 h with slow rotation. Beads were then spun down at 2000 x g on a tabletop centrifuge for 10 min at 4 °C. Supernatant was decanted and saved as flowthrough and beads were transferred to a column, using wash buffer 1 to resuspend the beads to aid in the transfer.

In the column, beads were washed with 10-20 column volumes of wash buffer 2. Elution buffer was then added gently to the column when the final wash nearly reached the surface of the settled beads, totaling 10 column volumes. The first 500-750 μL of flowthrough was collected as void volume. Two elution fractions of 3 mL each were then collected from the column. Elution fractions were dialyzed overnight in 1 x PBS and 2 mM EDTA using 10 kDa MWCO dialysis cassettes (Cat # 66380, ThermoFisher Scientific, Waltham, MA).

On day 5, the His_6 tag used for Fab purification was cleaved using TEV protease, obtained from QB3 Stanley Macrolab. First, elution fractions were combined and concentrated to 0.5 – 1 mg/mL using Amicon Ultra-4 30 kDa MWCO centrifugal filter (Cat #: UFC803024,

Millipore Sigma, Burlington, MA) TEV protease in 25 mM HEPES buffer, pH 7.5, 400 mM NaCl, 10% glycerol, and 1 mM DTT was added to Fab sample at a 1:22 w/w ratio and incubated at room temperature for 1 h. The reaction was then buffer exchanged over a NAP-5 or NAP-10 desalting column (Cat #: 17085301,17085401, Cytiva, Marlborough, MA) that was equilibrated in wash buffer 1.5. Ni^{2+}, about 50 times less than the amount used for binding Fab in the periplasm prep, were also equilibrated in wash buffer 1.5 and then incubated with the buffer exchanged Fab sample. Uncleaved Fab and His-tagged TEV protease were thereby removed from the cleaved Fab, which remained in solution. After incubating the Fab sample with Ni^{2+} for 1 h at 4 °C, beads were centrifuged down and the supernatant containing cleaved H57 Fab was saved. Beads were washed twice in wash buffer 2, and supernatants of washes were saved.

Fractions collected along the way during the Fab purification were analyzed by SDS-PAGE. The supernatant from the last Ni^{2+} bead incubation and washes containing cleaved Fab were combined and dialyzed overnight in 1 x PBS and 2 mM EDTA using 10 kDa MWCO dialysis cassettes.

Fab'-DNA Synthesis

On day 6, the purified Fab was conjugated to the 3'-thiol-fluorophore, 5'-amine-linker DNA oligonucleotide. The synthesis of this functionalized oligonucleotide is described in chapter 2. The Fab can optionally be treated with 2-MEA as described in chapter 2 to ensure that the added cysteine tailing from the Fab heavy chain is reduced while not disrupting the disulfide bonds holding the heavy and light chain together. 4-fold excess dye-DNA-linker was added to Fab sample, previously concentrated to at least 0.4 mg/mL using an Amicon Ultra-4 10 kDa MWCO centrifugal filter, and incubated at room temperature for 3 h, shaking. T remove excess dye-DNA-linker after the reaction, the solution was diluted to up to 4 mL and concentrated through an Amicon Ultra-4 30 kDa MWCO centrifugal filter. Dilution and concentration were repeated, then the solution was moved to a new Amicon Ultra-4 unit and the solution was filtered two more times.

Concentrated Fab'-DNA was then purified over a size exclusion column (Superdex 200 Increase 10/300, Cytiva) using 1 x PBS buffer and an anion exchange column (Mono Q 5/50 GL, Cytiva) using a 20 mM Tris pH 8 with a salt gradient from 150 mM to 1 M NaCl over 40 min and a flow rate of 1 mL/min. Fractions containing purified Fab'-DNA as evaluated by SDS-PAGE were aliquoted and frozen in 10% glycerol.

Flow Cytometry Screening of Fab Fragments

Crude periplasm extract was used to test expressed Fab binding affinity to primary murine T cells. One million T cells were incubated in 100 μL crude periplasm extract from 5 mL cultures for 20 min on ice. After washing with imaging buffer, cells were incubated in 100

μL of 5 μg/mL anti-c-myc-AlexaFluor488 antibody, clone 9E10 (Cat #: MCA2200A488, BioRad, Hercules, CA) for 15 min on ice. Cells were washed 3 times, resuspended in 500 μL imaging buffer, and transferred to a flow cytometry tube. The parental H57 Fab and anti-CD4-AlexaFluor488 antibodies (Cat #: 100423, Biolegend, San Diego, CA) were used as positive controls and an irrelevant Fab and no Fab (only buffer) were used as negative controls. Immediately after washing the anti-myc antibody, labeling efficiency was assessed using flow cytometry. The two-step protocol of incubating cells first in the Fab and second in the fluorescent label led to overall weak but detectable signal, comparing the expressed parental H57 Fab to the directly labeled anti-CD4 antibody. Future work should append a fluorescent protein directly to the Fab heavy chain c-terminus.

Primary T Cell Harvesting and Culture

All animal work was performed with prior approval by the Lawrence Berkeley National Laboratory Animal Welfare and Research Committee (LBNL's IACUC), under the approved protocol 177003. T cells were harvested from mice expressing the AND TCR, bred as a cross of B10.Cg-Tg(TcrAND)53Hed/J X B10.BR-H2k2 H2-T18a/SgSnJ from Jackson Laboratory. Polyclonal primary murine T cells were a gift from the Art Weiss lab at UCSF.

Primary murine cell culture, preparation of viral titer, and transduction of fluorescent reporter proteins were conducted as described in chapters 2 and 3. The spleen and lymph nodes of a mouse were harvested on Day 1, processed, and plated at 10-12 million cells/mL in coated 24-well tissue culture plates in RVC media. For AND T cells, MCC peptide was added to the media at a concentration of 2 μM. Polyclonal cells were plated in 24-well uncoated tissue culture plates that had been treated the night before with anti-CD3 2C11 and anti-CD28 antibodies, left to incubate overnight, then washed with RVC to introduce a fibronectin coat in the morning. On Day 1, PLAT-E viral packaging cells cultured in PLAT media in a tissue culture treated T75 flask at 50-60% confluency were transfected with 60 μg PEI and 15 μg *lat-egfp-p2a-nfat-mcherry* bicistronic construct in the MCSV backbone that had been pre-mixed in Opti-MEM media and incubated for 20 min. Media was exchanged to RVC after 4-5 h. IL-2 was added on Day 2, within 24 h of organ harvest.

For polyclonal cells, a step was added to the usual protocol for AND T cells to isolate $CD4^+$ cells in order to more directly compare results from the polyclonal cells to the $CD4^+$ AND T cells. On day 3, before transduction with fluorescently labeled reporter proteins, $CD4^+$ cells were isolated using DynabeadsTM UntouchedTM Mouse CD4 Cell Kit (Cat #: 11416D, ThermoFisher Scientific) according to the manufacturer's instructions. 50-75 million cells were treated for each set of imaging experiments.

T cells used to look at intracellular signaling events were then transduced on Day 3 with NFAT-mCherry-P2A-LAT-eGFP packaged in MSCV retrovirus. Cell survival rate on day 3 was usually 60% of the cell count on day 1. Viral titer was removed from PLAT cells and

filtered though a 0.22 μm filter to remove cell debris. Cells were centrifuged down at 500 x g for 5 min, exchanged into viral titer at 1.3 million /mL, IL-2, and polybrene. They were then distributed to a 24-well plate with 1.5 mL per well, and centrifuged for 1 h at 1330 x g at room temperature. The following day (day 4), cells were exchanged to fresh RVC and IL-2 and recovered at 2.5 – 3.5 million /mL.

Cells were imaged on days 5-8 and were maintained in fresh RVC media containing IL-2. A successful transduction resulted in about 30% of cells expressing the fluorescent reporter proteins.

SLB Preparation

Supported lipid bilayers were prepared in Attofluor chambers (Cat #: A7816 by Invitrogen, ThermoFisher Scientific) as described in chapters 2 and 3. The 16-mer thiol strand was used in all experiments to attach Fab'-DNA ligands to the SLB.

Microscopy

A Ti Eclipse inverted microscope (Nikon, Tokyo, Japan) was used to collect all images, as previously described in chapters 2 and 3. Micromanager software was used to control image acquisition [84]. All live cell imaging was conducted in a heating stage at 37 °C and 5% CO_2. Fraction bound data were collected on cells that had been interacting with a bilayer (0.1 mum^{-2} H57 R97L Fab'-DNA) for 3-7 min. A single set of snapshots, RICM to visualize cell footprints; 20 mW at source 20 ms 1000 gain 640 nm TIRF to visualize all Fab'-DNA; 20 mW at source 500 ms 50 gain 640 nm TIRF to visualize bound Fab'-DNA, was taken for each field of view. The short-exposure time snapshot was taken before the long-exposure time snapshot to minimize photobleaching during the acquisition.

Dwell time data were collected on cells from initial landing on the SLB until tracking of ligands to the geometric center of the cell prevented accurate tracking of binding events (about 3 min after cell landing). RICM and 2 mW at source, 500 ms, 1000 gain TIRF images in the 640 nm channel were collected every 3 s in a multidimensional acquisition. Photobleaching for the dwell time distribution bleach correction was assessed using the same imaging parameters as for dwell time data on immobile (DPPC replacing DOPC lipids) SLBs presenting about 0.2 μm^{-2} H57 R97L Fab'-DNA. The immobile bilayers allow single Fab'-DNA molecules to be tracked with high fidelity through time for assessing the photobleaching rate.

Binding events and LAT signal were sequentially imaged using a multidimensional acquisition. 500 ms, 2 mW at source 640 TIRF and 70-200 ms, 1-3 mW at source 488 TIRF images were taken in sequence with a 2 s time lapse. For tracking single binding events and LAT

signaling consequences, Fab'-DNA was presented on bilayers at 0.05 – 0.15 mum^{-2}. For imaging global cellular LAT response, Fab'-DNA was presented at 0.5 mum^{-2}.

Snapshots for NFAT dose-response curves were taken of live cells 15-30 min after initially adding cells to the bilayer. Within this range of time, T cells have had ample time to land on the bilayer and respond to the presented ligand, but have not significantly dissociated from the bilayer after activation. Transduced cells were identified by their LAT signal in the 488 TIRF channel. This prevented bias from being introduced in which cells were imaged, which could be the case if cells were identified as being transduced from their NFAT signal. Identified cells were then imaged with a single set of snapshots of RICM, 640 TIRF, 488 TIRF, and 561 epifluorescence. The RICM channel was used to identify cells that were adhered to the SLB to ensure that only cells that interacted with the SLB and presented Fab'-DNA ligands were analyzed. NFAT was imaged using 561 epifluorescence at three z locations, 0 μm, 3 μm, and 6 μm above the TIRF plane in order to resolve a clear image of the nucleus.

Image Analysis

Image analysis was performed as described in chapters 2 and 3.

Chapter 5

Optogenetic Control of Single TCR Ligation Events

Kiera B. Wilhelm[1]*, Derek M. Britain[2]*, Orion D. Weiner[2], Jay T. Groves[1]

* Authors contributed equally to this work
[1] Department of Chemistry, University of California, Berkeley, Berkeley, United States
[2] Cardiovascular Research Institute, University of California, San Francisco, San Francisco, United States

5.1 Abstract

Optogentic systems allow protein interactions to be precisely controlled by light. Here, we design a platform to tune the dwell time of ligated T cell receptor (TCR) using the LOV2:Zdk optogenetic system. T cells discriminate between self and agonist peptide markers in part by sensitively assessing ligand dwell time using a kinetic proofreading mechanism. Because LOV2:Zdk undergoes rapid dissociation upon absorption of incident blue light, the dwell time of ligated receptor to be directly modulated by changing the dosage of blue light without changing the ligand:TCR binding interface. We conjugate the high affinity anti-TCRβ Fab H57-597, to Zdk to serve as a linker between TCR and fluorescently-labeled LOV2 that is conjugated to a supported lipid bilayer. We then show that the dwell time distribution of single LOV2:Zdk recruitment events follows first-order unbinding kinetics for both wild type LOV2 and the low affinity V529N mutant, in agreement with bulk dissociation results. With this, we can move forward to study dwell time-dependent signaling through the TCR in primary murine cells.

5.2 Introduction

T cells integrate information from single ligation events between their T cell receptors (TCRs) and pMHC ligands in order to make cell fate decisions. In particular, the dwell time of the binding interaction is read by T cells through a kinetic proofreading mechanism [26]. A series of chemical steps requiring input energy (in the case of the TCR, ATP hydrolysis) must be completed while a receptor is bound in order for the receptor to reach a signaling-competent state [27, 155]. If the ligand unbinds before all required chemical steps are completed, signal is not propagated through the receptor. Recent work suggests that T cells have additional kinetic proofreading steps downstream of the TCR in order to ensure a robust response to a handful of pMHC agonists while retaining high selectivity [7, 148, 152]. Correct ligand discrimination is required for T cells to respond to pathogens while preventing autoimmunity due to enhanced sensitivity to self-peptides. Recent works have begun to estimate the number of proofreading steps [156] and their general location in the signaling pathway [152], and the molecular details of some kinetic proofreading steps in T cells are beginning to be illuminated [135, 148]. However, the precise mechanism by which the T cell signaling network maintains both high sensitivity and high selectivity remains unknown.

Optogenetics provides tools to precisely control protein binding interactions with light, and so can provide a means to modulate the dwell time of a ligand:TCR interaction and probe mechanisms of T cell signal integration without changing the binding interface. The LOV-TRAP optogenetic system, composed of the LOV2 photosensor domain of phototropin 1 from textitAvena sativa and its engineered Zdark (Zdk) binding partner [157], and the phytochrome B (PhyB)/phytochrome B interaction factor (PIF) optogenetic system [158, 159] have both been used to study temporal signal integration in T cells. Tisher and Weiner [156] and Yousef and coworkers [160] both transduced Jurkats with modified receptors containing an extracellular optogenetic domain, Zdk in the case of Tisher and Weiner and PIF in the case of Yousef et al. The receptor's light-sensitive partner was present either clustered in solution or bound to a supported lipid bilayer (SLB), and light dosage and patterning was used to modulate ligand:receptor binding kinetics. Despite differences in receptor triggering and downstream readouts used to measure cellular activation, both research groups estimated that the binding half-life threshold between non-stimulatory and stimulatory ligands for Jurkats is around 7 or 8 s. Other research groups have encoded optogenetic systems into intracellular domains of chimeric antigen receptors (CARs), requiring that the optogenetic pair be bound in order for signal to propagate from the receptor [161, 162]. Recently, Jaeger and coworkers controlled the duration and patterning of endogenous TCR engagement in primary murine T cells using a PIF-H57 Fab construct to control T cell engagement with PhyB-coated beads [44]. These studies probe persistence in the T cell signaling network over repeated receptor engagement on the time scale of minutes, mimicking T cell scanning of multiple antigen presenting cells.

While these experimental platforms control the timing and patterning of receptor engage-

ment in T cells in novel ways, most fail to replicate critical features of native TCR triggering by its monovalent, membrane-bound pMHC ligand. Signaling through CARs differs fundamentally from signaling through TCR [141], resulting in blunted antigen sensitivity [142]. Clustering of ligated receptors, used to trigger TCR in experiments using PhyB/PIF, does not occur at T cell – APC junctions at physiological pMHC densities [8, 12] and may bypass native antigen discrimination mechanisms. In physiological settings, T cells respond to APCs bearing agonist pMHC at densities of 0.1 – 2 μm^{-2}, and a handful of well-spaced pMHC:TCR ligation events [8, 9], each of which can alone generate significant signaling activity [7], are sufficient to activate the T cell.

Here, we design an optogenetic platform to study signaling from single TCR ligation events with precisely tuned kinetic off-rates. the LOVTRAP binding partners, LOV2 and Zdk, stably associate in the dark and rapidly unbind upon absorption of blue light (450 - 490 nm) by LOV2 [157]. The conformational change in LOV2 induced by blue light decreases its dissociation constant with Zdk over 150-fold. We synthesize a bispecific T cell engager, composed of an anti-TCR H57 Fab' fragment covalently linked to Zdk, to bridge TCR on a primary T cell and LOV2 presented on a supported lipid bilayer (SLB). H57 Fab' stably binds TCR [80, 102], so ligation to the apposed SLB is governed by LOV2:Zdk binding kinetics. Both blue light dosage and the variant of LOV2 used modulate the pair's half life [157] while maintaining other kinetic and physical parameters of ligation, such as applied force at ligation events. Cells remain adhered to the SLB through ICAM-1:LFA-1 adhesion regardless of TCR binding states. With fluorescently labeled LOV2 presented on the bilayer at low densities (0.05 – 1 μm^{-2}), single ligation events between TCR:Fab'-Zdk:LOV2 can be directly visualized and mapped to downstream readouts of signal propagation (Fig 5.1A). This extension of our previous platform using optoCARs tranduced into Jurkat cells (Fig. 5.1B) has the advantages of studying signaling through single ligation events between ligand and endogenous TCR in primary T cells. LOV2:Zdk binding kinetics have not previously been characterized at the single molecule, which is the range we want to be at in order to understand how the T cell signaling network is tuned to recognize and process these events. This work characterized LOV2:Zdk dwell time distributions from single dwell events and finds that they fit first-order dissociation kinetics, in agreement with bulk measurements [156]. This characterization will give us confidence in interpreting LOV2:Zdk:TCR dwell times and resulting downstream signaling readouts in primary T cells.

5.3 Results

Fab'-Zdk was synthesized to enable control of endogenous TCR ligation with light

We used a click reaction between methyltetrazine and trans-cyclooctyne (TCO) to covalently link Fab' to Zdk. Both the TCO and methyltetrazine functional groups are stable at 4 °C

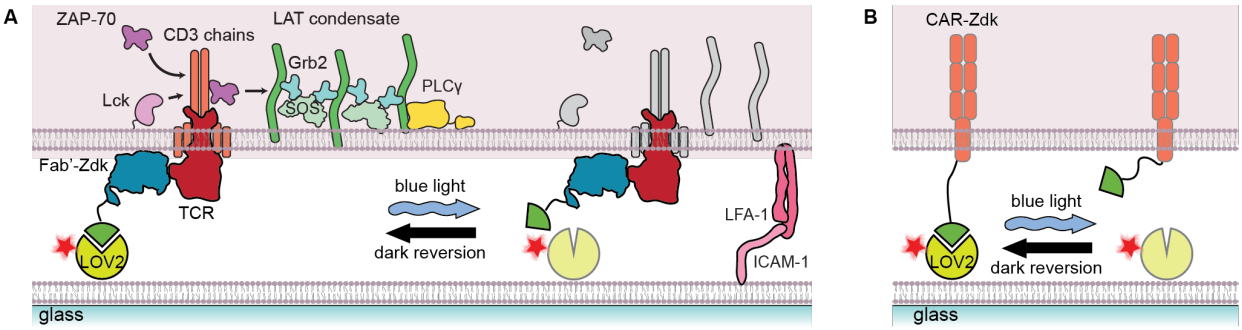

Figure 5.1: Fab'-Zdk enables direct control of ligand:TCR dwell time with light. (A) Single TCR ligation events can be controlled by blue light using the LOV2:Zdk optogenetic system, using Fab'-Zdk as a stable TCR binder. LOV2 binds Zdk in the dark, initiating phosphorylation cascades at ligated TCRs. Upon incident blue light, LOV2 undergoes a conformational change and rapidly releases Zdk, resulting in TCR unbinding and decreased downstream signaling. ICAM-1:LFA-1 adhesion interactions keep T cells stably adhered to the SLB regardless of blue light condition. **(B)** A previous system studied dwell-time dependent signaling through a CAR-Zdk construct transfected into T cells, which bound LOV2 on an SLB. With Fab'-Zdk, signaling can be studied through the native TCR.

in aqueous buffer for up to four weeks after conjugation to protein, and they react with high efficiency without requiring a toxic catalyst. The short PEG linkers in the bifunctional click reagents minimize Fab'-Zdk length and flexibility in order to maintain close contacts between the SLB and T cell membrane at TCR:Fab'-Zdk:LOV2 binding events. As TCO is used in excess of methyltetrazine in the click reaction, we conjugated TCO to Zdk, which can be expressed with high yields, and methyltetrazine to Fab', which has relatively high cost and low yields from antibody digestion.

Like with the original H57 Fab'-DNA, the Fab' fragment for Fab'-Zdk was isolated from commercially available antibody (Fig 5.2A) [102]. H57 antibody was digested with pepsin to cleave off the Fc region, and the resulting Fab'_2 fragment was purified using protein A beads. 2-mercaptoethylamine (2-MEA) was then used to reduce the disulfide bridges in the hinge region while leaving those in the Fab fragments in tact. Finally, a maleimide-PEG4-methyltetrazine linker was conjugated to the free thiol in the Fab' hinge region to functionalize the Fab for reaction to Zdk.

A cysteine point mutation was introduced to Zdk for conjugation to the TCO linker and purified as described in Tisher and Weiner 2019. Preliminary studies with a dye conjugated to the cysteine confirmed that the mutant had similar binding kinetics to LOV2 as wild type Zdk (data collected by D.M.B. Aug 2018 not shown). The maleimide-PEG3-TCO linker was conjugated to Zdk. The product was then reacted with Fab'-methyltetrazine to form the final Fab'-Zdk construct (Fig. 5.2A), which was purified by size exclusion chromatography

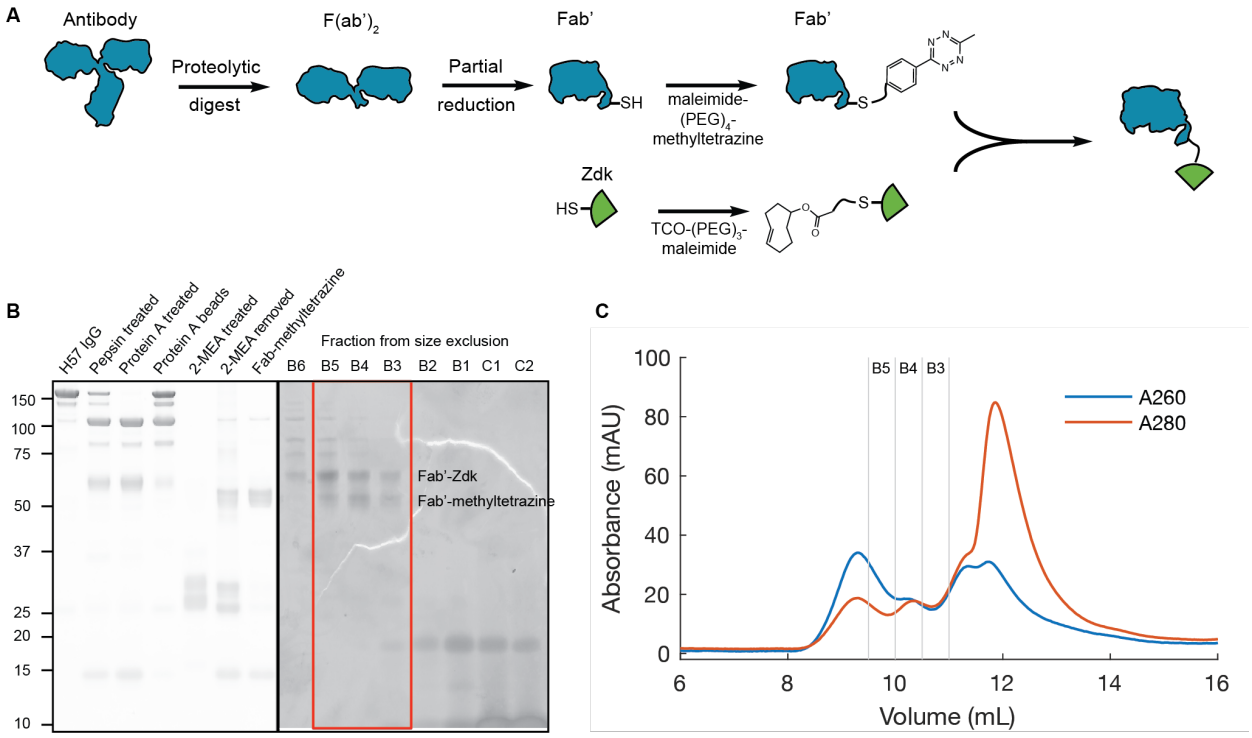

Figure 5.2: Synthesis of Fab'-Zdk. (A) Schematic of synthesis scheme for Fab'-Zdk. **(B)** Products from each of the reactions were analyzed by SDS-PAGE. The final Fab'-Zdk product was purified over a Superdex 75 size exclusion column. An expected 8 kDa shift was observed between the Fab'-methyltetrazine and Fab'-Zdk. **(C)**Absorbance traces from size exclusion chromatograpy show which peak corresponds to the desired product.

(Fig 5.2 B,C). Unreacted Zdk, present in excess in the reaction, was easily purified out, as its 8 kDa size is much smaller than the 63 kDa of Fab'-Zdk. It was more difficult to separate the 55 kDa Fab', but because the reaction was relatively effiecient (60-70%), this was a minor product (Fig. 5.2 B, size exclusion fractions). If T cells are incubated with this product prior to being introduced to LOV2-functionalized SLBs, H57 Fab' present in the sample will block some TCR, but as monovalent Fab's are inactive from solution [102, 163, 164], it will not disrupt signaling assays.

Future generations of Fab'-Zdk could be expressed and purified recombinantly using the Fab expression platform described in chapter 4. The Fab heavy chain could directly link to Zdk using a short glycine-serine linker.

Dwell time distributions of single binding events in the dark and under blue light fit first-order dissociation kinetics

Before studying endogenous TCR triggering in response to single TCR:Fab'-Zdk:LOV2 ligation events in primary cells, we characterized the distribution of single Zdk:LOV2 interactions under dark and blue light conditions. Zdk:LOV2 unbinding fits first-order dissociation kinetics in bulk [156, 157]. However, single molecule interactions may have different kinetics than the counterpart reactions in bulk or may illuminate features of the dwell time distribution that are otherwise obscured in bulk experiments [165]. In the case of LOV2:Zdk dissociation in the presence of blue light, the two steps of photon absorption by LOV2 to enter the low-affinity lit state followed by Zdk unbinding from the lit state may become apparent in single molecule measurements. Moreover, there may be a population of dark state LOV2 with unbinding kinetics convolved with that of the lit state. In bulk measurements, dark reversion, which occurs on the order of 20-30 s may complicate the bulk fluorescent readout [156], whereas in single molecule measurements, Zdk binding from solution in the middle of the acquisition can be directly accounted for. Knowing the behavior of LOV2:Zdk interactions at densities at which single interactions can be directly resolved is critical to correctly interpreting dwell time and signaling data in live cell experiments.

To obtain single LOV2:Zdk dwell times, LOV2 was conjugated to the SLB using biotin-streptavidin linkage at a relatively high density (15 μm^{-2}) and fluorescently labeled Zdk was introduced in solution at a very low concentration to enable direct visualization of single Zdk recruitment events. Care was taken to remove aggregates of streptavidin to minimize LOV2 clustering on the SLB. Bound LOV2:Zdk complexes were imaged through time both in the dark (Fig. 5.3 A,C) and under blue light (Fig. 5.3 B,D), and single complexes were tracked through time. The distributions of wild type LOV2:Zdk dwell times were compiled from these tracks (Fig. 5.3 E,F). The dwell time distributions in both the dark and under blue light were well-fit by single exponential decays, indicating that the system follows first-order dissociation kinetics under all measured conditions [156]. These results suggest that, for wild type LOV2 and blue light dosage used in these experiments, the probability of LOV2 photoconversion governs the observed dwell time, and that Zdk dissociation from light-activated LOV2 is much faster than the resolution of our experiment. This agrees with the measured bulk dwell time of Zdk interacting with fully-light activated LOV2 of 0.5 s [157]. After correction for photobleaching the mean dwell time of wild type LOV2 binding to Zdk was 120 $\pm$ 20 s in the dark and 20 $\pm$ 3 s under maximal blue light from the overhead LED. A shorter frame rate was used under light conditions to more thoroughly sample the dwell time distribution, but a control using a 10 s time lapse under blue light conditions showed that the measured dwell time distribution was independent of acquisition parameters (Fig. 5.4).

Wild type LOV2 has a long binding time to Zdk, even under maximal blue light from the illuminating LED, compared to the time scale of native pMHC:TCR binding interactions.

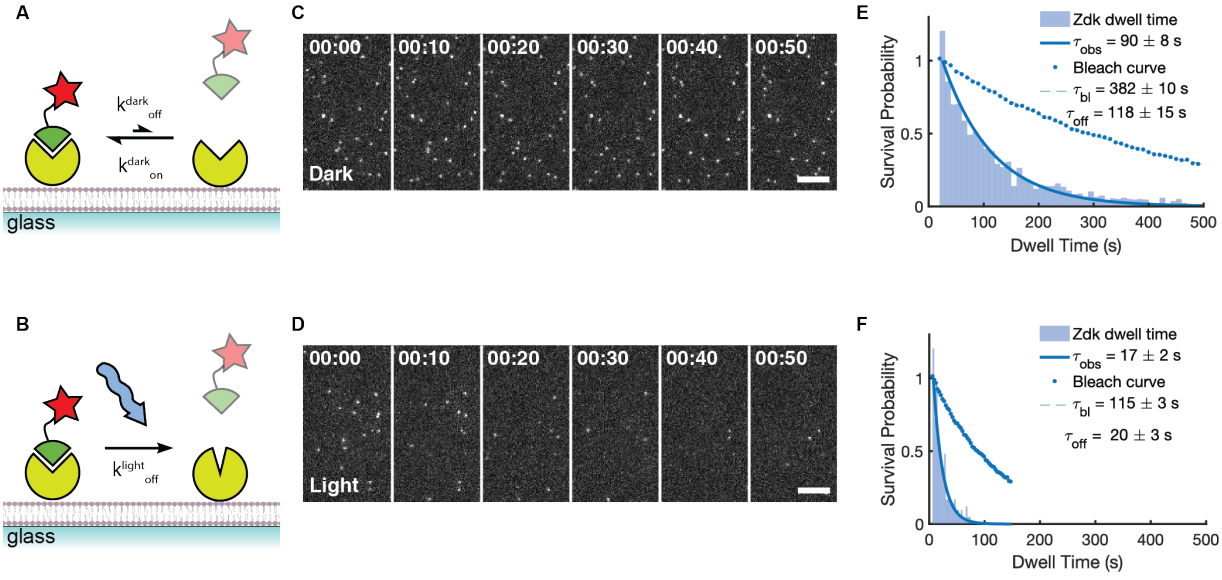

Figure 5.3: Single molecule dwell times of Zdk recruited to SLB-bound LOV2 in the dark and under blue light. (A and B) Schematic of the experiment in (A) dark and (B) blue light conditions. LOV2 is presented on SLBs composed of 98% DMPC, 2% biotin-PE phospholipids through biotin-streptavidin linkage, and fluorescently labeled Zdk is recruited from solution. **(C and D)** Recruited, labeled Zdk imaged through time. Scale bar 5 μm. **(E and F)** Compiled dwell time distribution for single Zdk trajectories. The mean dwell time in the dark is 118 $\pm$ 15 s and the mean dwell time under blue light is 20 $\pm$ 3 s. Both distributions are well-fit by a single exponential decay, indicating first order unbinding kinetics.

Variants of LOV2 have been developed with both higher and lower affinities to Zdk while still retaining large affinity differences between the dark and lit states. Preliminary dwell time distributions from lower-affinity LOV2 V529N [156, 166] are well-fit by single exponential decays, with mean dwell times that are sensitive to blue light conditions. The mean dwell time in the dark is about 16 s and decreases to about 3 s under maximal blue light (Fig. 5.5). Data under maximum blue light conditions need to be examined with greater sampling and with more experimental replicates, because two exponential components, one decaying longer and one decaying slower, might be present as the rate of LOV2 conformational change due to photon flux begins to approach the rate of Zdk unbinding from light-activated LOV2 state. The dynamic range of LOV2 V529N is appropriate for studying kinetic discrimination by T cells, and dwell times can be further decreased by more direct 488 illumination using a laser focused through the back focal objective rather than using the more diffuse overhead LED.

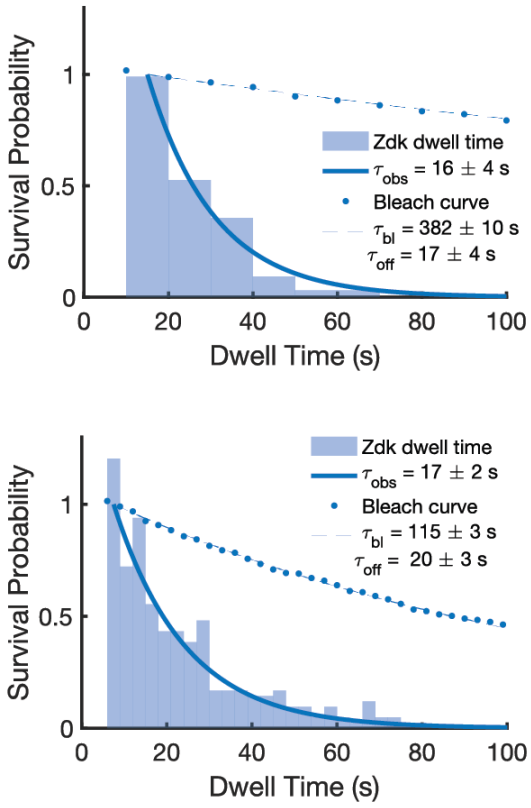

Figure 5.4: Measured dwell time is independent of acquisition parameters under blue light conditions. The mean LOV2:Zdk dwell time measured with **(A)** a 10 s imaging interval and **(B)** a 3 s imaging interval are the same, within error.

5.4 Discussion

The Fab'-Zdk bispecific T cell engager, in conjunction with LOV2-functionalized SLBs, enables the dwell time of ligand binding to endogenous TCR to be directly, experimentally controlled. Because monovalent Fab' from solution does not trigger TCR, triggering selectively occurs when TCR links to the SLB surface through Fab'-Zdk:LOV2 binding. Zdk binds LOV2 with high affinity in the dark but rapidly unbinds upon blue light-induced photoswitching. Light-controlled unbinding allows the LOV2:Zdk system to be used to experimentally modulate the dwell time of ligated TCR, which is the kinetic parameter that T cells rely on to differentiate agonist and self pMHC ligand. The geometry of TCR binding and the force sustained at binding events are not modulated as blue light dosage changes mean half life, thereby controlling for these other physical parameters to which TCR triggering is sensitive.

This experimental platform, for the first time, brings optogenetic control of TCR ligation to a platform that mimics critical aspects of native TCR triggering: triggering of the native TCR at an intermembrane junction in the presence of adhesion molecules, enabling sensitivity to single ligation events. Single molecule dwell time distributions with wild type and

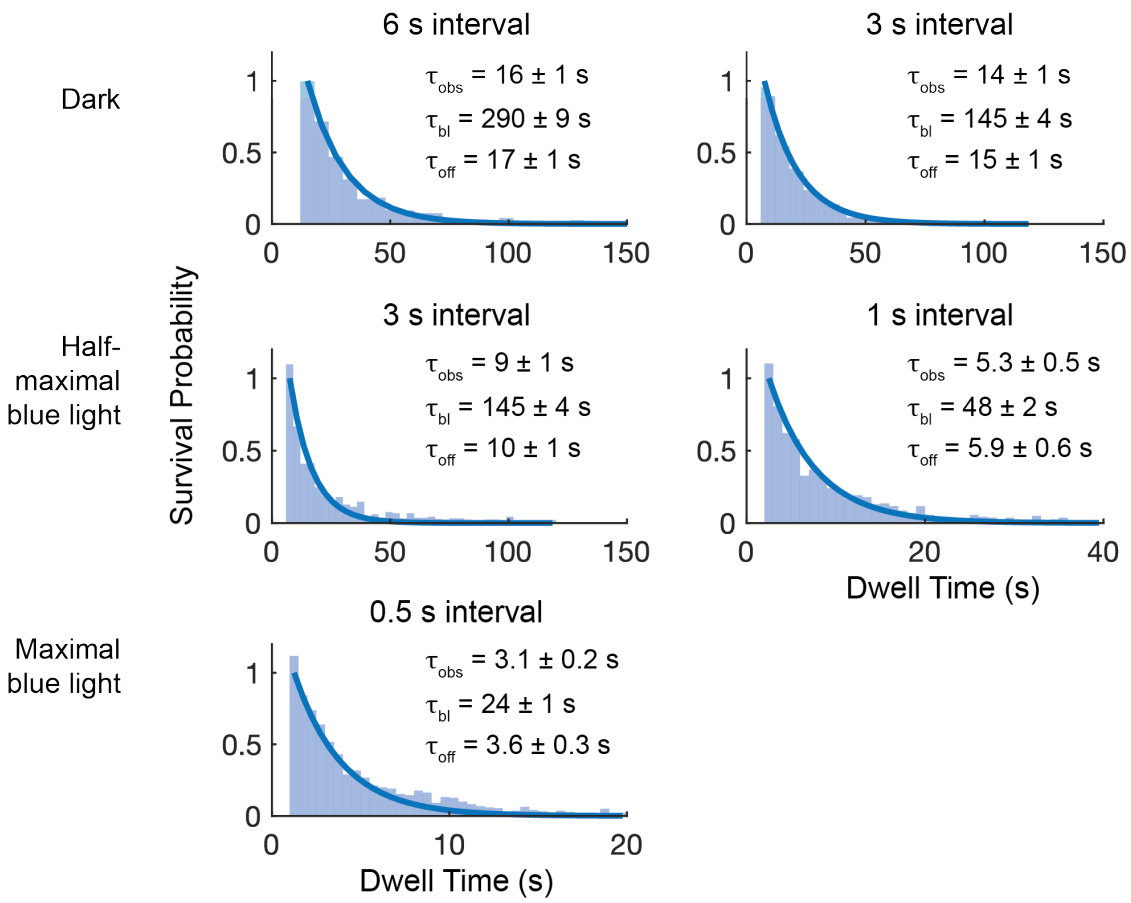

Figure 5.5: Single molecule dwell times of Zdk binding LOV2 V529N in the dark and under blue light. Dwell time distributions are compiled from single LOV2:Zdk recruitment events under dark, half-maximal blue light, or maximal blue light conditions. The interval between successive frames, noted above each panel, was determined to well-sample the dwell time distribution while minimizing photobleaching.

mutant LOV2 shows that, in agreement with bulk data [156], the dwell time distribution of single LOV2:Zdk binding events fits a single exponential decay, indicative of unimolecular unbinding, with a mean dwell time that is decreased with increased dosage of blue light. These results open the door to quantitative studies of T cell signal integration in primary murine T cells or Jurkats from ligands with precisely tunable dwell times. The recruitment of ZAP70, formation of binding-event-proximal LAT condensates, and activity of PLCγ can be monitored over a range of blue light conditions to correlate the probability of these signals with ligand dwell time. Our assays allow each binding event to be tracked through time, such that the precise inputs seen by the cell can be directly correlated to signaling outputs. Moreover, a strong pulse of blue light, perhaps patterned, can be used to rapidly unbind all LOV2:Zdk interactions in the illuminated region to study how hard cut-offs in ligand:receptor interaction times impact signal accumulation. With the knowledge that single LOV2:Zdk dwell times can be described by unimolecular unbinding kinetics for both wild type and V529N LOV2 over a range of blue light conditions, relationships between TCR triggering and downstream signaling events can be quantitatively assessed using physiologically low ligand densities to further unpack how the T cell signaling network accomplishes kinetic proofreading.

5.5 Materials and Methods

Reagents

All lipids were purchased from Avanti Polar Lipids Inc (Birmingham, AL). Standard chemical reagents and were purchased from Sigma-Aldrich (St. Louis, MO). H57-597 antibody was purchased from BioXCell (Lebanon, NH). Zdk and LOV2 were purified in-house. Click reagents methyltetrazine-PEG4-maleimide and TCO-PEG3-maleimide were purchased from Click Chemistry Tools (Scottsdale, AZ).

Fab'-Zdk Synthesis

H57 Fab' was prepared from commercially available antibody at a stock concentration of 2.5 mg/mL or higher as described in chapter 2. A cysteine point mutation was introduced in Zdk to enable conjugation to Fab'. Zdk was conjugated to TCO-PEG3-maleimide (Cat # 1002) and Fab' was conjugated to methyltetrazine-PEG4-maleimide (Cat # 1068), following manufacturer's instructions. The click reaction between TCO and methyltetrazine to link Fab' and Zdk was performed according to manufacturer's instructions. The final Fab'-Zdk product was purified over a size exclusion column (Superdex 75 Increase 10/300 GL, Cytiva) in filtered, degassed 1 x PBS buffer. Desired fractions, as determined by SDS-PAGE, were mixed with glycerol to 10%, aliquoted, flash frozen, and stored at -80 °C.

Protein Purification

LOV2 and Zdk1 for single dwell time measurements were purified and labeled as described in Tisher & Weiner 2019. Biotinylated LOV2 was labeled with AlexaFluor488 and Zdk was labeled with AlexaFluor647.

Supported Lipid Bilayer Preparation

Glass coverslips (75 x 25mm, Fisher Scientific) were cleaned for SLB formation as described in chapters 2 and 3. 6-channel ibidi chambers (ibidi, Cat#: 80608, Gräfelfing, Germany) were adhered to coverslips and manually sealed using the flat side of a 1000 uL chloroform pipette tip to ensure channels did not leak.

SUVs were prepared as described in chapters 2 and 3 with the following modifications. 1,2-dimyristoyl-sn-glycero-3-phosphocholine (DMPC) and 1,2-dioleoyl-sn-glycero-3-phosphoethanolamine-N-(cap biotinyl) (sodium salt) (Biotin-PE) lipids were mixed in chloroform in a molar ratio of 98% to 2%. After drying on a rotovap, lipid films were resuspended in MilliQ water at a temperature greater than DMPC transition temperature (24 °C). Resuspended lipids were sonicated with a tip sonicator, with no ice bath in order to keep a relatively high solution temperature, in order to form SUVs. SUVs were then mixed 1:1 with pre-warmed TBS and incubated in prepared chambers at 37 °C for 35 min. Bilayers were washed thoroughly with 1 x TBS (1 mL) and were ready for samples. All steps after bilayer formation could be performed at room temperature on the bench.

Due to the high temperature in the scope 8 microscope room, experiments with LOV2 V529N were conducted with 1,2-dipalmitoyl-sn-glycero-3-phosphocholine (DPPC), which has a transition temperature around 41 °C, in place of DMPC. Care was taken to keep the DPPC lipid solution above its transition temperature throughout preparation and SLB formation. The gel-phase bilayer facilitated tracking of single Zdk molecules that recruited to relatively immobile LOV2 molecules on the membrane.

SLB functionalization

Streptavidin that had been previously purified over a size exclusion column to remove aggregates was incubated on the bilayer at 1:1000 dilution of the stock concentration for 5 min, followed by a wash with 500 μL of wash buffer: 1 x TBS, 0.1 % BSA and 10 mM beta-mercaptoethanol (BME). Next LOV2-biotin was incubated on the bilayer for 10 min at a final concentration of 50 nM in wash buffer, followed by another washing step. This incubation condition led to a final LOV2 density on the bilayer of 15 μm^{-2}.

For single molecule recruitment measurements, Zdk was added to bilayers immediately at 0.3 nM immediately before imaging in imaging buffer containing an oxygen scavenging system:

1 x TBS, 0.1 % BSA and 10 mM BME, 2 mM Trolox, 0.32 mg/mL glucose oxidase, 0.05 mg/mL catalase, and 20 mM glucose.

Microscopy

An Eclipse Ti inverted microscope (Nikon, Tokyo, Japan), described in chapters 2 and 3, was used to image samples. Blue light for optogenetic stimulation was from a 470 nm LED (Lightspeed 490 Technologies Inc., #HPLS-36), delivered to the sample overhead through an adaptor on the condenser. The maximum blue light from the LED was 5 V in analog mode, corresponding to 400 mW continuous wave illumination. The illumination from the LED was diffuse, and scattering from the plastic ibidi chamber covering the SLBs likely further reduced the blue light intensity at the sample. Direct laser illumination from the back focal objective could be used to increase blue light dosage for future experiments.

Single molecules of Zdk-AlexaFluor647 were imaged at 5.1 mW at the sample with a 20ms exposure time and maximal camera gain. The time lapse between images depended on the LOV2 mutant used and blue light conditions, both of which modulate the mean Zdk:LOV2 dwell time. When necessary, LOV2-AlexaFluor488 was imaged with as gentle conditions as possible, 0.5 mW at the sample with a 20 ms exposure time, as taking the image with the 488 laser will also induce the conformational change in LOV2. Data collection for Zdk dwell time measurements began no sooner than 3 min after taking an image of LOV2 in the 488 channel to allow for complete dark reversion.

Photobleaching data were collected by crashing fluorescently labeled Zdk on glass and imaging using the same power, exposure time, and gain conditions as the single molecule dwell time data.

Image Analysis

Single particles were identified and tracked using Trackmate. Tracks were gently manually corrected to account for particle blinking and to link diffusing particles. Images were acquired very close to the DMPC transition temperature of 24 °C, and so, in bilayers where DMPC was used, some particles are in a gel phase and do not diffuse very much while others diffuse relatively quickly. Tracks were manually adjusted to account for errors that arose due to these two dramatically differing mobilities in the same time series.

Individual dwell times, measured by the lengths of single particle tracks, were compiled into a distribution using a custom MATLAB script as described in previous chapters. The distribution was fit to a single exponential decay, and was well fit by this model. Photobleaching was accounted for by measuring the total intensity of an area of even illumination in the photobleaching samples over the course of the acquisition. Maximum intensity was normalized to one and the decay was also fit by a single exponential decay to extract the timescale

of bleaching. The mean dwell time was calculated from the observed dwell time and the bleaching time using eqn. 2.2.

Chapter 6

Discussion, Conclusions, and Future Directions

6.1 Fab'-DNA mimics many critical features of physiological T cell activation

This dissertation work demonstrates that Fab'-DNA and pMHC ligands share many critical aspects of TCR triggering and cellular activation in primary murine $CD4^+$ effector T cells, with the important exception that Fab'-DNA can universally activate T cells. Notably, both pMHC and Fab'-DNA are monovalent ligands that are inactive in solution, but become potent T cell activators when tethered to a membrane surface as measured by translocation of transcription factors to the nucleus and cytokine production. This stands in contrast to multivalent antibodies, widely used to activate T cells, which activate T cells from solution through extensive TCR crosslinking. In addition, individual TCR ligation events from membrane-associated pMHC and Fab'-DNA constructs trigger indistinguishable proximal phosphorylation cascades, as measured by ZAP70 recruitment and LAT condensation. A few molecules of ZAP70 recruit to ligated TCR, visualized by step increases in signal from ZAP70-EGFP transduced into cells. LAT condensates form proximal to binding events after a delay on the order of low tens of seconds. For long-dwelling pMHC and Fab'-DNA, the number of LAT condensates formed per binding event experienced by the cell are statistically indistinguishable. These readouts suggest that binding events from both ligands are read similarly inside the cell and instigate similar downstream signaling cascades.

Data from Fab'-DNA constructs are consistent with widely accepted mechanisms for TCR triggering and ligand discrimination. Strong evidence over decades has shown that phosphatase exclusion from the tight intermembrane junction at pMHC:TCR binding events serves to indirectly trigger TCR by increasing local phosphorylation [16, 17, 104]. Consistent with this kinetic-segregation model, Fab'-DNA must be bound to an apposing surface

and enforce a short, 14 nm intermembrane space at binding events in order to efficiently trigger TCR. Increasing the allowed spacing by increasing the length of the DNA tether decreases TCR triggering efficiency and ligand potency. These data are also consistent with research showing that applied force through the TCR is a critical aspect of its triggering mechanism [21, 24, 167], though direction torque [20] does not appear to be required.

Fab'-DNA ligand potency correlates with dwell time consistent with the kinetic proofreading model of ligand discrimination by TCR. NFAT dose-response curves from polyclonal murine T cells significantly shifted to the right as Fab'-DNA dwell time decreased from over 140 s to 9 s. Kinetic proofreading in T cells most commonly refers to a minimum dwell time, established at about 2 s [144, 168], required for phosphorylation activity to accumulate at bound TCR for pMHC recognition. In this work, I did not develop any ligands with dwell times in the regime of less than 2 s in order to test this aspect of kinetic proofreading (though such future work would be insightful). However, comparing signaling from the parental H57 and H57 R97L Fab'-DNA, and analyzing results in the context of similar experiments with pMHC [7, 9], suggests that another layer of kinetic proofreading occurs at the level of LAT condensation. Like with pMHC, a single Fab'-DNA:TCR binding event can trigger local LAT condensation, but requires a dwell time in the low tens of seconds. Multiple shorter binding events in close spatial proximity but spread through time can cooperate to contribute to a LAT condensate. This coordination allows cells to activate in response to ligands with dwell times less than 10 s, but these ligands require a higher density or higher on-rate than longer dwelling ligands to achieve a similar activation response. Our data are consistent with ligand discrimination being determined by binding kinetics and provide new insights into how the intracellular signaling system successfully processes this kinetic information.

Suggested differences in long-term cellular adhesion of T cells in response to high densities of pMHC or Fab'-DNA merits further investigation into potential divergences in crosstalk between TCR and adhesion triggered by these ligands.

6.2 The modular design of Fab'-DNA provides a robust platform for studying signaling across membrane junctions

By allowing independent control of the receptor binding domain and membrane tether of the ligand, Fab'-DNA constructs enable numerous studies of T cell signaling and, more generally, signaling across membrane junctions. First, Fabs are stable, monomeric binders that can be generated from multiple sources. Fab' fragments can be purified and digested from commercially available antibodies or custom designed using a Fab' expression platform. I have used the former to design Fab'-DNA molecules that bind varied epitopes on murine TCR/CD3 and the later to introduce point mutations at the Fab':TCR binding interface

to decrease the Fab' dwell time. Further Fab' engineering could be used to design Fab's against novel epitopes [151, 169], perhaps in effort to develop anti-TCR Fab's with lower on-rates. Fab'-DNA constructs can likely access parameter space not easily obtained with pMHC ligands, such as extreme on- and off-rates, which could be used to test models of T cell signal integration and make predictions about real pMHC systems. Unnatural amino acids could also be engineered into the Fab' hinge region in order to more precisely control the stoichiometry of linker conjugation and minimize undesired products resulting from improper disulfide bond formation. Unlike single chain variable fragments, Fabs do not require unfolding and refolding upon purification, they remain monomeric once purified [94, 151], and do not interact non-specifically with the DNA to which they are conjugated [101]. Though my work has focused on developing synthetic TCR ligands, Fab'-DNA constructs can be developed to study a wide variety of juxtacrine signaling interactions, such as the Notch signaling pathway and eph-ephrin signaling [38].

Second, the DNA tether can be tuned independently from the Fab binding domain, as shown in the investigation of the effect of ligand height on T cell activation. More sophisticated modifications, such as the formation of hetero- or homodimers, or higher order oligomers, are readily enabled by DNA origami [37]. Such a system could be used to investigate the influence of spatial cooperativity between TCR and other membrane proteins such as co-receptors, the phosphatase CD45, costimulatory receptors, and integrins. The DNA tether can also be swapped out for an alternate means of ligand tethering, such as in the case of the Fab'-Zdk:LOV2 system. This easily sampled parameter space enables a host of future studies investigating how spatiotemporal correlations in signaling inputs govern T cell decision making. Fab'-DNA constructs fit into a larger category of T cell engagers that are used to experimentally and therapeutically study and control T cell activation [39, 42]. The literature on T cell engagers can help inspire innovation in the construction and use of Fab'-DNA molecules.

6.3 Fab'-DNA opens doors to quantitatively investigate signaling in polyclonal T cell populations

All Fab'-DNA constructs that I have designed bind murine T cells regardless of their clonotypes. This is, to our knowledge, the first rigorously characterized universal T cell engager that triggers TCR in a manner similar to native pMHC agonist, as detailed in the first section of the discussion. Fab'-DNA bypasses the need for cognate pMHCs while retaining critical features of ligand recognition, opening avenues to quantitatively investigate signaling networks in polyclonal T cell populations. This could involve studying manipulations in mouse models without requiring a transgenetic TCR background, or investigating the activation thresholds in naturally varying human T cell populations. Fab'-DNA ligands, coupled with

single cell assays such as our SLB imaging platform, open doors to asking questions such as: How does variation of protein copy number within a T cell population impact variation in single cell signaling activity and the activity of the population as a whole? How do different disease states manifest in single cell activity assays with activation conditions that mimic physiological conditions? Beyond using Fab'-DNA as a tool to uncover mechanisms which allow T cells to maintain both high sensitivity and high selectivity, Fab'-DNA imaging platforms could be a novel method for assessing the variation and diagnosing the health of human T cell populations.

References

(1) Weiss, A.; Imboden, J.; Hardy, K.; Manger, B.; Terhorst, C.; Stobo, J. *Annual Review of Immunology* **1986**, *4*, 593–619.

(2) Yin, L.; Dai, S.; Clayton, G.; Gao, W.; Wang, Y.; Kappler, J.; Marrack, P. *Protein & Cell* **2013**, *4*, 8–16.

(3) Boniface, J. J.; Rabinowtiz, J. D.; Wulfing, C.; Hampi, J.; Reich, Z.; Altman, J. D.; Kantor, R. M.; Beeson, C.; McConnell, H. M.; Davis, M. M. *Immunity* **1998**, *9*, 459–466.

(4) Irvine, D. J.; Purbhoo, M. A.; Krogsgaard, M.; Davis, M. M. *Nature* **2002**, *419*, 845–849.

(5) Purbhoo, M. A.; Irvine, D. J.; Huppa, J. B.; Davis, M. M. *Nature Immunology* **2004**, *5*, 524–530.

(6) Huang, J.; Brameshuber, M.; Zeng, X.; Xie, J.; Li, Q. j.; Chien, Y. h.; Valitutti, S.; Davis, M. M. *Immunity* **2013**, *39*, 846–857.

(7) McAffee, D. B.; O'Dair, M. K.; Lin, J. J.; Low-Nam, S. T.; Wilhelm, K. B.; Kim, S.; Morita, S.; Groves, J. T. *bioRxiv* **2021**, 2021.12.16.472676.

(8) Pielak, R. M.; O'Donoghue, G. P.; Lin, J. J.; Alfieri, K. N.; Fay, N. C.; Low-Nam, S. T.; Groves, J. T. *Proceedings of the National Academy of Sciences of the United States of America* **2017**, *114*, 12190–12195.

(9) Lin, J. J.; Low-Nam, S. T.; Alfieri, K. N.; McAffee, D. B.; Fay, N. C.; Groves, J. T. *Science Signaling* **2019**, *12*, 1–14.

(10) Mossman, K. D.; Campi, G.; Groves, J. T.; Dustin, M. L. *Science* **2005**, *310*, 1191–1193.

(11) Varma, R.; Campi, G.; Yokosuka, T.; Saito, T.; Dustin, M. L. *Immunity* **2006**, *25*, 117–127.

(12) Brameshuber, M.; Kellner, F.; Rossboth, B. K.; Ta, H.; Alge, K.; Sevcsik, E.; Göhring, J.; Axmann, M.; Baumgart, F.; Gascoigne, N. R.; Davis, S. J.; Stockinger, H.; Schütz, G. J.; Huppa, J. B. *Nature Immunology* **2018**, *19*, 487–496.

(13) Demotz, S.; Grey, H. M.; Sette, A. *Science* **1990**, *249*, 1028–1030.

(14) Harding, C. V.; Unanue, E. R. *Nature* **1990**, *346*, 574–576.

(15) Bozzacco, L.; Yu, H.; Zebroski, H. A.; Dengjel, J.; Deng, H.; Mojsov, S.; Steinman, R. M. *Journal of Proteome Research* **2011**, *10*, 5016–5030.

(16) Davis, S. J.; van der Merwe, P. *Immunology Today* **1996**, *17*, 177–187.

(17) Davis, S. J.; van der Merwe, P. A. *Nature Immunology* **2006**, *7*, 803–809.

(18) James, J. R.; Vale, R. D. *Nature* **2012**, *487*, 64–69.

(19) Carbone, C. B.; Kern, N.; Fernandes, R. A.; Hui, E.; Su, X.; Garcia, K. C.; Vale, R. D. *Proceedings of the National Academy of Sciences of the United States of America* **2017**, *114*, E9338–E9345.

(20) Kim, S. T.; Takeuchi, K.; Sun, Z. Y. J.; Touma, M.; Castro, C. E.; Fahmy, A.; Lang, M. J.; Wagner, G.; Reinherz, E. L. *Journal of Biological Chemistry* **2009**, *284*, 31028–31037.

(21) Li, Y.-C.; Chen, B.-M.; Wu, P.-C.; Cheng, T.-L.; Kao, L.-S.; Tao, M.-H.; Lieber, A.; Roffler, S. R. *The Journal of Immunology* **2010**, *184*, 5959–5963.

(22) Liu, B.; Chen, W.; Evavold, B. D.; Zhu, C. *Cell* **2014**, *157*, 357–368.

(23) Liu, Y.; Blanchfield, L.; Ma, V. P.-Y.; Andargachew, R.; Galior, K.; Liu, Z.; Evavold, B.; Salaita, K. *Proceedings of the National Academy of Sciences* **2016**, *113*, 5610–5615.

(24) Sibener, L. V. et al. *Cell* **2018**, *174*, 672–687.

(25) Choudhuri, K.; Wiseman, D.; Brown, M. H.; Gould, K.; Van Der Merwe, P. A. *Nature* **2005**, *436*, 578–582.

(26) McKeithan, T. W. *Proceedings of the National Academy of Sciences* **1995**, *92*, 5042–5046.

(27) Ganti, R. S.; Lo, W.-L.; McAffee, D. B.; Groves, J. T.; Weiss, A.; Chakraborty, A. K. *Proceedings of the National Academy of Sciences* **2020**, *117*, 26020–26030.

(28) Fernandes, R. A. et al. *Proceedings of the National Academy of Sciences of the United States of America* **2019**, *116*, 14002–14010.

(29) Kubo, R. T.; Born, W.; Kappler, J. W.; Marrack, P.; Pigeon, M. *Journal of immunology (Baltimore, Md. : 1950)* **1989**, *142*, 2736–42.

(30) Leo, O.; Foo, M.; Sachs, D. H.; Samelson, L. E.; Bluestone, J. A. *Proceedings of the National Academy of Sciences of the United States of America* **1987**, *84*, 1374–1378.

(31) Ledbetter, J. A.; June, C. H.; Grosmaire, L. S.; Rabinovitch, P. S. *Proceedings of the National Academy of Sciences* **1987**, *84*, 1384–1388.

(32) Dustin, M. L.; Springer, T. A. *Nature* **1989**, *341*, 619–624.

(33) Katagiri, K.; Hattori, M.; Minato, N.; Kinashi, T. *Molecular and Cellular Biology* **2002**, *22*, 1001–1015.

(34) Govern, C. C.; Paczosa, M. K.; Chakraborty, A. K.; Huseby, E. S. *Proceedings of the National Academy of Sciences of the United States of America* **2010**, *107*, 8724–8729.

(35) Zhong, S.; Malecek, K.; Johnson, L. A.; Yu, Z.; Vega-Saenz de Miera, E.; Darvishian, F.; McGary, K.; Huang, K.; Boyer, J.; Corse, E.; Shao, Y.; Rosenberg, S. A.; Restifo, N. P.; Osman, I.; Krogsgaard, M. *Proceedings of the National Academy of Sciences* **2013**, *110*, 6973–6978.

(36) Onoe, H.; Hsiao, S. C.; Douglas, E. S.; Gartner, Z. J.; Bertozzi, C. R.; Francis, M. B.; Mathies, R. A. *Langmuir* **2012**, *28*, 8120–8126.

(37) Coyle, M. P.; Xu, Q.; Chiang, S.; Francis, M. B.; Groves, J. T. *Journal of the American Chemical Society* **2013**, *135*, 5012–5016.

(38) Dong, M.; Spelke, D. P.; Lee, Y. K.; Chung, J. K.; Yu, C. H.; Schaffer, D. V.; Groves, J. T. *Biophysical Journal* **2018**, *115*, 865–873.

(39) Labrijn, A. F.; Janmaat, M. L.; Reichert, J. M.; Parren, P. W. *Nature Reviews Drug Discovery* **2019**, *18*, 585–608.

(40) Sun, L. L. et al. *Science Translational Medicine* **2015**, *7*, DOI: `10.1126/scitranslmed.aaa4802`.

(41) Junttila, T. T. et al. *Cancer Research* **2014**, *74*, 5561–5571.

(42) Bluemel, C.; Hausmann, S.; Fluhr, P.; Sriskandarajah, M.; Stallcup, W. B.; Baeuerle, P. A.; Kufer, P. *Cancer Immunology, Immunotherapy* **2010**, *59*, 1197–1209.

(43) Li, J. et al. *Cancer Cell* **2017**, *31*, 383–395.

(44) Jaeger, M.; Anastasio, A.; Brustlein, S.; Vincentelli, R.; Durbesson, F.; Char, R.; Boussand, M.; Lechelon, M.; Argüello, R. J.; Marguet, D.; He, H.-T.; Lasserre, R. *bioRxiv* **2022**, 2022.04.15.488452.

(45) Staufer, O.; Leithner, A.; Zhou, S.; Crames, M.; Comeau, S.; Young, D.; Low, S.; Jenkins, E.; Davis, S. J.; Nixon, A.; Pefaur, N.; Kasturirangan, S.; Dustin, M. L. *bioRxiv* **2022**, 2022.06.15.496334.

(46) Manz, B. N.; Jackson, B. L.; Petit, R. S.; Dustin, M. L.; Groves, J. *Proceedings of the National Academy of Sciences of the United States of America* **2011**, *108*, 9089–9094.

(47) O'Donoghue, G. P.; Pielak, R. M.; Smoligovets, A. A.; Lin, J. J.; Groves, J. T. *eLife* **2013**, *2*, e00778.

(48) Wilhelm, K. B.; Morita, S.; McAffee, D. B.; Kim, S.; O'Dair, M. K.; Groves, J. T. *Biophysical Journal* **2021**, *120*, 3869–3880.

(49) Merwe, P. A. v. d.; Davis, S. J. *Annual Review of Immunology* **2003**, *21*, 659–684.

(50) Cole, D. K.; Pumphrey, N. J.; Boulter, J. M.; Sami, M.; Bell, J. I.; Gostick, E.; Price, D. A.; Gao, G. F.; Sewell, A. K.; Jakobsen, B. K. *The Journal of Immunology* **2007**, *178*, 5727–5734.

(51) Fink, P. J.; Matis, L. A.; McElligott, D. L.; Bookman, M.; Hedrick, S. M. *Nature* **1986**, *321*, 219–226.

(52) Hogquist, K. A.; Jameson, S. C.; Heath, W. R.; Howard, J. L.; Bevan, M. J.; Carbone, F. R. *Cell* **1994**, *76*, 17–27.

(53) Gee, M. H. et al. *Cell* **2018**, *172*, 549–563.

(54) Kaye, J.; Porcelli, S.; Tite, J.; Jones, B.; Janeway, C. A. *Journal of Experimental Medicine* **1983**, *158*, 836–856.

(55) Kaye, J.; Janeway, C. A. *Journal of Experimental Medicine* **1984**, *159*, 1397–1412.

(56) Miescher, G. C.; Schreyer, M.; MacDonald, H. R. *Immunology Letters* **1989**, *23*, 113–118.

(57) Irving, B. A.; Weiss, A. *Cell* **1991**, *64*, 891–901.

(58) Krogsgaard, M.; Li, Q.-j.; Sumen, C.; Huppa, J. B.; Huse, M.; Davis, M. M. *Nature* **2005**, *434*, 238–243.

(59) Ledbetter, J. A.; Gentry, L. E.; June, C. H.; Rabinovitch, P. S.; Purchio, A. F. *Molecular and Cellular Biology* **1987**, *7*, 650–656.

(60) Altman, J. D.; Moss, P. A.; Goulder, P. J.; Barouch, D. H.; McHeyzer-Williams, M. G.; Bell, J. I.; McMichael, A. J.; Davis, M. M. *Science* **1996**, *274*, 94–96.

(61) Monks, C. R. F.; Freiberg, B. A.; Kupfer, H.; Sciaky, N.; Kupfer, A. *Nature* **1998**, *395*, 82–86.

(62) Grakoui, A.; Bromley, S. K.; Sumen, C.; Davis, M. M.; Shaw, A. S.; Allen, P. M.; Dustin, M. L. *Science* **1999**, *285*, 221–227.

(63) Yokosuka, T.; Sakata-Sogawa, K.; Kobayashi, W.; Hiroshima, M.; Hashimoto-Tane, A.; Tokunaga, M.; Dustin, M. L.; Saito, T. *Nature Immunology* **2005**, *6*, 1253–1262.

(64) DeMond, A. L.; Mossman, K. D.; Starr, T.; Dustin, M. L.; Groves, J. T. *Biophysical Journal* **2008**, *94*, 3286–3292.

(65) Yu, Y.; Fay, N. C.; Smoligovets, A. A.; Wu, H.-J.; Groves, J. T. *PLoS ONE* **2012**, *7*, ed. by Kanellopoulos, J., e30704.

(66) Dustin, M. L.; Groves, J. T. *Annual Review of Biophysics* **2012**, *41*, 543–556.

(67) Purcell, A. W.; Croft, N. P.; Tscharke, D. C. *Current Opinion in Immunology* **2016**, *40*, 88–95.

(68) Campi, G.; Varma, R.; Dustin, M. L. *Journal of Experimental Medicine* **2005**, *202*, 1031–1036.

(69) Caculitan, N. G.; Kai, H.; Liu, E. Y.; Fay, N.; Yu, Y.; Lohmüller, T.; O'Donoghue, G. P.; Groves, J. T. *Nano Letters* **2014**, *14*, 2293–2298.

(70) Feng, Y.; Brazin, K. N.; Kobayashi, E.; Mallis, R. J.; Reinherz, E. L.; Lang, M. J. *Proceedings of the National Academy of Sciences of the United States of America* **2017**, *114*, E8204–E8213.

(71) Rossboth, B.; Arnold, A. M.; Ta, H.; Platzer, R.; Kellner, F.; Huppa, J. B.; Brameshuber, M.; Baumgart, F.; Schütz, G. J. *Nature Immunology* **2018**, *19*, 821–827.

(72) Kim, S. T.; Shin, Y.; Brazin, K.; Mallis, R. J.; Sun, Z. Y. J.; Wagner, G.; Lang, M. J.; Reinherz, E. L. TCR mechanobiology: Torques and tunable structures linked to early T cell signaling, 2012.

(73) Limozin, L.; Bridge, M.; Bongrand, P.; Dushek, O.; van der Merwe, P. A.; Robert, P. *Proceedings of the National Academy of Sciences* **2019**, *116*, DOI: 10.1073/pnas.1902141116.

(74) Lee, M. S.; Glassman, C. R.; Deshpande, N. R.; Badgandi, H. B.; Parrish, H. L.; Uttamapinant, C.; Stawski, P. S.; Ting, A. Y.; Kuhns, M. S. *Immunity* **2015**, *43*, 227–239.

(75) Pessano, S.; Oettgen, H.; Bhan, A. K.; Terhorst, C. *The EMBO journal* **1985**, *4*, 337–44.

(76) Kung, P. C.; Goldstein, G.; Reinherz, E. L.; Schlossman, S. F. *Science* **1979**, *206*, 347–349.

(77) Wang, J. H.; Lim, K.; Smolyar, A.; Teng, M. K.; Liu, J. H.; Tse, A. G.; Liu, J.; Hussey, R. E.; Chishti, Y.; Thomson, C. T.; Sweet, R. M.; Nathenson, S. G.; Chang, H. C.; Sacchettini, J. C.; Reinherz, E. L. *EMBO Journal* **1998**, *17*, 10–26.

(78) Das, D. K.; Feng, Y.; Mallis, R. J.; Li, X.; Keskin, D. B.; Hussey, R. E.; Brady, S. K.; Wang, J. H.; Wagner, G.; Reinherz, E. L.; Lang, M. J. *Proceedings of the National Academy of Sciences of the United States of America* **2015**, *112*, 1517–1522.

(79) Johnson, K. G.; Bromley, S. K.; Dustin, M. L.; Thomas, M. L. *Proceedings of the National Academy of Sciences* **2000**, *97*, 10138–10143.

(80) Huppa, J. B.; Axmann, M.; Mörtelmaier, M. A.; Lillemeier, B. F.; Newell, E. W.; Brameshuber, M.; Klein, L. O.; Schütz, G. J.; Davis, M. M. *Nature* **2010**, *463*, 963–967.

(81) Aramburu, J.; Yaffe, M. B.; López-Rodrıguez, C.; Cantley, L. C.; Hogan, P. G.; Rao, A. *Science* **1999**, *285*, 2129–2133.

(82) Marangoni, F.; Murooka, T. T.; Manzo, T.; Kim, E. Y.; Carrizosa, E.; Elpek, N. M.; Mempel, T. R. *Immunity* **2013**, *38*, 237–249.

(83) Smith, A. W.; Smoligovets, A. A.; Groves, J. T. *The Journal of Physical Chemistry A* **2011**, *115*, 3867–3875.

(84) Edelstein, A.; Amodaj, N.; Hoover, K.; Vale, R.; Stuurman, N. Computer control of microscopes using manager, 2010.

(85) Tinevez, J. Y.; Perry, N.; Schindelin, J.; Hoopes, G. M.; Reynolds, G. D.; Laplantine, E.; Bednarek, S. Y.; Shorte, S. L.; Eliceiri, K. W. *Methods* **2017**, *115*, 80–90.

(86) Cohen, E. A. K.; Abraham, A. V.; Ramakrishnan, S.; Ober, R. J. *Nature Communications* **2019**, *10*, 793.

(87) Ensign, D. L.; Pande, V. S. *Journal of Physical Chemistry B* **2010**, DOI: 10.1021/jp906786b.

(88) Strunz, T.; Oroszlan, K.; Schäfer, R.; Güntherodt, H.-J. *Proceedings of the National Academy of Sciences* **1999**, *96*, 11277–11282.

(89) Nye, J. A.; Groves, J. T. *Langmuir* **2008**, *24*, 4145–4149.

(90) Dustin, M. L.; Singer, K. H.; Tuck, D. T.; Springer, T. A. *Journal of Experimental Medicine* **1988**, *167*, 1323–1340.

(91) Chung, J. K.; Lee, Y. K.; Denson, J.-P.; Gillette, W. K.; Alvarez, S.; Stephen, A. G.; Groves, J. T. *Biophysical Journal* **2018**, *114*, 137–145.

(92) Lin, W.-C.; Yu, C.-H.; Triffo, S.; Groves, J. T. *Curr. Protoc. Chem. Biol*, *2*, 235–269.

(93) Hughes, L. D.; Rawle, R. J.; Boxer, S. G. *PLoS ONE* **2014**, *9*, ed. by Gruenberg, J., e87649.

(94) Nelson, A. D.; Hoffmann, M. M.; Parks, C. A.; Dasari, S.; Schrum, A. G.; Gil, D. *Journal of Biological Chemistry* **2012**, *287*, 42936–42950.

(95) Taylor, M. J.; Husain, K.; Gartner, Z. J.; Mayor, S.; Vale, R. D. *Cell* **2017**, *169*, 108–119.

(96) Corse, E.; Gottschalk, R. A.; Krogsgaard, M.; Allison, J. P. *PLoS Biology* **2010**, *8*, 1–12.

(97) Stepanek, O. et al. *Cell* **2014**, *159*, 333–345.

(98) Freed, D. M.; Bessman, N. J.; Kiyatkin, A.; Salazar-Cavazos, E.; Byrne, P. O.; Moore, J. O.; Valley, C. C.; Ferguson, K. M.; Leahy, D. J.; Lidke, D. S.; Lemmon, M. A. *Cell* **2017**, *171*, 683–695.

(99) Chen, B. M.; Al-Aghbar, M. A.; Lee, C. H.; Chang, T. C.; Su, Y. C.; Li, Y. C.; Chang, S. E.; Chen, C. C.; Chung, T. H.; Liao, Y. C.; Lee, C. H.; Roffler, S. R. *Frontiers in Immunology* **2017**, *8*, 1–21.

(100) Rothemund, P. W. K. *Nature* **2006**, *440*, 297–302.

(101) Hellmeier, J.; Platzer, R.; Mühlgrabner, V.; Schneider, M. C.; Kurz, E.; Schütz, G. J.; Huppa, J. B.; Sevcsik, E. *ACS Nano* **2021**, *15*, 15057–15068.

(102) Lin, J. J.; O'Donoghue, G. P.; Wilhelm, K. B.; Coyle, M. P.; Low-Nam, S. T.; Fay, N. C.; Alfieri, K. N.; Groves, J. T. *Biophysical Journal* **2020**, *118*, 2879–2893.

(103) Brazin, K. N.; Mallis, R. J.; Das, D. K.; Feng, Y.; Hwang, W.; Wang, J. h.; Wagner, G.; Lang, M. J.; Reinherz, E. L. Structural features of the aβTCR mechanotransduction apparatus that promote pMHC discrimination, 2015.

(104) Dushek, O.; Goyette, J.; van der Merwe, P. A. *Immunological Reviews* **2012**, *250*, 258–276.

(105) Chang, V. T. et al. *Nature Immunology* **2016**, *17*, 574–582.

(106) Hwang, W.; Mallis, R. J.; Lang, M. J.; Reinherz, E. L. *Proceedings of the National Academy of Sciences of the United States of America* **2020**, *117*, 21336–21345.

(107) Garboczi, D. N.; Ghosh, P.; Utz, U.; Fan, Q. R.; Biddison, W. E.; Wiley, D. C. *Nature* **1996**, *384*, 134–141.

(108) Garcia, K. C.; Degano, M.; Pease, L. R.; Huang, M.; Peterson, P. A.; Teyton, L.; Wilson, I. A. *Science* **1998**, *279*, 1166–1172.

(109) Springer, T. A. *Nature* **1990**, *346*, 425–434.

(110) Woollett, G.; Williams, A.; Shotton, D. *The EMBO Journal* **1985**, *4*, 2827–2830.

(111) McCall, M. N.; Shotton, D. M.; Barclay, A. N. *Immunology* **1992**, *76*, 310–7.

(112) Zhang, W.; Sloan-Lancaster, J.; Kitchen, J.; Trible, R. P.; Samelson, L. E. *Cell* **1998**, *92*, 83–92.

(113) Nag, A.; Monine, M. I.; Faeder, J. R.; Goldstein, B. *Biophysical Journal* **2009**, *96*, 2604–2623.

(114) Balagopalan, L.; Kortum, R. L.; Coussens, N. P.; Barr, V. A.; Samelson, L. E. *Journal of Biological Chemistry* **2015**, *290*, 26422–26429.

(115) Rangarajan, S.; He, Y.; Chen, Y.; Kerzic, M. C.; Ma, B.; Gowthaman, R.; Pierce, B. G.; Nussinov, R.; Mariuzza, R. A.; Orban, J. *Journal of Biological Chemistry* **2018**, *293*, 15991–16005.

(116) Kaye, J.; Hsu, M.-L.; Sauron, M.-E.; Jameson, S. C.; Gascoigne, N. R. J.; Hedrick, S. M. *Nature* **1989**, *341*, 746–749.

(117) Berg, S. et al. *Nature Methods* **2019**, *16*, 1226–1232.

(118) Selden, N. S.; Todhunter, M. E.; Jee, N. Y.; Liu, J. S.; Broaders, K. E.; Gartner, Z. J. *Journal of the American Chemical Society* **2012**, *134*, 765–768.

(119) Murphy, M.; Rasnik, I.; Cheng, W.; Lohman, T. M.; Ha, T. *Biophysical Journal* **2004**, *86*, 2530–2537.

(120) Hui, E.; Vale, R. D. *Nature Structural and Molecular Biology* **2014**, *21*, 133–142.

(121) Reinherz, E. L. *Nature* **2019**, 7–9.

(122) Dong, D.; Zheng, L.; Lin, J.; Zhang, B.; Zhu, Y.; Li, N.; Xie, S.; Wang, Y.; Gao, N.; Huang, Z. *Nature* **2019**, *573*, 546–552.

(123) Qi, S. Y.; Groves, J. T.; Chakraborty, A. K. *Proceedings of the National Academy of Sciences* **2001**, *98*, 6548–6553.

(124) Kaizuka, Y.; Groves, J. T. *Physical Review Letters* **2006**, DOI: `10.1103/PhysRevLett.96.118101`.

(125) Hellmeier, J. et al. *Proceedings of the National Academy of Sciences of the United States of America* **2021**, *118*, e2016857118.

(126) Palmer, E. *Nature Reviews Immunology* **2003**, *3*, 383–391.

(127) Daniels, M. A.; Teixeiro, E.; Gill, J.; Hausmann, B.; Roubaty, D.; Holmberg, K.; Werlen, G.; Holländer, G. A.; Gascoigne, N. R.; Palmer, E. *Nature* **2006**, *444*, 724–729.

(128) Tanchot, C.; Lemonnier, F. A.; Pérarnau, B.; Freitas, A. A.; Rocha, B. *Science* **1997**, *276*, 2057–2062.

(129) Tian, S.; Maile, R.; Collins, E. J.; Frelinger, J. A. *The Journal of Immunology* **2007**, *179*, 2952–2960.

(130) Stone, J. D.; Chervin, A. S.; Kranz, D. M. *Immunology* **2009**, *126*, 165–176.

(131) Matsui, K.; Boniface, J. J.; Steffner, P.; Reay, P. A.; Davis, M. M. *Proceedings of the National Academy of Sciences of the United States of America* **1994**, *91*, 12862–12866.

(132) Kersh, G. J.; Kersh, E. N.; Fremont, D. H.; Allen, P. M. *Immunity* **1998**, *9*, 817–826.

(133) Krogsgaard, M.; Prado, N.; Adams, E. J.; He, X. L.; Chow, D. C.; Wilson, D. B.; Garcia, K. C.; Davis, M. M. *Molecular Cell* **2003**, *12*, 1367–1378.

(134) Hopfield, J. J. *Proceedings of the National Academy of Sciences* **1974**, *71*, 4135–4139.

(135) Goyette, J.; Depoil, D.; Yang, Z.; Isaacson, S. A.; Allard, J.; van der Merwe, P. A.; Gaus, K.; Dustin, M. L.; Dushek, O. *Proceedings of the National Academy of Sciences of the United States of America* **2022**, *119*, DOI: 10.1073/pnas.2116815119.

(136) Gangopadhyay, K.; Roy, A.; Chandradasan, A. C.; Roy, S.; Debnath, O.; SenGupta, S.; Chowdhury, S.; Das, D.; Das, R. *bioRxiv* **2021**, 2021.11.09.467998.

(137) Aleksic, M.; Dushek, O.; Zhang, H.; Shenderov, E.; Chen, J. L.; Cerundolo, V.; Coombs, D.; van der Merwe, P. A. *Immunity* **2010**, *32*, 163–174.

(138) Kalergis, A. M.; Boucheron, N.; Doucey, M.-A.; Palmieri, E.; Goyarts, E. C.; Vegh, Z.; Luescher, I. F.; Nathenson, S. G. *Nature Immunology* **2001**, *2*, 229–234.

(139) Holler, P. D.; Kranz, D. M. *Immunity* **2003**, *18*, 255–264.

(140) Frankel, S. R.; Baeuerle, P. A. *Current Opinion in Chemical Biology* **2013**, *17*, 385–392.

(141) Davenport, A. J.; Cross, R. S.; Watson, K. A.; Liao, Y.; Shi, W.; Prince, H. M.; Beavis, P. A.; Trapani, J. A.; Kershaw, M. H.; Ritchie, D. S.; Darcy, P. K.; Neeson, P. J.; Jenkins, M. R. *Proceedings of the National Academy of Sciences of the United States of America* **2018**, *115*, E2068–E2076.

(142) Gudipati, V.; Rydzek, J.; Doel-Perez, I.; Gonçalves, V. D. R.; Scharf, L.; Königsberger, S.; Lobner, E.; Kunert, R.; Einsele, H.; Stockinger, H.; Hudecek, M.; Huppa, J. B. *Nature Immunology* **2020**, *21*, 848–856.

(143) Pettmann, J.; Huhn, A.; Shah, E. A.; Kutuzov, M. A.; Wilson, D. B.; Dustin, M. L.; Davis, S. J.; van der Merwe, P. A.; Dushek, O. *eLife* **2021**, *10*, 1–42.

(144) Altan-Bonnet, G.; Germain, R. N. *PLoS Biology* **2005**, *3*, ed. by Marrack, P., e356.

(145) Shen, L.; Matloubian, M.; Kadlecek, T. A.; Weiss, A. *Science Signaling* **2021**, *14*, 1–11.

(146) Huang, W. Y. C.; Yan, Q.; Lin, W.-C.; Chung, J. K.; Hansen, S. D.; Christensen, S. M.; Tu, H.-L.; Kuriyan, J.; Groves, J. T.; Klein, M. L., DOI: 10.1073/pnas.1602602113.

(147) Su, X.; Ditlev, J. A.; Hui, E.; Xing, W.; Banjade, S.; Okrut, J.; King, D. S.; Taunton, J.; Rosen, M. K.; Vale, R. D. *Science* **2016**, *352*, 595–599.

(148) Huang, W. Y. C.; Alvarez, S.; Kondo, Y.; Lee, Y. K.; Chung, J. K.; Lam, H. Y. M.; Biswas, K. H.; Kuriyan, J.; Groves, J. T. *Science* **2019**, *363*, 1098–1103.

(149) Wada, J.; Rathnayake, U.; Jenkins, L. M.; Singh, A.; Mohammadi, M.; Appella, E.; Randazzo, P. A.; Samelson, L. E. *Journal of Biological Chemistry* **2022**, *298*, 101680.

(150) De Haard, H. J.; Van Neer, N.; Reurs, A.; Hufton, S. E.; Roovers, R. C.; Henderikx, P.; De Bruïne, A. P.; Arends, J. W.; Hoogenboom, H. R. *Journal of Biological Chemistry* **1999**, *274*, 18218–18230.

(151) Kim, J. M.; Stroud, R. M.; Craik, C. S. *Methods* **2011**, *55*, 303–309.

(152) Britain, D.; Weiner, O. *bioRxiv (preprint)* **2021**, 1–49.

(153) Salzer, B.; Schueller, C. M.; Zajc, C. U.; Peters, T.; Schoeber, M. A.; Kovacic, B.; Buri, M. C.; Lobner, E.; Dushek, O.; Huppa, J. B.; Obinger, C.; Putz, E. M.; Holter, W.; Traxlmayr, M. W.; Lehner, M. *Nature Communications* **2020**, *11*, 1–16.

(154) Chan, A. Y.; Punwani, D.; Kadlecek, T. A.; Cowan, M. J.; Olson, J. L.; Mathes, E. F.; Sunderam, U.; Man Fu, S.; Srinivasan, R.; Kuriyan, J.; Brenner, S. E.; Weiss, A.; Puck, J. M. *Journal of Experimental Medicine* **2016**, *213*, 155–165.

(155) Chakraborty, A. K.; Weiss, A. *Nature Immunology* **2014**, *15*, 798–807.

(156) Tischer, D. K.; Weiner, O. D. *eLife* **2019**, *8*, 1–25.

(157) Wang, H.; Vilela, M.; Winkler, A.; Tarnawski, M.; Schlichting, I.; Yumerefendi, H.; Kuhlman, B.; Liu, R.; Danuser, G.; Hahn, K. M. *Nature Methods* **2016**, *13*, 755–758.

(158) Bae, G.; Choi, G. *Annual Review of Plant Biology* **2008**, *59*, 281–311.

(159) Levskaya, A.; Weiner, O. D.; Lim, W. A.; Voigt, C. A. *Nature* **2009**, *461*, 997–1001.

(160) Yousefi, O. S.; Günther, M.; Hörner, M.; Chalupsky, J.; Wess, M.; Brandl, S. M.; Smith, R. W.; Fleck, C.; Kunkel, T.; Zurbriggen, M. D.; Höfer, T.; Weber, W.; Schamel, W. W. *eLife* **2019**, *8*, 1–33.

(161) O'Donoghue, G. P.; Bugaj, L. J.; Anderson, W.; Daniels, K. G.; Rawlings, D. J.; Lim, W. A. *Proceedings of the National Academy of Sciences of the United States of America* **2021**, *118*, DOI: 10.1073/pnas.2019285118.

(162) Harris, M. J.; Fuyal, M.; James, J. R. *Molecular Systems Biology* **2021**, *17*, DOI: 10.15252/msb.202010091.

(163) Chang, T. W.; Kung, P. C.; Gingras, S. P.; Goldstein, G. *Proceedings of the National Academy of Sciences* **1981**, *78*, 1805–1808.

(164) Van Wauwe, J. P.; Goossens, J. G.; Beverley, P. C. *Journal of immunology (Baltimore, Md. : 1950)* **1984**, *133*, 129–32.

(165) Huang, W. Y. C.; Ditlev, J. A.; Chiang, H.-K.; Rosen, M. K.; Groves, J. T. *Journal of the American Chemical Society* **2017**, *139*, 18009–18015.

(166) Yao, X.; Rosen, M. K.; Gardner, K. H. *Nature Chemical Biology* **2008**, *4*, 491–497.

(167) Chen, Y.; Ju, L.; Rushdi, M.; Ge, C.; Zhu, C. *Molecular Biology of the Cell* **2017**, *28*, 3134–3155.

(168) Qi, S.; Krogsgaard, M.; Davis, M. M.; Chakraborty, A. K. *Proceedings of the National Academy of Sciences* **2006**, *103*, 4416–4421.

(169) Basu, K.; Green, E. M.; Cheng, Y.; Craik, C. S. *Current Opinion in Biotechnology* **2019**, *60*, 153–158.